

University of Nevada, Reno

**Radiation from Precursor Plasmas of Cylindrical Wire Array and X-pinch
Plasmas at 1-1.7 MA Current and Notable Spectroscopic Signatures of fs
Laser Produced Plasmas**

A dissertation submitted in partial fulfillment of the
requirements for the degree of Doctor of Philosophy in Physics

by

Austin Stafford

Dr. Alla S. Safronova/Dissertation Advisor

May 2016

Copyright © by Austin Stafford 2016

All Rights Reserved



THE GRADUATE SCHOOL

We recommend that the dissertation
prepared under our supervision by

AUSTIN STAFFORD

Entitled

**Radiation from Precursor Plasmas of Cylindrical Wire Array and X-pinch Plasmas
at 1-1.7 MA Current and Notable Spectroscopic Signatures of fs Laser Produced
Plasmas**

be accepted in partial fulfillment of the
requirements for the degree of

DOCTOR OF PHILOSOPHY

Alla S. Safronova, Ph.D., Advisor

Victor L. Kantsyrev, Ph.D., Committee Member

Kenneth W. Struve, Ph.D., Committee Member

Piotr Wiewior, Ph.D., Committee Member

Keith Dennett, Ph.D., Graduate School Representative

David W. Zeh, Ph. D., Dean, Graduate School

May, 2016

Abstract

My research began with studying precursor plasma from cylindrical wire array (CWA) Z-pinches. Z-pinches are efficient X-ray generators which makes them interesting to many research fields including high energy density (HED) physics, inertial confinement fusion, and astrophysics. Precursor plasmas play an important role in the implosion dynamics of Z-pinches and have been studied extensively. While many important aspects of precursor plasmas column have been studied, the electron temperatures of the precursor plasma was originally estimated using extreme ultraviolet spectra and were inferred to be $\sim 50\text{-}60$ eV. In later experiments on the Zebra Generator, X-ray time gated spectrometers were implemented to observe L-shell radiation from Ni-60 (94% Cu and 6% Ni) CWAs. Modeling of the spectra suggested electron temperatures of the precursor plasma exceeded 300 eV. My research continues from this point by studying precursor plasmas from CWAs using Cu, Ni, and Al wires to observe precursor plasma conditions, sensitivity to current changes, and effects of non-uniform wire material configurations. Experimental data from time resolved diagnostics including X-ray spectrometers, X-ray pinhole cameras, and diode signals were analyzed to understand precursor plasma evolution. Additional exploration into plasmas from pulse powered devices included experiments with pure Ti and Ti alloy X-pinch experiments. The goal of these experiments was to optimize the experimental parameters, most notably the array mass, to best take advantage of the current that is increased by the Load Current Multiplier (LCM) and determine the limits for the Zebra Generator with the enhanced current. Having investigated K-shell and L-shell radiation from pulsed power created plasma, it was desired to further investigate the results of notable spectroscopic signatures from HED plasmas. In order to focus on specific interactions that affect plasma radiation, ultrashort fs pulse lasers were used to create plasma that interact with the laser pulse on such small time scales that specific relativistic atomic processes can be much more

noticeable. Flat Mg targets were irradiated by 350 fs laser pulses from the Leopard Laser producing dielectronic satellite lines from K-shell plasmas. Dielectronic recombination is an important atomic process for populating atomic states with transitions that produce satellite lines and has a large influence on the ionization balance for a plasma. Analysis of the satellite lines provided information on the significance of dielectronic recombination and identified the transitions associated with the satellite structure. Lastly, K-shell Fe spectra were analyzed that were collected from 35 fs pulse laser irradiation from the J-KAREN Laser to investigate hot electron interaction and X-ray pumping effects in the formation of K-shell Fe radiation. Results included observing three distinct plasma regions and identifying hot electron presence.

This dissertation is dedicated to my parents Marc and Susie Stafford for taking care of me
before, during, and most likely after writing this

Acknowledgements

There have been many people who have contributed to completing this dissertation that I would like to thank. First is my Advisor Dr. Alla Safronova who has supported and guided me for the last six years. I will always be amazed at how she can organize conferences, teach classes, write proposals, and continually try to improve the state of the physics department all while making sure each of her students is receiving the support and guidance needed for their research. I would like to thank Dr. Victor Kantsyrev for encouraging and being patient with me while I was in charge of signal processing for our experiments and for teaching me about the experimental process and importance of connecting theory to experiments. I am thankful for Dr. Piotr Wiewior for his help with our Leopard Laser campaigns, support with my first published paper, and for taking the time to be a part of my committee. Also thank you to the rest of my committee members, Dr. Ken Struve and Dr. Keith Dennett, for taking the time out of your schedules to challenge me during my comprehensive test and dissertation defense.

I would like to thank the many members of this amazing research group that have been like another family to me. Thank you to Michael Weller for inviting me to that movie and answering all my questions; Nick Ouart for teaching me how to use the models and asking me tough questions at every conference; Glenn Osborne for teaching me how to process signals; Ishor Shrestha for building all the experimental loads and providing a happy and lighthearted atmosphere; Veronica Shlyaptseva for all the work during the campaigns; Steve Keim for assistance with signal processing, computer problems, and his collaboration in X-pinch experiments with the LCM; Emil Petkov for help with creating new models; Kim Shultz for game night and helping with oscilloscope issues; Dr. Ulyana Safronova for providing relativistic atomic data for presentations and support with writing my first paper; Dr. Andrey Esaulov for providing

modeling from the wire ablation dynamics model for my presentations; and Mindy Lorance and Max Schmidt-Petersen for being enthusiastic undergraduate students.

I would like to express my appreciation to all my collaborators who help me with my presentations and papers: Dr. Faenov from the Institute for Academic Initiatives, Dr. Coverdale from Sandia National Laboratories, and Dr. Chuvatin from Ecole Polytechnique.

I am grateful to all the staff at the University of Nevada, Reno Physics Department and the Nevada Terawatt Facility. A special thank you to Mercy Balderrama and Marvin Wakefield for taking care of all the paperwork and advising me with travel requests and contracts and to Vidya Nalajala and her students for providing assistance with troubleshooting data collection problems.

I am very grateful to my parents, Marc and Susie, and my brothers, Tyler and Levi, for taking care of me and supporting me through everything. Finally, thank you to my nephew, Osias, for being an extra bit of excitement to look forward to upon completing this dissertation.

This work was supported by the DOE/NNSA Cooperative agreements DE-FC52-06NA27588 and DE-NA0001984. Experiments at the Nevada Terawatt Facility were supported in part by DE-FC52-06NA27616, DE-FC52-06NA27586, and by the Defense Threat Reduction Agency, Basic Research Award HDTRA1-13-1-0033, to the University of Nevada, Reno.

Table of Contents

Chapter 1

Introduction.....	1
-------------------	---

Chapter 2

Experimental and Theoretical Tools.....	6
2.1- The Zebra Generator.....	6
2.2- The Leopard Laser.....	9
2.3- The J-KAREN Laser	9
2.4- Nonlocal Thermodynamic Equilibrium Modeling	10
2.4.1- K-shell Models	14
2.4.2- L-shell Models.....	21

Chapter 3

Radiative Properties of Precursor Columns from CWAs at 1 – 1.7 MA Current.....	24
3.1- Introduction to Precursor Plasmas Produced by CWAs.....	24
3.2- Mid-Atomic Number CWAs at Standard Current.....	25
3.2.1- Cu CWA at Standard Current.....	26
3.2.2- Alumel CWA at Standard Current.....	29
3.3- Ni-60 CWAs at Enhanced Current	32

3.4- Al CWA at Standard Current.....	35
3.5- Mixed Alumel/Al CWAs at Standard Current	38
3.6- Conclusions	43

Chapter 4

Spectroscopic Analysis of Ti Alloy X-pinch Experiments at 1.5-1.7 MA	46
4.1- Introduction to X-pinches.....	46
4.2- Ti-Alloy X-pinches at Enhanced Current.....	47
4.2.1- Time Gated Spectral and Imagery Data Analysis	50
4.2.2- Time Integrated Spectral Data Analysis.....	55
4.3- Conclusions	59

Chapter 5

Application of Dielectronic Recombination to Understand Satellite Structures from Laser Irradiated Mg Targets.....	61
5.1- Introduction to Dielectronic Recombination	61
5.2- Description of Mg Target Experiments and Spectrometers.....	63
5.3- Dielectronic Satellite Spectra for He-like Mg	64
5.4- Dielectronic Satellite Spectra for Li-like Mg.....	67
5.5- Dielectronic Satellite Spectra for Be-like Mg.....	71
5.6- Comparison to Experimental Spectra	73
5.7- Conclusions.....	79

Chapter 6

Influence of Hot Electrons on the Spectra of Fe Plasma Irradiated by Femtosecond Laser Pulses	82
6.1- Introduction to K-shell Fe Plasma from Femtosecond Laser Pulses.....	82
6.2- Description of Experiments	83
6.3- Modeling of the K-shell Fe Spectra.....	84
6.4- Conclusion.....	90

Chapter 7

Conclusion	92
References.....	96

List of Tables

Table 2.1 Transitions and wavelengths for diagnostically important K-shell Al and Mg lines.	15
Table 2.2 Transitions and wavelengths for diagnostically important L-shell Cu and Ni lines.	21
Table 3.1 A list of mid-Z element CWA experiments performed on the Zebra Generator at standard current (1 MA) with some experimental parameters included. ...	26
Table 4.1 Table of X-pinch experiments using Ti based wires. Load mass and total energy measured for the experiments are included.....	49
Table 5.1 Shot details for Leopard Laser Experiments. All shots had a target thickness of 50 μm	64
Table 5.2 Wavelengths (λ in \AA), radiative rates (A_r in s^{-1}), autoionization rates (A_a in s^{-1}), Auger energies (E_s in keV), branching ratio (K), intensity factors (Q_d in s^{-1}) and effective emission rate coefficients (C_{eff} in cm^3/s) ($T_e = 600$ eV) for the $2lnl'-1snl''$ transitions $n = 2,3,4,5$ in He-like Mg calculated using the MZ Code. Designations: $E = 2s2s$, $C = 2s2p$, $F = 2p2p$, $C' = 2snp$, $B' = 2pns$, $A' = 2pnd$, $J' = 2pnf$, $E' = 2sns$, $G' = 2snd$, $F' = 2pnp$, $I' = 2snf$, $S = 1s2s$, $P = 1s2p$, $S' = 1sns$, $P' = 1snp$, $D' = 1snd$, $H' = 1snf$. Digits after a letter (i.e. $F155$) stand for $(2S + 1)(2L + 1)(2J + 1)$. $A[B]$ means $A \cdot 10^B$...	66
Table 5.3 Wavelengths (λ in \AA), radiative rates (gA_r in s^{-1}), autoionization rates (gA_a in s^{-1}), Auger energies (E_s in eV), intensity factors (Q_d in s^{-1}) and effective emission rate coefficients (C_{eff} in $10^{-15} \text{cm}^3/\text{s}$) ($T_e = 600$ eV) for the $1s3l3l'-1s^23l$ Li-like Mg transitions calculated using the COWAN code. Results are given for the $1s^2$ decay channel (a) and	

the sum of $1s^2$, $1s2s$, and $1s2p$ decay channels (b). Those results are given in columns labeled as $1s2l$. A[B] means $A \cdot 10^B$68

Table 5.4 Wavelengths (λ in Å), radiative rates (gA_r in s^{-1}), autoionization rates (gA_a in s^{-1}), Auger energies (E_s in eV), intensity factors (Q_d in s^{-1}) and effective emission rate coefficients (C_{eff} in $10^{-15} \text{ cm}^3/\text{s}$) ($T_e = 600 \text{ eV}$) for the $1s3/4l'-1s^24l$ Li-like Mg transitions calculated using the Cowan Code. Results are given for the $1s^2$ decay channel (a) and the sum of $1s^2$, $1s2s$, and $1s2p$ decay channels (b). Those results are given in columns labeled as $1s2l$. A[B] means $A \cdot 10^B$70

Table 5.5 Wavelengths (λ in Å), radiative rates (gA_r in s^{-1}), autoionization rates (gA_a in s^{-1}), Auger energies (E_s in eV), intensity factors (Q_d in s^{-1}) and effective emission rate coefficients (C_{eff} in $10^{-15} \text{ cm}^3/\text{s}$) ($T_e = 600 \text{ eV}$) for the $1s^23/3l'-1s3/3l'3l''$ Li-like Mg transitions calculated using the COWAN Code. In the first two columns, we use shorter labeling: $3/3l'$ instead of $1s^23/3l'$ and $3/3l'3l''$ instead of $1s3/3l'3l''$. Results are given for the $1s^23l$ (a) and $1s2/3l'$ decay channels and the sum of these channels (b). Those results are given in columns labelled as $1s2/3l'$. A[B] means $A \cdot 10^B$72

List of Figures

- Figure 2.1** A diagram of the Zebra Generator with important sections labeled. (<http://www.unr.edu/ntf/facility/zebra>)6
- Figure 2.2** An energy level diagram displaying the different transitions that occur between ionization levels and within ionization levels. The different processes are color matched to the arrows representing the transition types.11
- Figure 2.3** A series of synthetic spectra for ionic K-shell Al displaying the T_e dependence. N_e was constant at $1 \times 10^{20} \text{ cm}^{-3}$ and hot electrons were not included. Diagnostically important lines are identified.16
- Figure 2.4** Synthetic ionic K-shell Al spectra with varying N_e to show the electron density dependence. N_e are in units of cm^{-3} , the T_e was held constant at 400 eV, and hot electrons were not included. Diagnostically important lines are identified.17
- Figure 2.5** A series of synthetic spectra for characteristic K-shell Fe displaying the T_e dependence. N_e was constant at $1 \times 10^{20} \text{ cm}^{-3}$ and hot electrons were not included. Clusters from important ionization levels are identified.18
- Figure 2.6** A series of synthetic spectra for characteristic K-shell Fe displaying the hot electron dependence. N_e was constant at $1 \times 10^{20} \text{ cm}^{-3}$ and T_e was constant at 100 eV. Clusters from important ionization levels are identified.19
- Figure 2.7** A sample Ti spectrum produced with $T_e = 3000 \text{ eV}$ and $N_e = 1 \times 10^{20} \text{ cm}^{-3}$.
.....21
- Figure 2.8** A series of synthetic spectra for L-shell Ni displaying the T_e dependence. N_e was constant at $1 \times 10^{20} \text{ cm}^{-3}$ and hot electrons were not included. Diagnostically important lines are identified.22

- Figure 2.9** Synthetic L-shell Ni spectra with varying N_e to show the electron density dependence. N_e are in units of cm^{-3} , the T_e was held constant at 300 eV, and hot electrons were not included. Diagnostically important lines are identified.23
- Figure 3.1** a) Signals for 1 MA Cu CWA including: current, PCD, x-ray time gated pinhole images (TGPH), and x-ray time gated spectra (TGSP). b) X-ray time gated pinhole images for energies $>1\text{keV}$. Times are relative to the precursor PCD peak. Anode to cathode gap is 2 cm.27
- Figure 3.2** X-ray time gated spectra for Cu CWA. Times for spectra are relative to the precursor PCD peak. Spectra from precursor radiation are shown compared to modeling from a Cu non-LTE kinetic model with electron temperature (T_e) and density (N_e) estimates.28
- Figure 3.3** a) Signals for 1 MA AluMel CWA including: current, PCD, x-ray time gated pinhole images (TGPH), and x-ray time gated spectra (TGSP). b) X-ray time gated pinhole images for energies $>1\text{keV}$. Times are relative to the precursor PCD peak. Anode to cathode gap is 2 cm.30
- Figure 3.4** X-ray time gated spectra for AluMel CWA. Times for spectra are relative to the precursor PCD peak. Spectra from precursor radiation are shown compared to modeling from a Ni non-LTE kinetic model with electron temperature (T_e) and density (N_e) estimates.31
- Figure 3.5** a) Signals for 1.5 MA Ni-60 CWA including: current, PCD, x-ray time gated pinhole images (TGPH), and x-ray time gated spectra (TGSP). b) X-ray time gated pinhole images for energies $>1\text{keV}$. Times are relative to the precursor PCD peak. Anode to cathode gap is 1 cm.33
- Figure 3.6** X-ray time gated spectra for Ni-60 CWA. Times for spectra are relative to the precursor PCD peak. Spectra from precursor radiation are shown compared to modeling from a Cu non-LTE kinetic model with electron temperature (T_e) and density (N_e) estimates.34

Figure 3.7 a) Signals for 1 MA Al CWA including: current, PCD, x-ray time gated pinhole images (TGPH), and x-ray time gated spectra (TGSP). b) Shadowgraphy images showing precursor column formation. c) X-ray time gated pinhole images for energies $>1\text{keV}$. Times are relative to the precursor PCD peak. Anode to cathode gap is 2 cm.

.....36

Figure 3.8 X-ray time gated spectra for Al CWA. Times for spectra are relative to the precursor PCD peak. Spectra from precursor radiation are shown compared to modeling from Al and Mg non-LTE kinetic models with electron temperature (T_e) and density (N_e) estimates.37

Figure 3.9 a) Signals for 1 MA Alumel/Al CWA including: current, PCD, x-ray time gated pinhole images (TGPH), and x-ray time gated spectra (TGSP). b) X-ray time gated pinhole images for energies $>1\text{keV}$. Times are relative to the precursor PCD peak. Anode to cathode gap is 1 cm.39

Figure 3.10 X-ray time gated spectra for Alumel/Al CWA. Times for spectra are relative to the precursor PCD peak. Spectra from precursor radiation are shown compared to modeling from K-shell Al and Mg and L-shell Ni non-LTE kinetic models.40

Figure 3.11 The spectral region viewable by the x-ray time gated spectrometer divided into four regions: 1t) K-shell Al and Mg from 6.5 to 9.28 Å, 1a) K-shell Al from 6.5 to 8 Å, 1t) K-shell Mg from 8 to 9.28 Å, and 2) L-shell Ni from 9.28 to 11 Å.42

Figure 3.12 The ratios of the integrations of the regions from Figure 3.11 plotted versus the time relative to the first PCD peak which is attributed to the precursor plasma. ..43

Figure 4.1 Picture of an X-pinch.46

Figure 4.2 Plot of electron temperatures estimated from K-shell radiation of plasmas created with the 1 MA Zebra generator and the theoretical curve that determines the necessary temperature to produce significant K-shell radiation for a given atomic number. Figure borrowed from proceedings of Dense Z-pinchs 2011 unpublished.48

- Figure 4.3** a) Current and diode signals, and timings for time gated diagnostics measured from a Ti alloy X-pinch experiment. b) X-ray time gated pinhole images with cutoff energies >3 and >1 keV labeled with timings. c) Shadowgraphy images recorded with timings. All timings are relative to the first peak in the XRD signal.50
- Figure 4.4** Time gated pinhole images from shot 3585. Timings are with respect to the main peak in the XRD signal.52
- Figure 4.5** Time gated spectra recorded during Ti alloy X-pinch experiment with timings relative to first peak in the XRD signal. The fifth and sixth frames are repeated with contrast adjustments for better viewing of K-shell Al lines. An approximate wavelength scale is included.53
- Figure 4.6** A cropped image of the x-ray time integrated and spatially resolved spectra collected from a Ti alloy X-pinch experiment. The different lines are grouped by element and order of reflection.56
- Figure 4.7** Lineouts from TISR spectra from Ti alloy (red) and pure Ti (blue) X-pinch experiments. Important lines are labeled.57
- Figure 4.8** A lineout taken from the central hotspot of the x-ray time integrated spatially resolved spectra focused on the K-shell Al radiation (black). Theoretical modeling of the experimental spectra estimated with $T_e = 550$ eV and $N_e = 5 \times 10^{20} \text{ cm}^{-3}$ (red).58
- Figure 5.1** K-shell Mg spectra recorded in high contrast (10^{-7}) and 350 fs pulse experiment by the FSSR and KAP spectrometers compared to synthetic spectra: a) Synthetic spectra with experimental KAP spectra. The boxed region highlights the area of focus for spectra comparison. b) KAP spectra with synthetic spectra from boxed region. c) FSSR spectra with synthetic spectra.....74
- Figure 5.2** Experimental spectra recorded by KAP spectrometer for: a) High contrast (10^{-7}) and 350 fs pulse with non-LTE kinetic modeling at electron temperature of 320 eV and electron density of $3 \times 10^{20} \text{ cm}^{-3}$, b) Low contrast (10^{-5}) and 350 fs pulse with non-LTE

kinetic modeling at electron temperature of 320 eV and electron density of $3 \times 10^{20} \text{ cm}^{-3}$, and c) Low contrast (10^{-5}) and 0.8 ns pulse with non-LTE kinetic modeling at electron temperature of 350 eV and electron density of $2 \times 10^{20} \text{ cm}^{-3}$. Boxed region highlights spectral range of focus for satellite studies.76

Figure 5.3 K-shell Mg spectra from high contrast (10^{-7}) and 350 fs pulse (a, c, e) and low contrast (10^{-5}) and 350 fs pulse (b, d, f) experiments recorded by FSSR spectrometer. Synthetic spectra (red) compared to experimental data (blue) which include: a), b) Li-like $1s3/3l'-1s^23l$ transitions as described in Table 5.3 combined with Li-like $1s3/4l'-1s^24l$ transitions as described in Table 5.4. c) Be-Like transitions as described by Table 5.5. d) He-like $2lnl'-1snl''$ transitions with $n = 2,3,4,5$ as described in Table 5.2. e) All Tables with the region around 8.4 – 8.6 Å described with He-like $2lnl'-1snl''$ transitions from Table 5.2. f) Combination of Tables 5.2, 5.3, and 5.4.77

Figure 5.4 K-shell Mg spectra from low contrast (10^{-5}) and 0.8 ns pulse experiment recorded by FSSR spectrometer. Synthetic spectra (red) compared to experimental data (blue) which include: a) He-like $2lnl'-1snl''$ transitions with $n = 2,3,4,5$ as described in Table 5.2. b) Li-like Mg $1s3/3l'-1s^23l$ transitions as described in Table 5.3. c) Combination of Tables 5.2, 5.3, and 5.4.80

Figure 6.1 Theoretical modeling matched to experimental data from laser experiments performed at J-KAREN facility. All models include 0.1% hot electrons described with a Gaussian distribution at 10 keV with a 50 eV half width at half max (HWHM). a) 3500 eV and $8 \times 10^{22} \text{ cm}^{-3}$ modeling matches He α and Ly α transitions. b) 700 eV and $1.8 \times 10^{24} \text{ cm}^{-3}$ modeling matches B-like and C-like structures between 1.88 and 1.9 Å. c) Modeling for cold K α and K β transitions suggest 10 eV electron temperatures with a $8 \times 10^{22} \text{ cm}^{-3}$ electron density.86

Figure 6.2 Combination of theoretical models shown in Figure 6.1 matched to the experimental spectrum. The modeling matches most structure between 1.85 and 1.95 Å.87

Figure 6.3 Theoretical modeling of three different hot electron concentrations, a) 10%, b) 25%, and c) 40%, with a bulk $T_e=300$ eV and $N_e=1.8 \times 10^{24}$ cm⁻³. The modeling shows the ionization balance does not fit the experimental spectrum which confirms the need for multiple regions shown in Figure 6.1.88

Figure 6.4 Theoretical modeling showing the influence of different ionizations on the K-shell Fe experimental spectrum from a stainless steel X-pinch experiment performed on the Zebra generator at 1 MA. Modeling was done with $T_e=170$ eV and $N_e=1 \times 10^{20}$ cm⁻³ and three different hot electron concentrations (1%, 2.5%, and 4%). The experimental spectrum shows evidence of He-like to F-like ions.89

Figure 6.5 Theoretical modeling for Stainless Steel X-pinch spectra estimating the plasma parameters of the highest T_e (1700 eV, 1×10^{20} cm⁻³) and lowest T_e (170 eV, 1×10^{20} cm⁻³) regions.89

Chapter 1

Introduction

The stars have inspired the advancement of science since the beginning of civilization. It began as a means to predict the seasons and has progressed to being the greatest means to understand where we come from. We have learned that the stars are what create the elements through fusion and we have made it one of our goals to achieve fusion for ourselves. Fusion is the greatest energy source we can imagine at this point and it is the inspiration for much of the research occurring today. In order to achieve fusion as an energy source, we need to improve our understanding of the physics involved with plasma formation and manipulation.

There are many devices created at this point that can create plasma in a laboratory environment including: lasers, Z-pinches, and tokamaks. By creating the plasmas in a controlled environment, we can improve our understanding of plasmas by manipulating the conditions and processes involved for the purposes of focusing on the areas of interest. Two important areas to focus on are the atomic processes occurring in the plasmas and predicting the capabilities of the technology we have. For this reason we have what are called university scale machines. These machines are typically much smaller in scale than the machines built to the peak of current capabilities, but they can be used with a higher frequency and are much cheaper to operate than the larger machines. The university machines serve to provide ground work for the larger machines by being able to identify successful and unsuccessful practices and designs with more manageable costs. Once the ideal conditions are determined, similar experiments can be done with the larger machines to create more data points to improve predictability when the technologies improve even further.

One of the most useful tools for observing plasmas is spectroscopy. Spectroscopy is the study of radiation to estimate plasma conditions. Spectroscopy is a useful tool because the plasma creates its own radiation and therefore it is not necessary to directly interfere with the plasma. The radiation emitted by the plasma is affected by many properties including: the density of the plasma, the temperature of the plasma, the size of the plasma, and the atomic processes occurring in the plasma. In order to make use of the radiation from the plasmas, spectrometers are used to separate the radiation by its wavelength. The spectrum that is created can be compared to synthetic spectra from theoretical models that are created by using inputted plasma conditions. Many interesting and useful diagnostic details were observed in astrophysical spectra and this led to improvements in theoretical codes by expanding the details of atomic processes such as dielectronic recombination (Gabriel 1972). Further improvements followed with the inclusion of details such as line shapes and opacity effects (Apruzese *et al* 1998). As computer technology improved so did the models. L-shell plasmas would eventually be created, for example, selenium (Peyrusse *et al* 1989), molybdenum, and silver (Young *et al* 1989).

Additional tools are also used to compliment the analysis using spectroscopy. Pinhole cameras provide 2-d resolution images that show the size and shape of the plasma. When multiple pinhole cameras are used with different filters, further understanding of the intensity from different spectral regions is possible with the most notable value seen when multiple materials are radiating from the same spatial regions. X-ray diode detectors are another tool. The diode detectors measure the total energy radiated during the experiment with time resolution. The diodes can be filtered differently to record the intensity of radiation from many different energy regions. The results from time gated spectra can be compared to the signals from X-ray diode detectors with similar cutoff energies to confirm the timings for the spectra and find trends with radiation intensity and plasma conditions.

The results from the analysis of X-ray spectra, X-ray pinhole images, and X-ray diodes discussed in this dissertation were from Z-pinch, X-pinch, and laser produced plasma experiments. The Z-pinch and X-pinch experiments were performed using the Zebra Generator at the Nevada Terawatt Facility (NTF) and the University of Nevada, Reno (UNR). The laser experiments were done using the Leopard Laser at the NTF and the J-KAREN laser at the Kansai Photon Science Institute (KPSI) of Japan Atomic Energy Agency. These facilities are described in Chapter 2 along with the theoretical models used to compare with the experimental spectra.

Chapter 3 details all the work I have done on precursor plasma columns from cylindrical wire arrays (CWA). Precursor plasma columns exist in unique conditions compared to the plasma in the main implosion and this can provide insight into the studies of basic plasma physics, radiation hydrodynamics, and astrophysics. Precursor plasma columns have been researched extensively with both small (~ 1 MA) (MAGPIE, Lebedev *et al* 2001 and Bott *et al* 2006) and large (~ 20 MA) (Z Machine, Cuneo *et al* 2006) machines. While many important aspects of precursor plasmas columns have been studied, the electron temperatures of the precursor plasma was originally estimated using extreme ultraviolet spectra and were inferred to be ~ 50 - 60 eV (Bott *et al* 2006). Experiments headed by Dr. Coverdale from Sandia National Laboratories, used X-ray time gated spectrometers to observe L-shell radiation from Ni-60 (94% Cu and 6% Ni) CWAs on the UNR Zebra Generator (Coverdale *et al* 2009). The spectra showed evidence that the electron temperatures of the precursor plasma radiated >300 eV, which was believed to be <60 eV before. My work began with confirming high electron temperatures in precursor plasma for other mid-Z materials. The research continued with investigations into current scaling effects on the precursor plasma column by using the load current multiplier (LCM) to increase the current from 1 MA to 1.7 MA. The last stage of research into the precursor plasma columns was observing the effects of non-uniformity. For these experiments two different wire materials,

Alumel (95% Ni, 2% Al, 2% Mn, and 1% Si) and Al, were used to break the symmetry of the system.

Ti alloy X-pinch experiments using the LCM were explored in Chapter 4. These experiments were part of the first X-pinch experiments on the UNR Zebra Generator using the enhanced current of 1.7 MA. This research was focused on observing the limits of the Zebra generator by measuring the electron temperatures of the K-shell Ti radiation. Ti X-pinch experiments were found to produce the highest K-shell electron temperatures when the Zebra Generator was run at standard current (1 MA) (A.S. Safronova 2012a).

The UNR Leopard Laser was used to produce K-shell Mg spectra in Chapter 5. The laser operated in multiple configurations related to laser pulse duration (350 fs or 0.8 ns) and prepulse to main pulse contrast ratio (10^{-5} or 10^{-7}). The purpose of these experiments was to investigate the importance of dielectronic recombination in the interpretation of satellite structures observed in K-shell Mg spectra. The experiments took advantage of a high resolution spectrometer to record very detailed satellite structure in the K-shell Mg spectra.

The analysis of K-shell Fe spectra from the KPSI J-KAREN Laser are presented in Chapter 6. The K-shell Fe experiments were performed to investigate the significance of hot electrons and X-ray pumping in the production of the K-shell Fe spectra. The laser was operated with a short 35 fs laser pulse. The spectra were investigated expecting three distinct plasma regions of differing plasma conditions. Additionally, K-shell Fe spectra from X-pinch experiments performed using the Zebra Generator at 1 MA were analyzed to emphasize the differences in K-shell radiation from HED Fe plasmas due to the significantly different time scales of the plasmas.

Chapter 7 summarizes all the research presented in this dissertation and emphasizes the achievements attributed to the research.

Chapter 2

Experimental and Theoretical Tools

2.1 The Zebra Generator

The Zebra Generator at the Nevada Terawatt Facility (NTF) at the University of Nevada, Reno (UNR) is a pulse power device that can store up to 200 kJ of energy (Bauer *et al* 1997). The energy is stored in 32 1.3 μF capacitors that are charged in parallel up to 100 kV. The capacitors are then discharged in series through multiple stages as shown in Figure 2.1. Typical currents for experiments in this dissertation were ~ 1 MA with 100-110 ns rise times which provided up to 1.5 TW of power. The Zebra Generator has up to 16 ports for attaching diagnostic equipment on the horizontal plane that are typically filled with radiation detectors, spectrometers, and pinhole cameras.

An additional attachment called the Load Current Multiplier (LCM) (Chuvatin *et al*

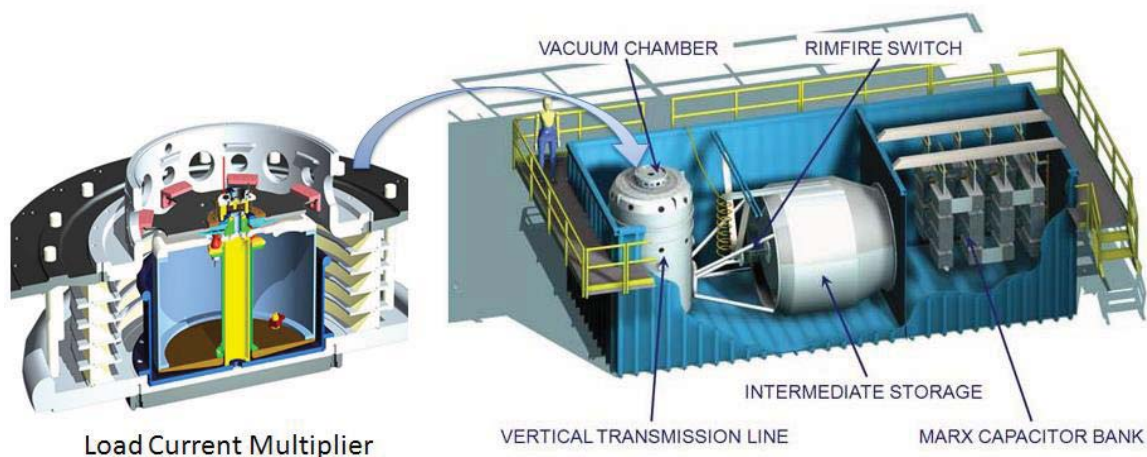


Figure 2.1. A diagram of the Zebra Generator with important sections labeled. (<http://www.unr.edu/ntf/facility/zebra>)

2010) can be connected to the load chamber. This can increase the current up to 1.7 MA and allow experiments with more massive loads as well as larger size loads compared to 1MA. Including the LCM constricts the spacing between the anode and cathode from 2 cm to 1 cm and may block viewing from some of the 16 ports due to return current posts in the chamber.

The diagnostics fielded on the Zebra Generator can be found in detail in Williamson 2011 and Osborne 2012. Experiments on the Zebra Generator field a full suite of diagnostics and the important ones for this dissertation will be briefly described in the following paragraphs.

There are multiple radiation detection diodes fielded on the Zebra Generator with varying cutoff energies. The most useful diode in this dissertation is the photo conducting (PCD) diode (PCD) which has a cutoff energy of >750 eV or <16.5 Å. This energy range includes most of the K- and L-shell x-ray radiation that will be produced by the hottest regions in these experiments.

The spectrometers are the primary tools for diagnosing plasma conditions for experiments with the Zebra Generator. The time gated spatially integrated (TGSI) spectrometer can record up to six different frames with ~ 6 ns durations. The frames are usually separated by 5 ns though they can be adjusted if desired. The TGSI spectrometer used a potassium hydrogen phthalate (KAP) crystal and the geometry of the spectrometer provides a spectral range of 6.5-11 Å. The time integrated spatially resolved (TISR) spectrometer records throughout the experiment and has spatial resolution along the anode to cathode gap. The TISR spectrometer also used a KAP crystal and the geometry provides a spectral range of approximately 2-15 Å.

The time gated pinhole images and spectra are collected by using micro-channel plate (MCP) photomultipliers. The MCP consists of up to six gold strips in which voltage is applied for short periods of time. The radiation from the source interacts with the gold plates and excites electrons due to the photoelectric effect. The voltage applied to the plates creates an electric field

that accelerates the electrons into an array of lead-oxide doped glass capillaries. The initial electrons interact with the glass creating a cascading emission of secondary electrons that are accelerated onto a phosphor screen. The interaction of the electrons with the phosphor screen creates radiation that is recorded with optical film. Adjusting the voltages will affect how many secondary electrons are emitted and can therefore be used to limit the exposure of the film based on the expected intensity of the incoming radiation.

The time gated pinhole camera has spatial resolution in both the anode to cathode axis and the radial axis. There are two cutoff energies, >1 keV (<12.5 Å) and >3 keV (<4 Å). The pinhole camera can record up to six different frames and are usually triggered with 6 ns delays between frames. The pinhole images provide information on how the plasma radiates by detecting the brightness of the plasma from different regions. The two different cutoff energies help to determine where the more energetic radiation originates and can help locate where plasma from certain materials are for experiments with multiple materials that have different energies for their K-and/or L-shell radiation.

The laser shadowgraphy provides a detailed view into the structure of the plasma at early times before the plasma becomes too dense. The shadowgraphy system works by sending a 150 ps laser pulse ($\lambda = 532$ nm) through the load chamber with a camera on the other end to detect the “shadow” cast by the plasma in the experiment. This is very valuable for experiments with precursor formation as it can be easily seen if the wires still exist while the precursor structure is evolving. The laser shadowgraphy is run with four frames separated by 3 or 6 ns. When the LCM is used there are only two frames separated by 9 ns (Weller 2014).

While I focus on the theoretical side of the research we do, I proposed and oversaw many of the experiments that created the data I analyzed. In addition, I was in charge of signal collection and processing beginning in the spring of 2013 and continuing until the spring of 2016.

My responsibilities included collecting all the data from the oscilloscopes and syncing all the timings for analysis. Along with this I was in charge of identifying signals that had problems so they could be corrected by the experimentalist that was responsible for the device. This responsibility included all experiments that were done at the NTF, including the Leopard Laser experiments.

2.2 The Leopard Laser

The Leopard Laser is a high energy laser at the NTF at UNR. The laser is a hybrid Ti:Sapphire/Nd:glass laser system that can be operated with 350 fs or 1 ns pulses with $\lambda = 1057$ nm (Wiewior *et al* 2010). For 350 fs pulses the total energy of the pulse ranges between 10 and 20 kJ, while the 1 ns pulses can provide an energy ~ 100 kJ. The laser can achieve an intensity of 10^{19} W/cm. The laser can be run with either a 10^{-5} (low contrast) or 10^{-7} (high contrast) prepulse to main pulse contrast ratio.

The diagnostics discussed in this dissertation for the Leopard experiments are two time integrated spectrometers. The first is the same TISR spectrometer used in the Zebra experiments. This spectrometer has a spectral range of 1-15 Å with a spectral resolution of $\lambda/\Delta\lambda = 300$. This spectrometer was not fielded with spatial resolution as the intensity of the radiation from the experiments was too low. The second spectrometer is a focusing spectrometer with spatial resolution (FSSR) (Faenov *et al* 1994 and Skobelev *et al* 1995). This spectrometer has a much higher spectral resolution of $\lambda/\Delta\lambda \sim 3000$ with a more limited spectral range of 14.5-17.5 Å. This spectrometer was operated with spatial resolution.

2.3 The J-KAREN Laser

The J-KAREN laser is located at Kansai Photon Science Institute of Japan Atomic Energy Agency and is an optical parametric chirped-pulse amplification (OPCPA) Ti:Sapphire

hybrid laser system (Kiriya *et al* 2010). Laser pulses have energy up to ~ 7 J, duration of 35 fs (full width at half maximum, FWHM, with respect to intensity), wavelength of 0.8 μm and a typical prepulse to main pulse contrast of 10^{-10} . The contrast is improved with a saturable absorber inserted between the high-energy CPA oscillator and stretcher. The ultrafast Pockels cell with the extinction ratio of 200 is applied at 500 ps before the main pulse to secure the contrast on the nanosecond time scale. Using F/2.1 off-axis parabolic mirror, p-polarized laser pulses are focused onto a target at an incidence angle of 84° , producing a spot with the FWHM diameter of ~ 4.5 μm (FWHM) and the peak laser intensity of 10^{21} W/cm^2 .

2.4 Nonlocal Thermodynamic Equilibrium Modeling

The primary means of understanding the plasmas that are studied in this dissertation is through spectroscopic analysis of x-ray spectra recorded during the experiments. The plasma conditions can be estimated by using models to match theoretical spectra with the experimental spectra. Choosing the theoretical model is first done by determining if the plasmas will be in local thermodynamic equilibrium (LTE) or not. Plasma is in LTE conditions if the atomic processes involving the ions are equal to the reverse processes. LTE is most common for plasma with high electron densities ($>10^{23}$ cm^{-3}) where the collisional processes dominate the radiative ones. For most experiments in this dissertation the electron densities are 10^{18} - 10^{21} cm^{-3} . For this reason non-LTE modeling is necessary. Non-LTE modeling can be used for LTE conditions however the reverse is not true. The down side to this is LTE models can be run faster than non-LTE models; however, the small number of LTE plasmas makes it an insignificant problem.

Non-LTE modeling is based around determining the populations of different states for the various ions in a plasma by solving a system of equations that balance the populating of the states with the depopulating of the states by the various atomic process. These processes are collisional excitation and de-excitation, radiative decay and resonant photo-absorption, collisional ionization

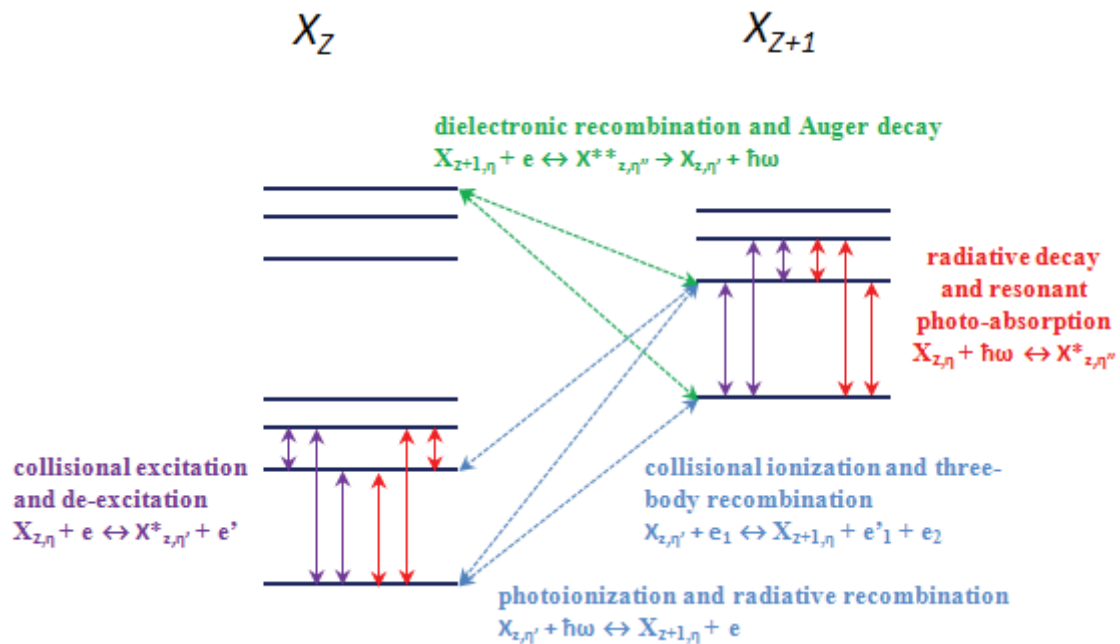


Figure 2.2. An energy level diagram displaying the different transitions that occur between ionization levels and within ionization levels. The different processes are color matched to the arrows representing the transition types.

and three body recombination, dielectronic recombination and Auger decay, and photoionization and radiative recombination. Figure 2.2 displays how these processes relate to each other. In the figure, $X_{z,\eta}$ refers to the ion with z electrons removed and with the quantum numbers represented by η . The number of asterisks (*) denotes how excited the state is, one for singly excited and two for doubly excited.

The non-LTE kinetic models used in this dissertation are based on the Flexible Atomic Code (FAC) (Gu 2008) and the Spectroscopic Collisional-Radiative Atomic Model (SCRAM) (developed by Hansen 2003 and modified by Ouart 2010). The FAC code calculates energy levels and atomic rates of the atomic processes. This information is then used by SCRAM to calculate level populations and produce synthetic spectra. The process begins by collecting the necessary atomic data for the desired element which includes energy levels, rates for radiative processes, and cross sections for collisional processes. The cross sections, $\sigma(\epsilon)$, are integrated over the

energy of a free electron, ϵ , along with the velocity of the free electron, $v(\epsilon)$, and the free electron distribution function, $F(\epsilon)$, to acquire a collisional rate as shown in Equation 2.1.

$$N_e \langle v\sigma \rangle = N_e \int v(\epsilon)\sigma(\epsilon)F(\epsilon)d\epsilon \quad (s^{-1}) \quad 2.1$$

In Equation 2.1 N_e is the electron density, $v(\epsilon) = \sqrt{2\epsilon/m_e}$, and $F(\epsilon)$ must be normalized to unity ($\int F(\epsilon)d\epsilon = 1$). For processes involving two free electrons, it would be necessary to integrate twice over the electron distribution function.

Having collected all the necessary rates, SCRAM determines the rate of change of population for each level, $\frac{dX_i}{dt}$, as described in Equation 2.2.

$$\frac{dX_i}{dt} = \sum_{j=1}^N X_j R_{ji}^{tot} - X_i \sum_{j=1}^N R_{ij}^{tot} \quad 2.2$$

The population of a level is denoted by X_i , i and j identify the initial and final levels respectively, and R_{ji}^{tot} is the sum total of the rates from state j to state i . The first term represents the populating processes while the second term is the depopulating processes. When included with the sum of the populations being unity ($\sum X_i = 1$), the fraction of the population for each energy level can be calculated. With the fractional populations, the average ion charge, $\langle z \rangle$, and the ion density, n_{ion} , can be found assuming a neutral plasma:

$$\langle z \rangle = \sum_z X_z z \quad 2.3$$

$$n_{ion} = \frac{N_e}{\langle z \rangle} \quad 2.4$$

While the previous discussion outlines the majority of the process involved with creating synthetic spectra, there are a few more things to consider. The first is how to pick the free electron distribution required in Equation 2.1. If the electrons are assumed to have non-relativistic

velocities and sufficient time to thermalize, then the electron distribution can be described with a Maxwellian distribution:

$$F_M(\varepsilon, T_e) = \frac{2}{\sqrt{\pi}T_e} \sqrt{\frac{\varepsilon}{T_e}} e^{-\varepsilon/T_e} \quad (eV^{-1}) \quad 2.5$$

T_e is the electron temperature. In order to determine if the electrons have sufficient time to thermalize Equation 2.5 is used (Spitzer 1962):

$$t_\tau \approx 3.3 \left(\frac{T_e}{100 \text{ eV}} \right)^{\frac{3}{2}} (10^{20} \text{ cm}^{-3} / n_e \ln Y) (\text{ps}) \quad 2.6$$

The thermalization time is t_τ and Y is the Coulomb logarithm which varies with the temperature and density and is generally between 5 and 15. If Equation 2.6 is used with common plasma parameters found in this dissertation, $T_e = 400 \text{ eV}$ and $n_e = 10^{20} \text{ cm}^{-3}$, then t_c is on the order of a few picoseconds. This is far faster than the typical time frames of Z-pinch plasmas which evolve on a nanosecond time scale. Most plasma can be described with the Maxwellian distribution. However, there can be a small percentage of the electrons that are much higher energy that are accelerated by the effects of instabilities in the plasma. These electrons are called “hot” electrons. When hot electrons are included, an additional electron distribution function is included with a Gaussian shape. The Gaussian is centered at ε_o with variance σ^2 . The Gaussian is added to the Maxwellian distribution with a fraction parameter, α , as shown in Equation 2.7.

$$F_{non-max}(\varepsilon, \varepsilon_o, T_e, \sigma, \alpha) = (1 - \alpha)F_M(\varepsilon, T_e) + \alpha F_G(\varepsilon, T_e) \quad 2.7$$

$$F_G(\varepsilon, \varepsilon_o, \sigma) = \frac{1}{\sqrt{2\pi}\sigma} \exp\left(\frac{-(\varepsilon - \varepsilon_o)^2}{2\sigma^2}\right) \quad 2.8$$

The last thing necessary to complete the creation of a synthetic spectrum is to add broadening to the lines. Broadening in an experimental spectrum comes from three main sources: Doppler broadening due to the movement of the ions, natural broadening due to the finite lifetime

of the state, and lastly from instrumental broadening which comes from limits on the resolution of the spectra due to the physical nature of the recording device. The SCRAM code uses Voigt line profiles to account for these effects. More details can be found in Hansen 2003.

The models used in this dissertation can largely be grouped into K-shell and L-shell models. The following sections will describe the different groups and provide information on how the models are used to estimate plasma conditions.

2.4.1 K-shell Models

The K-shell models used in this dissertation are Al, Mg, and Fe. K-shell radiation is defined as radiation from transitions that end in the $n=1$ shell or K-shell. These transitions are grouped into two categories: ionic transitions and characteristic transitions. Ionic transitions come from ions that are ionized to have very few electrons left such as 1, 2, or 3. These transitions radiate from “hotter” plasma for a given element and occur normally for sufficiently high temperatures depending on the element. Characteristic transitions come from ions that are less ionized and would typically have filled K-shells. For these ions it is possible for high energy electrons or photons to excite a K-shell electron such that a vacancy occurs lower than the more filled higher shells. In this event it is commonly referred to as a hollow ion. These hollow ions will quickly have another electron decay to fill the vacancy by producing a photon. This photon is lower in energy than a similar transition from a typical “hot” plasma as the additional electrons provide shielding from the nucleus which lowers the energy difference of the two states. The closer the electron is to the nucleus the greater the effect. For this reason transitions that are called satellite transitions can be seen near the ionic lines if there is a colder plasma with a hotter region inside.

Table 2.1. Transitions and wavelengths for diagnostically important K-shell Al and Mg lines.

Line Label	Transition	Al $\lambda(\text{\AA})$	Mg $\lambda(\text{\AA})$
Intercombination (I.C.)	$1s2p^3P_1 \rightarrow 1s^2^1S_0$	7.8070	9.2312
He α	$1s2p^1P_1 \rightarrow 1s^2^1S_0$	7.7578	9.1695
Ly α	$2p^1^2P_{1/2,3/2} \rightarrow 1s^2^1S_{1/2}$	7.1709	8.4192
He β	$1s3p^1P_1 \rightarrow 1s^2^1S_0$	6.6349	7.8507
He γ	$1s4p^1P_1 \rightarrow 1s^2^1S_0$	6.3140	7.4733
Ly β	$3p^2P_{1/2,3/2} \rightarrow 1s^2^1S_{1/2}$	6.0525	7.1058

The first K-shell models that will be discussed are ionic Al and Mg which were previously created to study Z-pinch plasmas (Yilmaz 2009). The Al and Mg models include ground states for all ionizations and have additional details for H-like, He-like and Li-like ionizations. Singly excited states up to $n=6$ are included for H-like, up to $n=5$ for He-like, and up to $n=4$ for Li-like. Al and Mg plasmas discussed in this dissertation are dominated by H-like and He-like ions and the most useful lines for diagnosing these plasma are described in Table 2.1.

Figure 2.3 displays five synthetic K-shell Al spectra in which the electron temperature, T_e , was varied (200 – 600 eV) while all other parameters were held constant ($N_e = 1 \times 10^{20} \text{ cm}^{-3}$, no hot electrons). The lines described in Table 2.1 are labeled. Figure 2.3 highlights how changing the electron temperature of the plasma affects the spectra. The most significant changes can be noticed by comparing the relative intensities of the H-like lines (Ly α and Ly β) with the He-like and Li-like lines. Electron temperature has the biggest effect on the ionization balance and therefore comparing the relative intensities of lines from different ionization stages provides insight into the T_e of the plasma. The relative intensities of the He α and Ly α lines are the primary tool for determining the T_e of optically thin K-shell plasma. When the plasma is optically thick, the less intense He-like and H-like lines are compared.

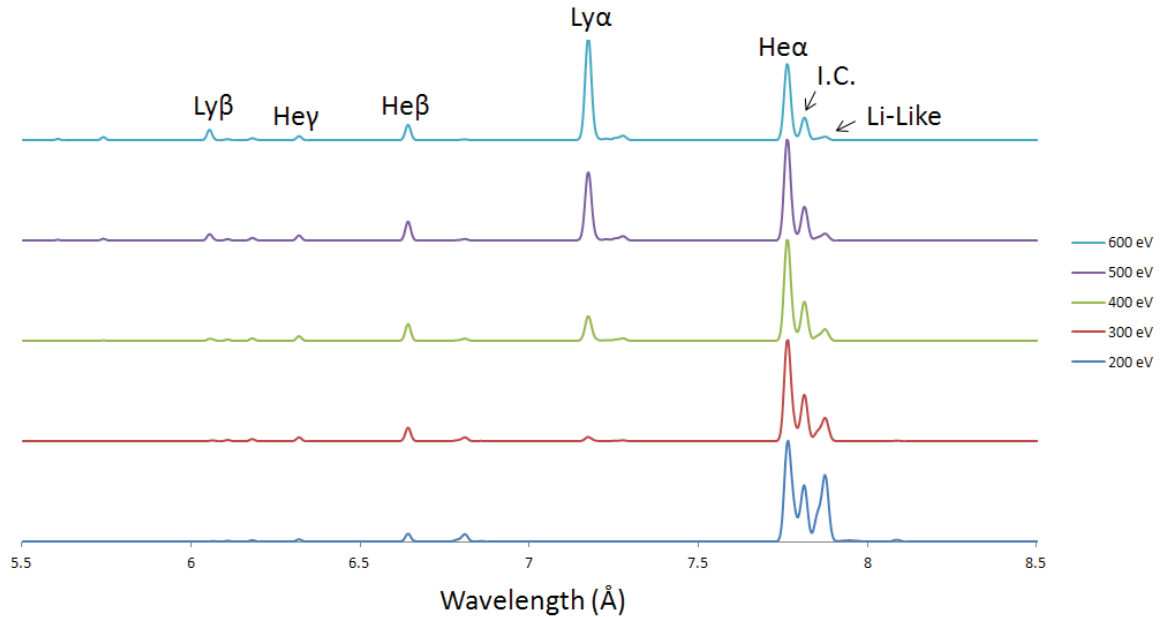


Figure 2.3. A series of synthetic spectra for ionic K-shell Al displaying the T_e dependence. N_e was constant at $1 \times 10^{20} \text{ cm}^{-3}$ and hot electrons were not included. Diagnostically important lines are identified.

Figure 2.4 shows four synthetic K-shell Al spectra with the electron density changing ($10^{18} - 10^{21} \text{ cm}^{-3}$) while the other parameters were held constant ($T_e = 400 \text{ eV}$, no hot electrons). Again the important lines are labeled. When the electron density was varied the most prominent change occurred in the relative intensity of the intercombination line (I.C.). The I.C. line is like the He α line but the spin states of the electrons are different. The initial states for these transitions are influenced by collisional processes to significantly different levels. For this reason the relative intensity of the He α and I.C. lines was used to estimate N_e .

While only Al spectra were shown the same trends are true for all ionic K-shell radiation. The differences are in the location of the lines and the specific values necessary to achieve K-shell radiation. For example, K-shell Mg would have lower T_e to achieve similar structures as seen in Figure 2.3 and the lines would be at larger wavelengths as stated in Table 2.1.

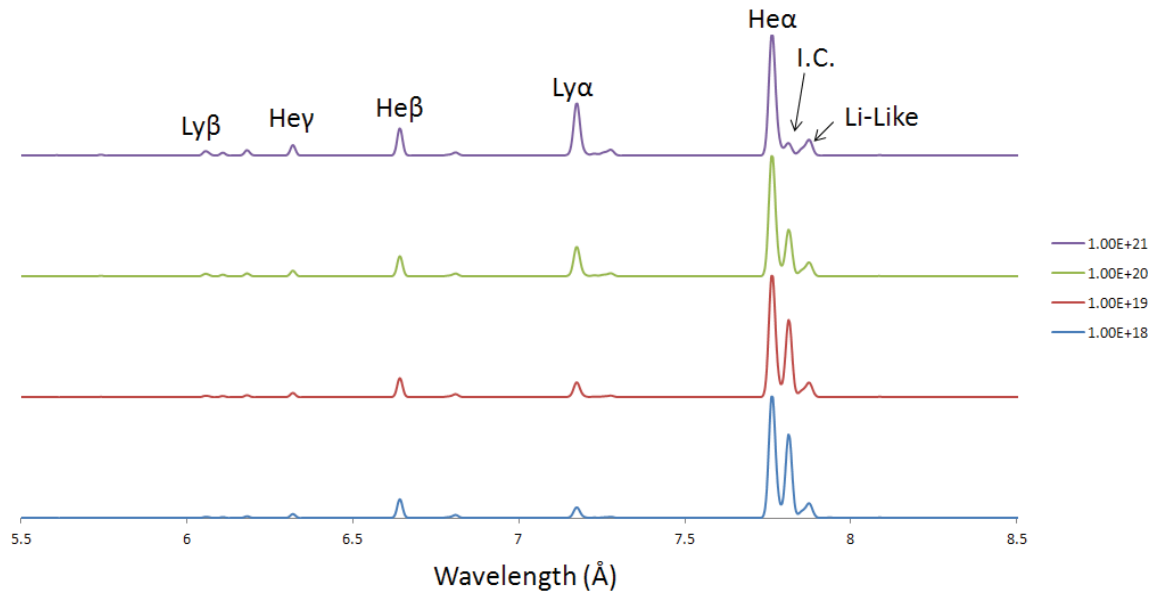


Figure 2.4. Synthetic ionic K-shell Al spectra with varying N_e to show the electron density dependence. N_e are in units of cm^{-3} , the T_e was held constant at 400 eV, and hot electrons were not included. Diagnostically important lines are identified.

The next models used are a characteristic K-shell Fe model and a characteristic/ionic Fe model. The two models were used: a “cold” $K\alpha$ model that focuses on K-shell radiation from near neutral ions of Fe, and an ionic Fe model that includes K-shell transitions for ionization levels between Al-like and H-like (Ouart 2010). The cold $K\alpha$ model includes ground states for all ionization levels with excited states focusing on the K- to Fe-like ionization levels. Singly excited states up to $n=3$ were included for the K- to Fe-like ionization levels. The ionic model includes ground states for ionization levels from bare to neutral, while excited states for H-like to Al-like were detailed with the largest focus being on O-like to Al-like states. For K-shell transitions, singly excited states up to $n=6$ were used for H-like ions, $n=5$ for He- and Li-like ions, and up to $n=4$ for Be- to F-like. Doubly excited states were included for He- and Li-like ions up to $n=3$ and for Be-like up to $n=2$.

Characteristic radiation is not dominated by a small number of specific transitions like the ionic radiation. Instead clusters of lines from each ionization level combine to create peaks.

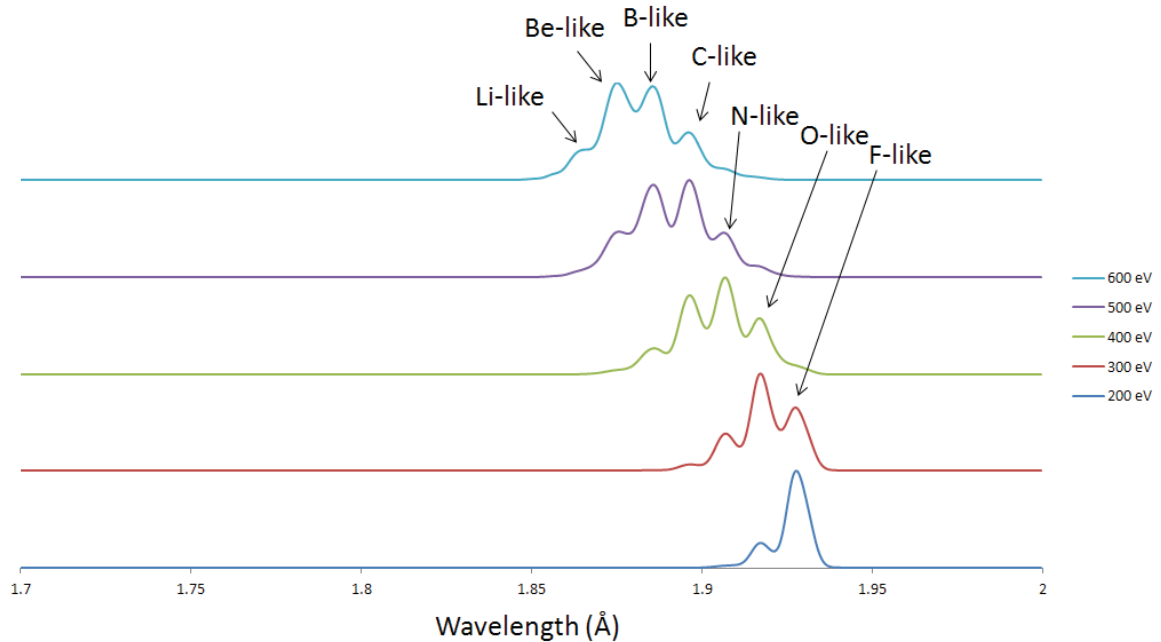


Figure 2.5. A series of synthetic spectra for characteristic K-shell Fe displaying the T_e dependence. N_e was constant at $1 \times 10^{20} \text{ cm}^{-3}$ and hot electrons were not included. Clusters from important ionization levels are identified.

Characteristic lines are labeled by the ionic transition type they are most similar to. Characteristic lines from transitions from the $n=2$ to $n=1$ state are called $K\alpha$ lines, while lines from $n=3$ to $n=1$ transitions are called $K\beta$ lines. Figure 2.5 shows $K\alpha$ spectra from the ionic Fe model with the clusters from each ionization level identified. The spectra have different T_e (200 – 600 eV) to highlight the electron dependence of characteristic radiation. Increasing the T_e shifts the ionization balance to higher ionization levels. Therefore T_e is determined by identifying the dominant ionization levels in the spectrum.

Figure 2.6 shows synthetic spectra with varying hot electron concentrations (1% - 20%) to demonstrate the effects of hot electrons. The hot electrons were given a 10 keV Gaussian temperature with a 50 eV half width at half max (HWHM). The T_e was consistent at 100 eV and the N_e was consistent at 10^{20} cm^{-3} . Increasing the hot electron concentration increases the ionization similar to increasing the T_e . However, the hot electrons also increase the ionization

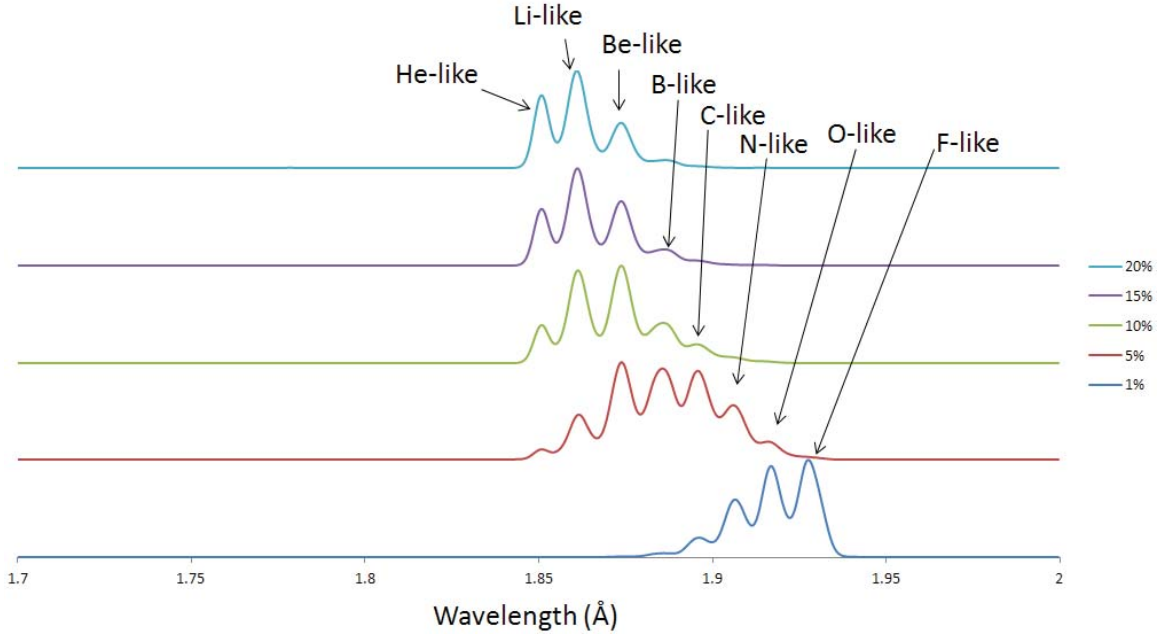


Figure 2.6. A series of synthetic spectra for characteristic K-shell Fe displaying the hot electron dependence. N_e was constant at $1 \times 10^{20} \text{ cm}^{-3}$ and T_e was constant at 100 eV. Clusters from important ionization levels are identified.

spread. This can be seen by the larger number of ionization levels present when hot electrons are included.

For analysis of satellite structures from K-shell Mg spectra discussed in Chapter 5, atomic data was provided by Dr. Ulyana Safronova. Dielectronic recombination related atomic data was collected using the quasi-relativistic many-body perturbation theory (MZ) code (Vainshtein *et al* 1980) for He-like transitions and the Hartree-Fock-Relativistic method (COWAN code) for Li- and Be-like transitions. Synthetic spectra were created by calculating an effective emission coefficient, C_S^{eff} , as described in Equations 2.9 and 2.10.

$$C_S^{eff}(j, i) = 3.3 \times 10^{-24} \left(\frac{I_H}{kT_e}\right)^{3/2} \frac{Q_d(j, i)}{g_o} \times \exp\left(-\frac{E_s(i)}{kT_e}\right) \text{ photons cm}^3 \text{ s}^{-1} \quad 2.9$$

$$Q_d(j, i) = \frac{g(i)A_a(i, i_o)A_r(j, i)}{\sum_{i'_0} A_a(i, i'_0) + \sum_k A_r(k, i)} \quad 2.10$$

Here, j denotes the bound state, i is the autoionizing state, i_0 is the initial state (that is, the ground state $1s$ of H-like Mg), and i'_0 is the possible final state for autoionization, which in our case was same as i_0 . The statistical weight of the doubly excited state is $g(i)$, $A_d(i, i_0)$ is the rate of autoionization from i to i_0 , $A_r(j, i)$ is the radiative rate from i to j . I_H is the ionization potential of hydrogen, $E_s(i)$ is the energy of the autoionizing state i relative to $1s$, and T_e is the electron temperature. The statistical weight of the initial state, i_0 , is $g_0 = 1$. C_S^{eff} is used as the intensity value for the given transition. After calculating all the C_S^{eff} values, the synthetic spectra were created by multiplying the C_S^{eff} value with a broadening term. The broadening term used was a Gaussian distribution as described in Equation 2.8. For this situation, ϵ_0 is the wavelength of the transition and ϵ is the wavelength of the spectrum. σ is adjusted to match the synthetic spectrum with the experimental spectrum. The sum of all the C_S^{eff} with their broadening terms created the synthetic spectrum. A final magnitude adjustment factor was included to match the intensity of the synthetic spectrum with the experimental spectrum.

An ionic/characteristic K-shell Ti model was created for use with the Ti X-pinch experiments described in Chapter 4. The model uses atomic data from FAC and uses SCRAM to calculate population levels and create synthetic spectra. A total of 2552 states were included. Ground states for all ionization levels are included. Singly excited states up to $n=6$ are included for H-like ions, up to $n=5$ for He- and Li-like ions, and up to $n=4$ for Be- to Ne-like ions. Doubly excited states up to $n=3$ are included for He- and Li-like ions, and up to $n=2$ for Be- to F-like ions. The example of K-shell Ti calculated with $T_e = 3000$ eV and $N_e = 1 \times 10^{20}$ cm⁻³ is displayed in Figure 2.7. Diagnostically important He- and H-like lines are labeled and the presence of the Ly α line occurs for high electron temperatures >1.5 keV.

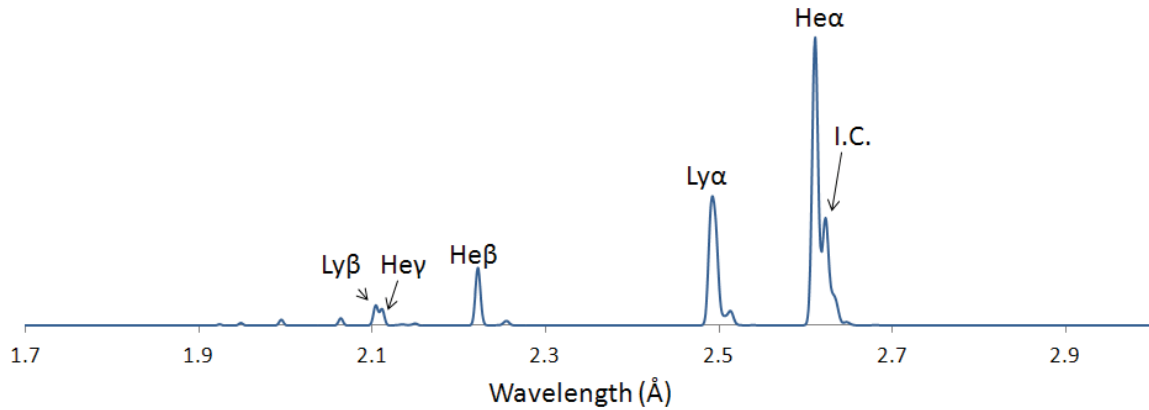


Figure 2.7. A sample Ti spectrum produced with $T_e = 3000$ eV and $N_e = 1 \times 10^{20}$ cm $^{-3}$.

2.4.2 L-shell Models

The L-shell models used in this dissertation are Ni and Cu. While not shown in this dissertation, L-shell Fe modeling was also done to assist collaborators with their research. L-shell radiation is defined as radiation from transitions that end in the $n=2$ shell or L-shell. These

Table 2.2. Transitions and wavelengths for diagnostically important L-shell Cu and Ni lines.

Line Label	Transition	Ni λ (Å)	Cu λ (Å)
Ne-like 4C	$1s^2 2s^2 2p^5 4d \ ^1P_1 \rightarrow 1s^2 2s^2 2p^6 \ ^1S_0$	9.984	9.115
Ne-like 4D	$1s^2 2s^2 2p^5 4d \ ^3D_1 \rightarrow 1s^2 2s^2 2p^6 \ ^1S_0$	10.117	9.245
O-like O1	$1s^2 2s^2 2p^3 3d \ ^3P_2 \rightarrow 1s^2 2s^2 2p^4 \ ^3S_2$	11.302	10.393
Ne-like 3A	$1s^2 2s 2p^6 3p \ ^1P_1 \rightarrow 1s^2 2s^2 2p^6 \ ^1S_0$	11.514	10.580
Ne-like 3B	$1s^2 2s 2p^6 3p \ ^3P_1 \rightarrow 1s^2 2s^2 2p^6 \ ^1S_0$	11.570	10.638
F-like F1	$1s^2 2s^2 2p^4 3d \ ^2D_{5/2} \rightarrow 1s^2 2s^2 2p^5 \ ^2P_{3/2}$	11.828	10.857
Ne-like 3C	$1s^2 2s^2 2p^5 3d \ ^1P_1 \rightarrow 1s^2 2s^2 2p^6 \ ^1S_0$	12.435	11.390
Na-like Na1	$1s^2 2s^2 2p^5 3s 3d \ ^2F_{5/2} \rightarrow 1s^2 2s^2 2p^6 3s \ ^2S_{1/2}$	12.581	11.514
Ne-like 3D	$1s^2 2s^2 2p^5 3d \ ^3D_1 \rightarrow 1s^2 2s^2 2p^6 \ ^1S_0$	12.661	11.607
Na-like Na2	$1s^2 2s^2 2p^5 3s 3d \ ^2P_{1/2} \rightarrow 1s^2 2s^2 2p^6 3s \ ^2S_{1/2}$	12.824	11.737
Ne-like 3F	$1s^2 2s^2 2p^5 3s \ ^1P_1 \rightarrow 1s^2 2s^2 2p^6 \ ^1S_0$	13.797	12.591
Ne-like 3G	$1s^2 2s^2 2p^5 3s \ ^3P_1 \rightarrow 1s^2 2s^2 2p^6 \ ^1S_0$	14.064	12.849

models were previously created for Z-pinch plasma radiation analysis (Ouart 2010). These models include ground states for all ionization levels and singly and doubly excited states for H- to Al-like ionization levels. The singly excited states are included up to $n=6$ for H-like ions, $n=5$ for He- to Li-like ions, Ne- and Na-like ions, and $n=4$ for Be- to F-like ions, and Mg- and Al-like ions. The doubly excited states include up to $n=3$ for He-, Li-, Na-, Mg-, and Al-like ions, and with $n=2$ for Be-like ions. The diagnostically important lines are listed in Table 2.2.

Figure 2.8 shows the T_e dependence of L-shell Ni. The T_e varies between 200 and 400 eV and the N_e is kept constant at 10^{20} cm^{-3} . At 200 eV the spectra is primarily Ne- and Na-like lines. As the T_e is increased, F-like lines become more significant and the Na-like lines fade. The relative intensities of lines from different ionization levels is how the T_e is determined. The 3C line is the most susceptible to opacity and is therefore not usually used as a reliable line. The 4C and 4D lines are usually optically thin and thus are used to scale the intensity of the theoretical

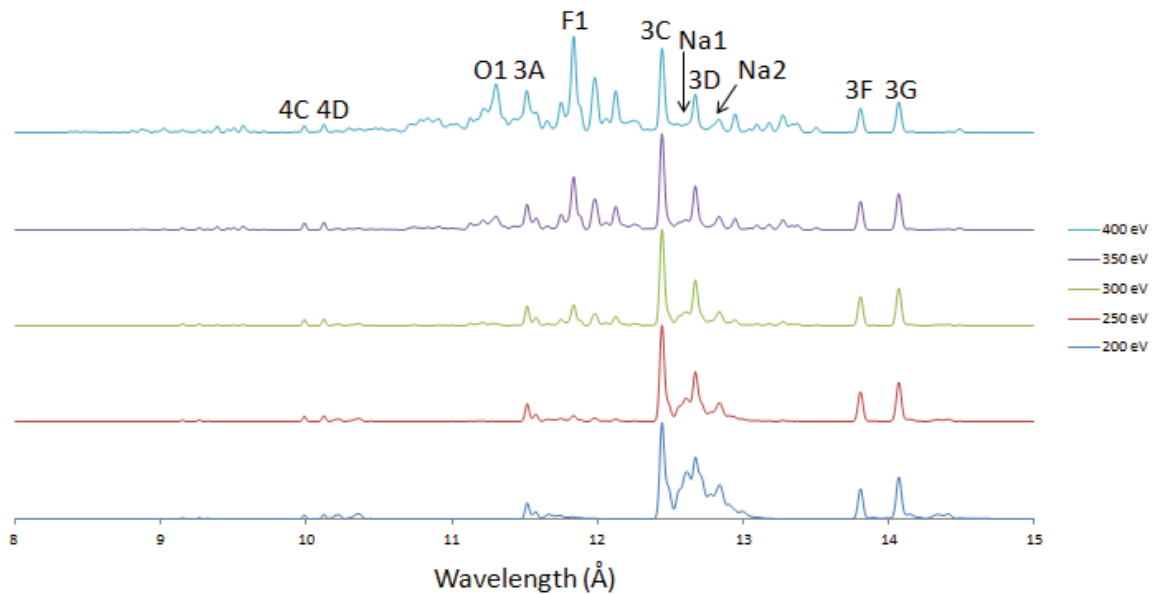


Figure 2.8. A series of synthetic spectra for L-shell Ni displaying the T_e dependence. N_e was constant at $1 \times 10^{20} \text{ cm}^{-3}$ and hot electrons were not included. Diagnostically important lines are identified.

spectra. The F1 line and the Na1 and Na2 lines are compared to the 4C and 4D lines to estimate the T_e of the plasma.

Figure 2.9 highlights the N_e dependence of L-shell Ni. The N_e is varied between 10^{18} and 10^{20} cm^{-3} while the T_e is held constant at 300 eV. The lines most affected by changes to the N_e are the 3A, 3F, and 3G lines. The 3F and 3G lines are the preferred lines to use for N_e diagnosing. However, these lines are frequently outside the detectible spectral range for time gated spectra and therefore the 3A line is used in those situations.

While only L-shell Ni is displayed, L-shell Cu follows the same trends with only the line location and specific values for T_e and N_e varying. L-shell Cu will have lower wavelengths, and higher T_e values are necessary to achieve similar structure as seen in Figures 2.8 and 2.9.

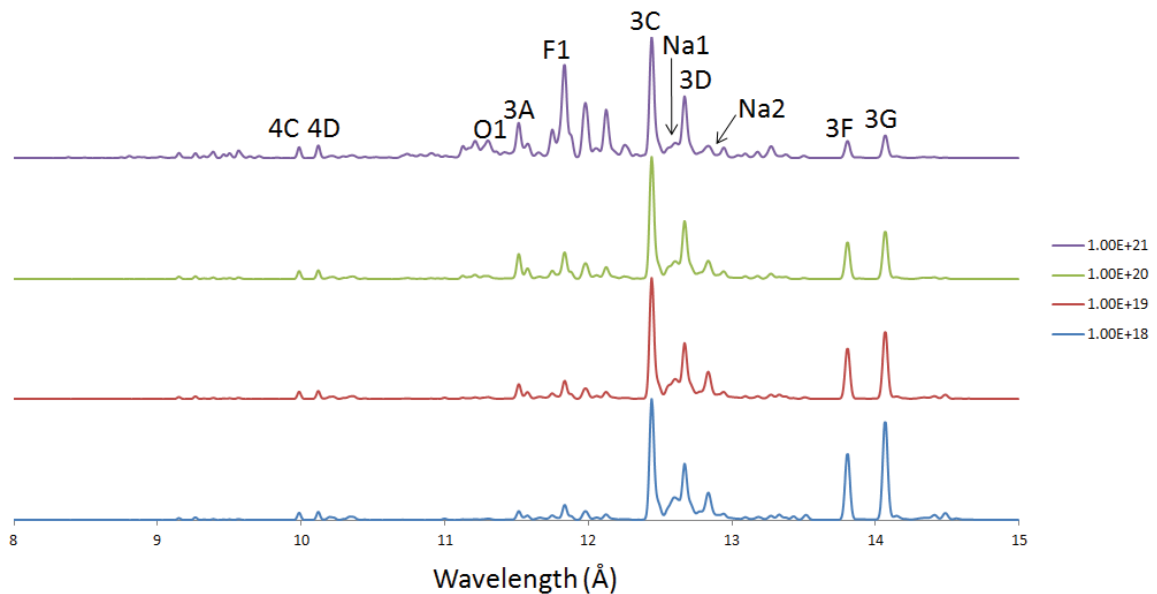


Figure 2.9. Synthetic L-shell Ni spectra with varying N_e to show the electron density dependence. N_e are in units of cm^{-3} , the T_e was held constant at 300 eV, and hot electrons were not included. Diagnostically important lines are identified.

Chapter 3

Radiative Properties of Precursor Columns from CWAs at 1 –

1.7 MA Current

3.1 Introduction to Precursor Plasmas Produced by CWAs

A cylindrical wire array (CWA) is an array of wires set up in a pattern of uniform spacing around a central axis. The wires are then subjected to a large current, typically on the order of MA, which causes the wires to ionize into plasma in a process called ablation. A common property of CWAs is a precursor plasma column that forms on the central axis. Ablated plasma from the wires is pulled onto the axis due to the $J \times B$ Lorentz force and builds up creating its own radiation burst before the wires implode. As the wires ablate, eventually the magnetic fields created by the current cause the wires to be pulled into the central axis. The imploding wires create an intense burst of radiation including a large amount of x-rays. CWAs have been an area of interest for their relevance to high energy density physics (Matzen *et al* 2005), inertial confinement fusion (Cuneo *et al* 2006), and astrophysics. CWA precursor plasma columns have been studied in extensive detail including: observation of precursor plasma column creation from multiple materials (Deeney *et al* 1995 and Yadlowsky *et al* 1996), understanding precursor column formation due to ablated plasma stagnating on the central axis (Lebedev *et al* 1998 and Chittenden *et al* 1999), and CWA size (Coverdale *et al* 2002).

The most detailed research into precursor plasmas was done by a series of experiments at the Mega Ampere Generator for Plasma Implosion Experiments (MAGPIE) at Imperial College London detailed in Bott *et al* 2006. These experiments were done with a 1 MA current with a 240 ns rise time. These experiments included many materials (Al, W, Ni, Cu, Ti, and Mo) and number

of wires (8, 16, 32, and 64) of various sizes to investigate many different facets of precursor columns. Some of the most significant findings were the interaction of ablated plasmas between the wires and the central axis (Bott *et al* 2006), precursor column diameter evolution in time (Lebedev *et al* 2001 and Bott *et al* 2006), and percentage of the current passing through the precursor column.

While the MAGPIE experiments were extensive, one area that was not fully explored was the plasma electron temperature, T_e , of the precursor column. The only estimates of the T_e of the precursor column were inferred using extreme ultraviolet (EUV) spectra. These estimates were 50-60 eV for Al precursor columns. Coverdale *et al* 2009 performed collaborative experiments at UNR using low wire number CWAs with an x-ray time gated spectrometer focused on the precursor column to determine how hot the precursor columns could be (Coverdale *et al* 2009). Ni-60 (94% Cu and 6% Ni) wires were used and modeling of the collected L-shell Cu spectra found the precursor columns have much higher than expected $T_e > 300$ eV. This chapter will detail the continued research into precursor columns that extends from the discovery of relatively hot temperatures for precursor column plasmas.

3.2 Mid-Atomic Number CWAs at Standard Current

Mid-atomic number, or mid-Z, elements are elements with atomic numbers around 22-30. Experiments with low wire number (6 wires) mid-Z CWAs were conducted to examine the plasma parameters of the precursor columns. Table 3.1 provides a list of some of the mid-Z CWA experiments. These experiments were performed on the Zebra Generator, described in Section 2.1, to determine if the hot precursor plasma seen in Coverdale *et al* 2009 is consistent for other mid-Z elements. There were three main wire materials used for these experiments: Cu, Brass (70% Cu and 30% Zn), and Alumel (95% Ni, 2% Al, 2% Mn, and 1% Si). Each experiment

Table 3.1. A list of mid-Z element CWA experiments performed on the Zebra Generator at standard current (1 MA) with some experimental parameters included.

Shot Number	Material	Wire thickness (μm)	Total Linear Mass of the Array ($\mu\text{g/cm}$)	Total Radiation Yield (kJ)
2151	Cu	10	44	20.5
2153	Brass	10	44	20.6
2157	Alumel	10	43	17.1
2772	Alumel	10	43	18.1

included all available diagnostics with an emphasis on time gated diagnostics (time gated pinhole cameras, spectrometers, etc.) that were triggered while the precursor column was most prominent. While experiments for each material provided data for analysis of the precursor plasma, the Cu experiments were useful for comparison with the Ni-60 experiments and the Alumel experiments were the best precursor plasma radiators. Cu and Alumel loads will be the focus for presenting the mid-Z CWA precursor column results.

3.2.1 Cu CWA at Standard Current

The first experiment performed was a Cu CWA imploded with standard current. This CWA was composed of 6 Cu wires of thickness 10 μm evenly spaced in a circular pattern with a diameter of 12 mm. The total linear array mass was 44 $\mu\text{g/cm}$. This experiment produced a total radiation yield measured by the bolometer of 20 kJ. Figure 3.1a shows photo conducting diode (PCD) (cutoff energy, >750 eV) and current signals for the 1 MA Cu CWA. The total energy measured by the PCD was 470 J, which is estimated by integrating the PCD signal from first rise of the signal to when the signal returns to noise. The integrated value is then multiplied by a calibration constant for the diode. The portion due to the precursor was 14 J or 3%, calculated from first rise in signal for the precursor to the end of the drop in signal for the precursor. The PCD signals show a small peak (4 ns full width at half max, FWHM) at the origin that increases and decreases before a much more intense peak at 21 ns. The smaller peak is due to radiation

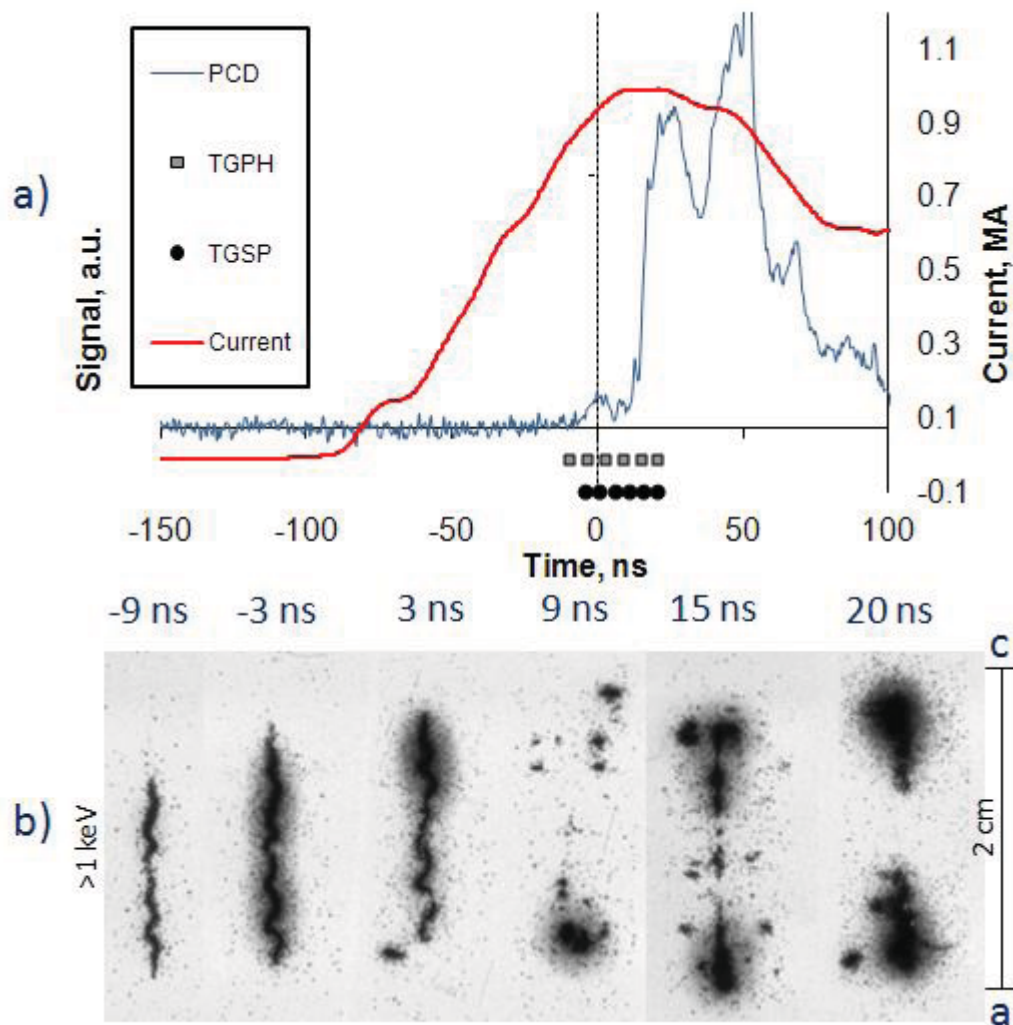


Figure 3.1. a) Signals for 1 MA Cu CWA including: current, PCD, x-ray time gated pinhole images (TGPH), and x-ray time gated spectra (TGSP). b) X-ray time gated pinhole images for energies >1 keV. Times are relative to the precursor PCD peak. Anode to cathode gap is 2 cm.

from the precursor, confirmed by the x-ray pinhole images, while the high intensity peaks that follow are from the implosion of the wires. Timings for x-ray time gated pinhole images and spectra are displayed. The x-ray time gated pinhole images and spectra were set to trigger during the precursor peak and lead into the wire implosion. Figure 3.1b shows the x-ray time gated pinhole images for >1 keV energies and the time relative to the first PCD peak from the precursor plasma. The first pinhole image, which occurs at approximately -9 ns, shows a thin precursor plasma column, estimated diameter of 1 mm, with pronounced magnetohydrodynamic

instabilities (see, for example, Coverdale *et al* 2009). This column grows in intensity adding a less intense cloud around the column, drops in intensity, and then breaks up around 9 ns. A new column begins to form at 15 ns and becomes an intense column at 20 ns. The gap in the middle of the last pinhole image is due to a defect in the MCP.

Figure 3.2 displays the x-ray time gated spectra with timings. The x-ray time gated spectra start at -4 ns with only small signals of L-shell Cu radiation. The next frame shows prominent L-shell Cu radiation which increases in the following frame and then disappears afterwards. In the final two frames, which are closer to the main x-ray burst, the L-shell Cu returns with increasing intensity and strong background radiation as the wires reach the center. Lineouts were taken for each frame during the precursor phase and modeled using a non-local thermodynamic equilibrium (non-LTE) kinetic model described in Section 2.4.1. The model parameters were chosen by matching the intensity of the 4C and 4D (4-2 Ne-like transitions) lines for scaling. Then the electron density parameter was adjusted to match the 3A (3-2 Ne-like transition) line, while the electron temperature was adjusted to match the F-like (3-2 F-like

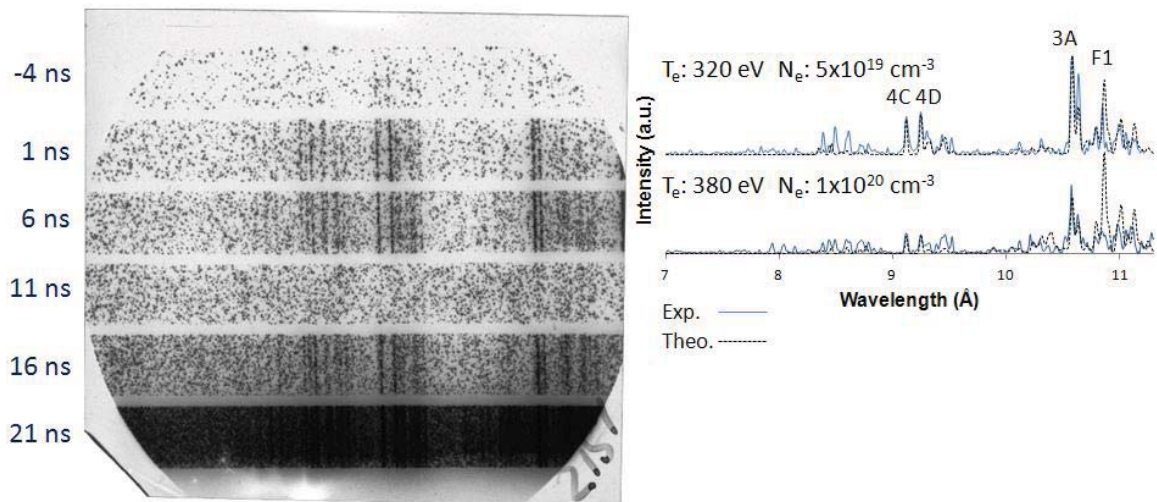


Figure 3.2. X-ray time gated spectra for Cu CWA. Times for spectra are relative to the precursor PCD peak. Spectra from precursor radiation are shown compared to modeling from a Cu non-LTE kinetic model with electron temperature (T_e) and density (N_e) estimates.

transitions) lines on the high wavelength side of the 3A transition. The modeling suggests T_e starting at 320 eV for the first precursor spectrum and rising to 380 eV for the last precursor spectrum before the L-shell Cu disappears. The electron density starts at $5 \times 10^{19} \text{ cm}^{-3}$ and rises to $1 \times 10^{20} \text{ cm}^{-3}$. By combining the plasma size from the pinhole images with the electron density from the modeling, an estimation of the L-shell radiating mass can be made. The L-shell radiating mass for the precursor was calculated to be up to 2% of the total array mass, which is consistent with Coverdale *et al* 2009. This modeling suggests the higher electron temperatures for precursor plasmas from Ni-60 CWAs are also found for pure Cu CWAs.

3.2.2 Alugel CWA at Standard Current

Alugel is a Ni alloy with 95% Ni, 2% Al, 2% Mn, and 1% Si. Alugel CWA experiments were performed using 6 wires and 12 mm diameter configuration, the same as used in the Cu CWA experiments. 10 μm diameter wires were used which constituted a 43 $\mu\text{g}/\text{cm}$ total linear array mass. The total radiation yield for the Alugel CWA experiment was 17 kJ (repeatable to 15%). The PCD and current signals for the Alugel CWA experiment can be seen in Figure 3.3a. Alugel CWAs show much more prominent precursor radiation (11 ns FWHM) relative to the main implosion. In the PCD signal, the strong precursor radiation peaks at the origin and decreases before the main implosion which first peaks at 30 ns. The total energy measured by the PCD was 566 J, with the precursor providing 70 J or 12%. The x-ray time gated pinhole images and spectra were triggered to start early in the formation of the precursor column and record the evolution of the plasma until the PCD signal rise attributed to the beginning of the main implosion. Figure 3b shows the x-ray time gated pinhole images with their timings. The pinhole images started with a high intensity column at -15 ns that grew more intense until -3 ns. Estimates of the size of the high intensity region of the column suggest a diameter as big as 1.5 mm. The column was around 50% thicker for the Alugel experiment than the Cu experiment and the

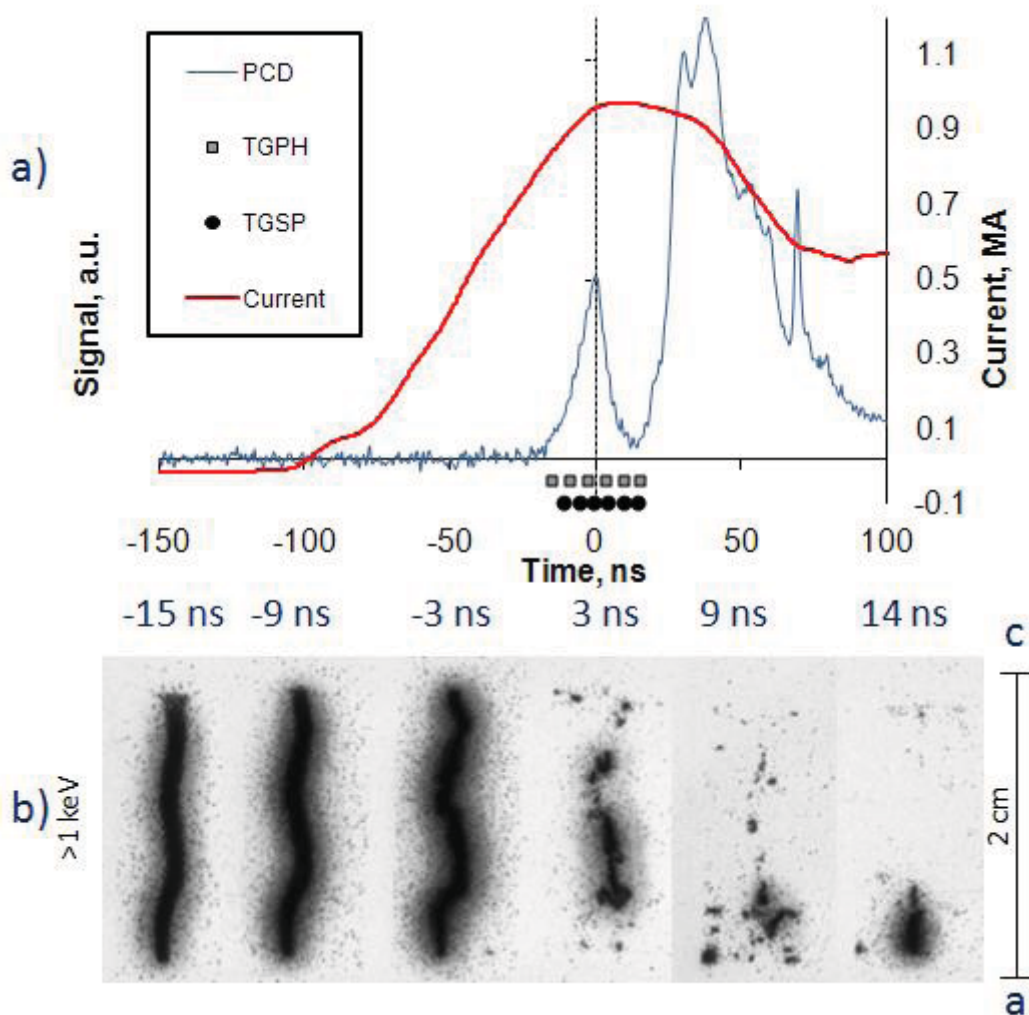


Figure 3.3. a) Signals for 1 MA Aludel CWA including: current, PCD, x-ray time gated pinhole images (TGPH), and x-ray time gated spectra (TGSP). b) X-ray time gated pinhole images for energies $>1\text{keV}$. Times are relative to the precursor PCD peak. Anode to cathode gap is 2 cm.

instabilities of the Aludel precursor have a longer wavelength. After -3 ns the column started dispersing before the intensity began to increase with the onset of the main implosion. As with the Cu CWA experiment the last frame of the pinhole image was affected by a defect of the MCP in the middle.

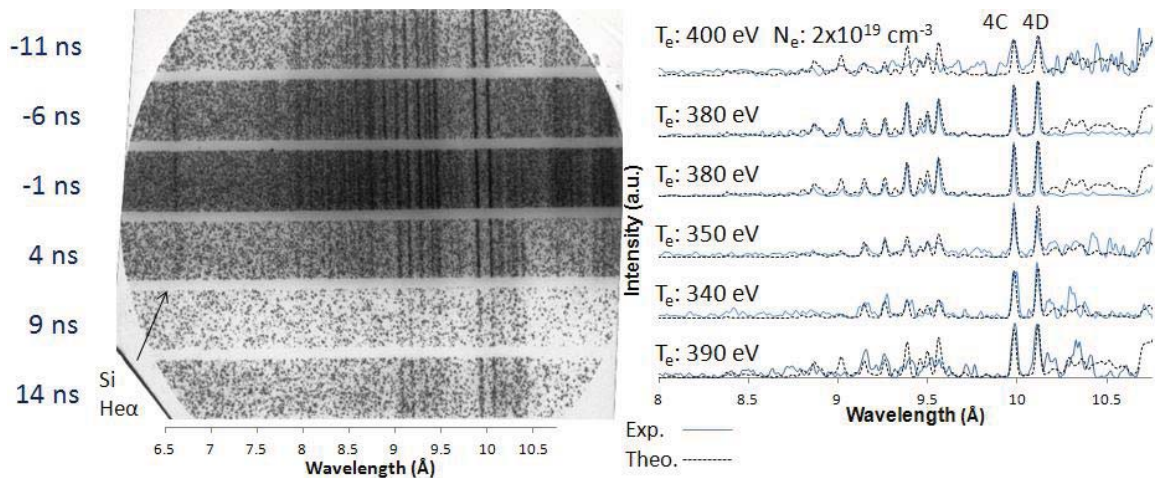


Figure 3.4. X-ray time gated spectra for Aludel CWA. Times for spectra are relative to the precursor PCD peak. Spectra from precursor radiation are shown compared to modeling from a Ni non-LTE kinetic model with electron temperature (T_e) and density (N_e) estimates.

In Figure 3.4, the x-ray time gated spectra recorded the early stages of precursor radiation as seen in the PCD signal and ended with the PCD signal rise attributed to the beginning of the main implosion. The spectra showed an increase and fade in intensity that correlated with the PCD signal. Non-LTE kinetic modeling of the L-shell Ni indicated an electron temperature of ~ 400 eV for the earliest timing (-11 ns). The electron temperature then decreased to about 340 eV (-1 ns) before increasing to about 390 eV (14 ns). The density was kept constant at $2 \times 10^{19} \text{ cm}^{-3}$ which is a common electron density for Z-pinch plasmas. This was done because there were not good density diagnostic lines in the spectral region available. The density was chosen by comparing the precursor energy measured by the PCD with the energy estimated by using the theoretical spectrum and the size estimation of the precursor column. The electron temperature was determined by matching the line structures surrounding the 4C and 4D transition lines. The four most intense lines centered around 9.5 \AA and the lines near 9 \AA are F-like transitions. The two lines between the F-like structures are Ne-like. Again, >300 eV temperatures were observed for a mid-Z material.

3.3 Ni-60 CWAs at Enhanced Current

Upon confirming the consistently high electron temperatures for the mid-Z CWA precursor columns, additional studies were conducted through the use of the Load Current Multiplier (LCM). Ni-60 (94% Cu and 6% Ni) CWA experiments were performed at enhanced current (1.5-1.7 MA) to understand the effects of current scaling on the precursor plasma. These experiments used 6 wires and 12 mm diameter configuration. However, the use of the LCM restricted the anode to cathode gap to 1cm compared to the 2 cm gap without the LCM. For this reason, comparisons between the standard current and enhanced current experiments were done using values normalized using the anode to cathode gap for the respective experiments. The wires used were thicker than at standard current (15 μm) with a total linear mass of 100 $\mu\text{g}/\text{cm}$. The heavier mass was chosen to maximize the benefit of the enhanced current and to have a similar timing for the implosion. If the mass was the same as the standard current experiments, the array would implode before the current reached its peak. The Ni-60 CWA experiments have a total radiation yield of ~ 16 kJ (repeatable to 10%) or 16 kJ/cm when normalized to the anode to cathode gap. When the total radiation yield from the Cu CWA at standard current was normalized to the anode to cathode gap it was ~ 10 kJ/cm. This shows a $\sim 50\%$ energy increase due to the enhanced current. The PCD and current signals for a typical experiment can be seen in Figure 3.5a. A strong precursor peak (8 ns FWHM) similar to the Al₂O₃ CWA was seen in the PCD signals with a maximum at the origin while the main x-ray burst first peaked at 25 ns. The total energy measured by the PCD was 750 J, with the precursor radiation accounting for 40 J or 5%. The energy measured from the standard current Ni-60 CWA precursor column from Coverdale *et al* 2009 was 28 J. This is $\sim 50\%$ increase without taking into account the anode to cathode gap difference. The signals also display the x-ray time gated pinhole images and spectra timings which begin in the precursor radiation bump and end early during the radiation rise of the main

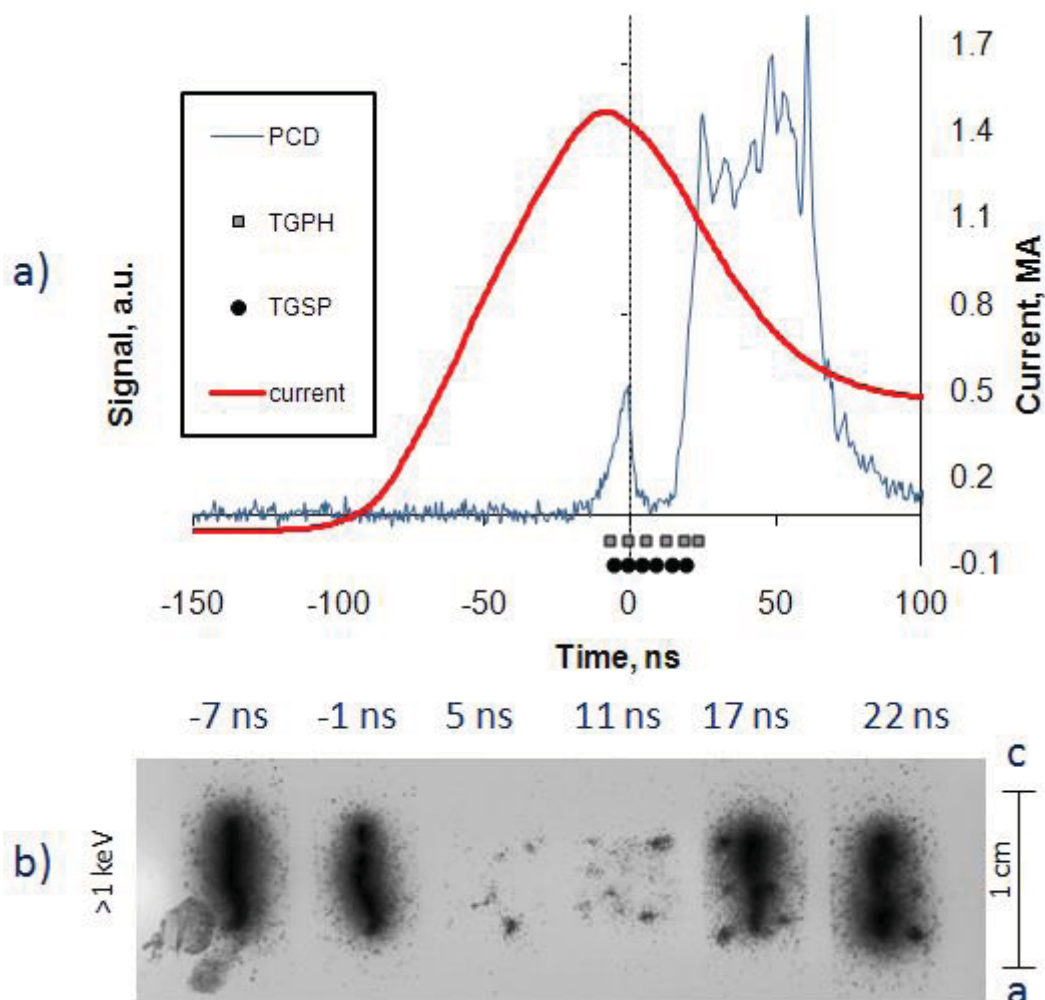


Figure 3.5. a) Signals for 1.5 MA Ni-60 CWA including: current, PCD, x-ray time gated pinhole images (TGPH), and x-ray time gated spectra (TGSP). b) X-ray time gated pinhole images for energies $>1\text{keV}$. Times are relative to the precursor PCD peak. Anode to cathode gap is 1 cm.

implosion. The x-ray time gated pinhole images are shown in Figure 3.5b. The pinhole camera recorded 2 frames of strong radiation from a column, estimated diameter of approximately 1.5 mm, followed by two frames of scattered small radiation spots. The final frames displayed strong radiation from a column along with scattered spots of radiation. This shows the change from precursor radiation to the beginning of the main implosion radiation. The diameters measured in the standard current experiments were 1 – 1.5 mm.

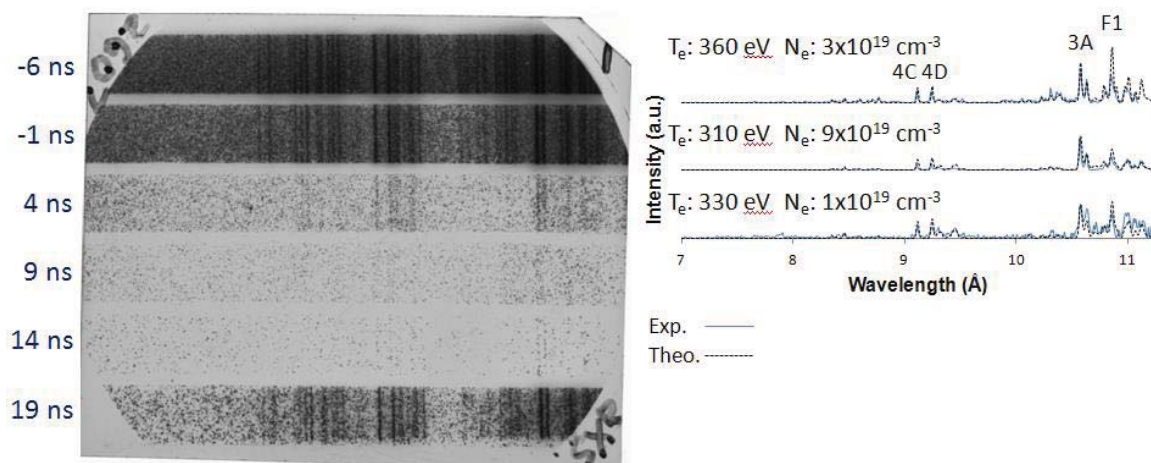


Figure 3.6. X-ray time gated spectra for Ni-60 CWA. Times for spectra are relative to the precursor PCD peak. Spectra from precursor radiation are shown compared to modeling from a Cu non-LTE kinetic model with electron temperature (T_e) and density (N_e) estimates.

In Figure 3.6, the x-ray time gated spectra began recording during the peak of the precursor plasma radiation. The intensity of the spectra decreased with the fall in radiation and mostly disappeared by the fourth frame. This continued until the end when the spectrum returned with the rise of the radiation from the main implosion. Modeling of L-shell Cu was matched to the three frames connected to the precursor plasma. The small percentage of Ni was not enough to affect the L-shell spectra. The modeling suggests electron temperatures starting at approximately 360 eV which dropped to 310 eV in the next frame. The last precursor spectrum showed a rise in temperature to 330 eV. The electron density followed a reverse trend starting at $3 \times 10^{19} \text{ cm}^{-3}$ and increasing to $9 \times 10^{19} \text{ cm}^{-3}$ before dropping to $1 \times 10^{19} \text{ cm}^{-3}$. The electron temperatures were similar to the standard current experiments; however, the densities of the standard current experiments were more consistently $\sim 1 \times 10^{19} \text{ cm}^{-3}$. Including the results of the x-ray pinhole images, comparing the standard and enhanced currents suggests the enhanced current precursor column was larger with similar electron densities and higher electron densities leading to more radiation from the precursor plasma.

3.4 Al CWA at Standard Current

After studying the effects of current scaling on precursor columns from CWAs, the next step was to examine the effects of nonuniformity in the CWAs. The Al_umel CWAs showed the most intense precursor column radiation and therefore were chosen as the dominant material for a mixed material CWA. Aluminum was chosen as a secondary material for its faster ablation rate which was expected to significantly impact the precursor column formation due to the potential for different materials to arrive at the central axis at different times and the symmetry of the implosion to be disturbed as the wires imploded at different times. In order to fully understand the changes to the precursor column in the mixed CWA, a pure aluminum CWA was necessary for comparison.

An aluminum CWA experiment was performed with the same 6 wires and 12 mm diameter configuration using standard current. Al 5056 (95% Al and 5% Mg) wires were used with a 17.8 μm diameter with a total linear mass of 40 $\mu\text{g}/\text{cm}$. The total radiation yield for the aluminum CWA was 9 kJ, which was much less than from mid-Z CWAs. Figure 3.7a shows the PCD and current signals along with the timings for the shadowgraphy images, time gated x-ray pinhole images, and time gated x-ray spectrometer. The PCD signals started to rise around 45 ns prior to the maximum of the signals which was associated with the x-ray burst from the main implosion. The signal increased to a moderate level and remained fairly consistent until the sharp increase began due to the main x-ray burst unlike the mid-Z CWAs where the precursor signal reached a peak and decreased to near zero before the main x-ray burst. Figure 3.7b depicts two shadowgraphy images taken at -17 and -10 ns relative to the maximum of the PCD signal in the precursor stage. It can be clearly seen that the 6 wires were still standing while a precursor column was being formed which confirmed the initial rise in the PCD signal was during the precursor column phase. With this knowledge the percentage of the PCD signal due to the

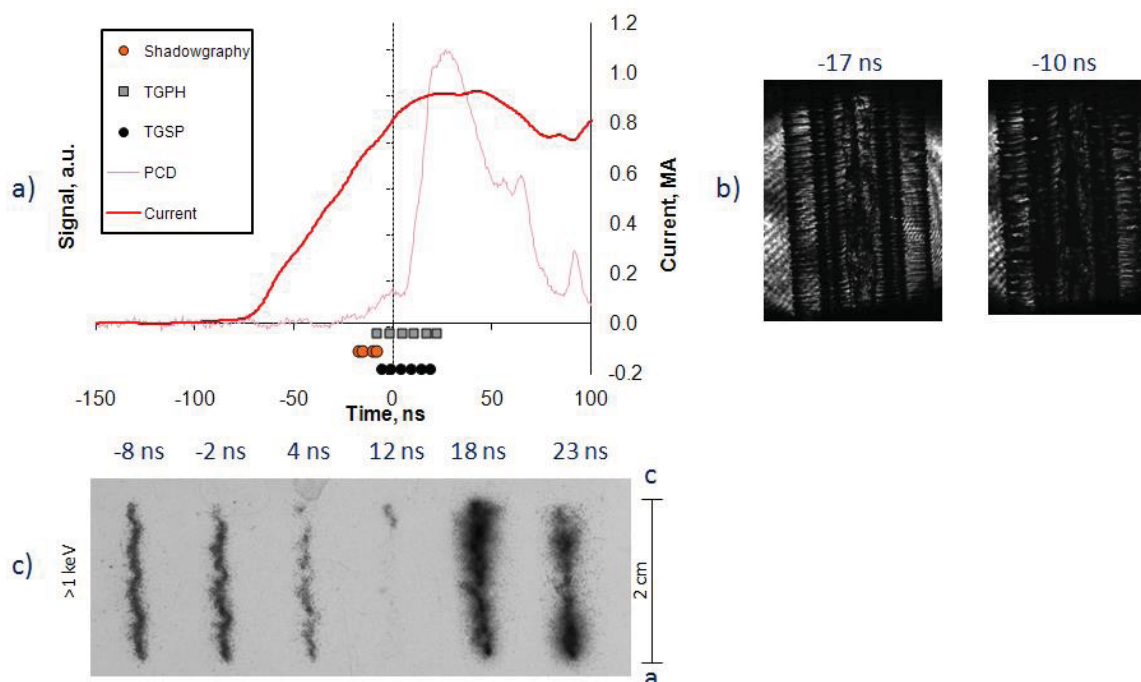


Figure 3.7. a) Signals for 1 MA Al CWA including: current, PCD, x-ray time gated pinhole images (TGPH), and x-ray time gated spectra (TGSP). b) Shadowgraphy images showing precursor column formation. c) X-ray time gated pinhole images for energies $>1\text{keV}$. Times are relative to the precursor PCD peak. Anode to cathode gap is 2 cm.

precursor phase could be determined. The precursor phase started from the first rise of the signal near -14 ns, and lasts until the sharp rise of the signal at approximately 5 ns. Through integrating the signal it was found that 4% of the signal was due to the precursor phase. Unfortunately, the PCD diode that was absolutely calibrated was not operational during the Al CWA experiments; therefore, the energy detected by the diode could not be determined. Figure 3.7c shows the x-ray pinhole images that were recorded between -8 and 23 ns. The first frame of the pinhole image corresponds to the second shadowgraphy image. The pinhole image was a fairly intense column of $\sim 1.2\text{ mm}$ thickness filling the full anode to cathode gap with instabilities that were between the short wavelengths of the Cu CWA and the longer wavelengths of the AlumeI CWA. The pinhole images then grew less intense while maintaining the instabilities. The fourth frame at 12 ns was affected by an MCP defect. The following frames then show intense thicker columns when the main implosion began.

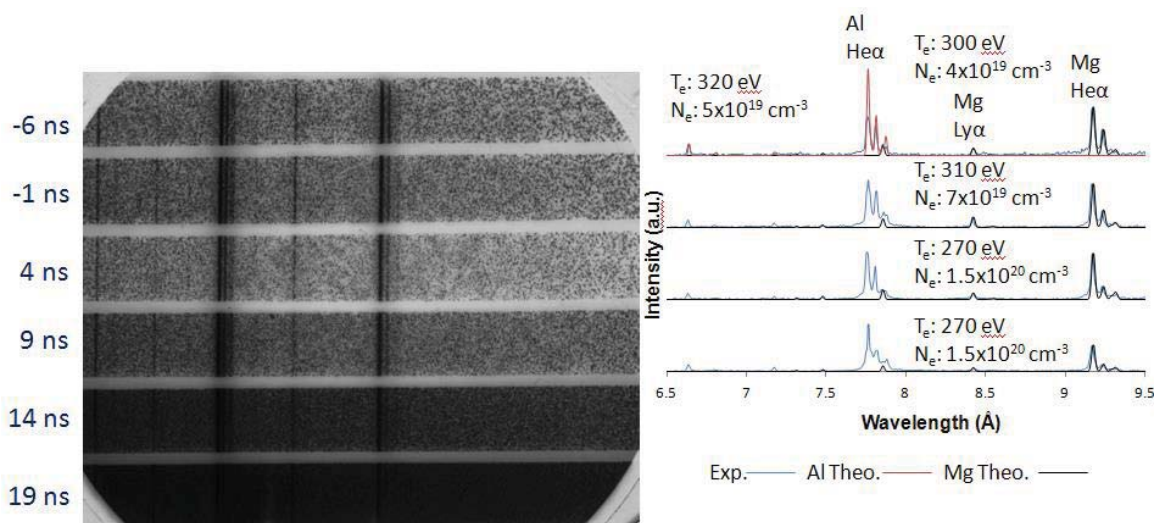


Figure 3.8. X-ray time gated spectra for Al CWA. Times for spectra are relative to the precursor PCD peak. Spectra from precursor radiation are shown compared to modeling from Al and Mg non-LTE kinetic models with electron temperature (T_e) and density (N_e) estimates.

In Figure 3.8 the x-ray time gated films that recorded the K-shell Al and Mg spectra are presented with the lineouts and modeling for each of the first four frames shown on the right. The film displays intense K-shell Al and Mg radiation throughout the frames that represent -6 to 19 ns relative to the peak of the PCD signal. While the K-shell radiation remained intense in each frame, the background radiation varied in a manner that matched the progression of the intensity in the corresponding pinhole images. The initial frame has a moderate background intensity that drops in the next two frames just like the pinhole images. The next three frames get more intense with the rise of the PCD signal and the increased pinhole image intensity.

The modeling of the spectra begins with the frame at -6 ns. The K-shell Al radiation was modeled using a $T_e = 320$ eV and a $N_e = 5 \times 10^{19} \text{ cm}^{-3}$. The model significantly over estimated the Al He α line and this was due to the model being run assuming optically thin plasma. The overestimation identifies the K-shell Al as optically thick and therefore less reliable for determining the plasma conditions. When the K-shell Al is optically thick, K-shell Mg is usually present which was the case here. Due to the small concentration of Mg (5%) in the wire material, the K-shell Mg was optically thin or not significantly present. For this reason the modeling for the

time gated spectra focused on the K-shell Mg lines. The K-shell Mg models estimated the precursor plasma T_e to be 270 – 300 eV and the N_e to be $4 \times 10^{19} - 1.5 \times 10^{20} \text{ cm}^{-3}$. The T_e of the precursor started at 300 eV and increased to 310 eV before dropping to 270 eV for the next two frames. This makes sense as the precursor column was slowly collecting material on the center axis before being flooded with large amounts of mass due to the imploding of the wires which shielded the radiation from the hot center and distributed the energy among the greater cooler mass. The N_e of the plasma started at $4 \times 10^{19} \text{ cm}^{-3}$ and steadily rose to $1.5 \times 10^{20} \text{ cm}^{-3}$ over the next two frames. This was due to the constant accumulation of the ablated mass and eventually the imploding wires. The time gated spectra results provide a good reference point for the mixed CWAs that will follow, but they also provide evidence of relatively hot precursor plasma conditions for Al CWAs that were previously inferred to be 50 – 60 eV based on extreme ultraviolet (EUV) spectra (Bott *et al* 2006).

3.5 Mixed Alumel/Al CWAs at Standard Current

Mixed CWAs are CWAs that have wires with multiple wire materials. Experiments were performed with four wires of Alumel (10 μm thick) and two wires of Al 5056 (17.8 μm thick) along a diameter. This configuration was expected to provide nonuniformity in the precursor column formation while still maintaining a level of symmetry throughout the pinching process. Other than the different wire materials, the other parameters for the experiments were kept the same (12 mm diameter, 6 wires, and standard current). The linear mass of the load was 42 $\mu\text{g/cm}$. The time gated diagnostics were again set to record the precursor phase.

Figure 3.9a displays the PCD and current signals, and timings for the time gated pinhole images and spectra. The PCD signal measured an initial rise starting around 60 ns prior to the first peak from the main x-ray burst. The signal from the precursor column exhibited an intense rise

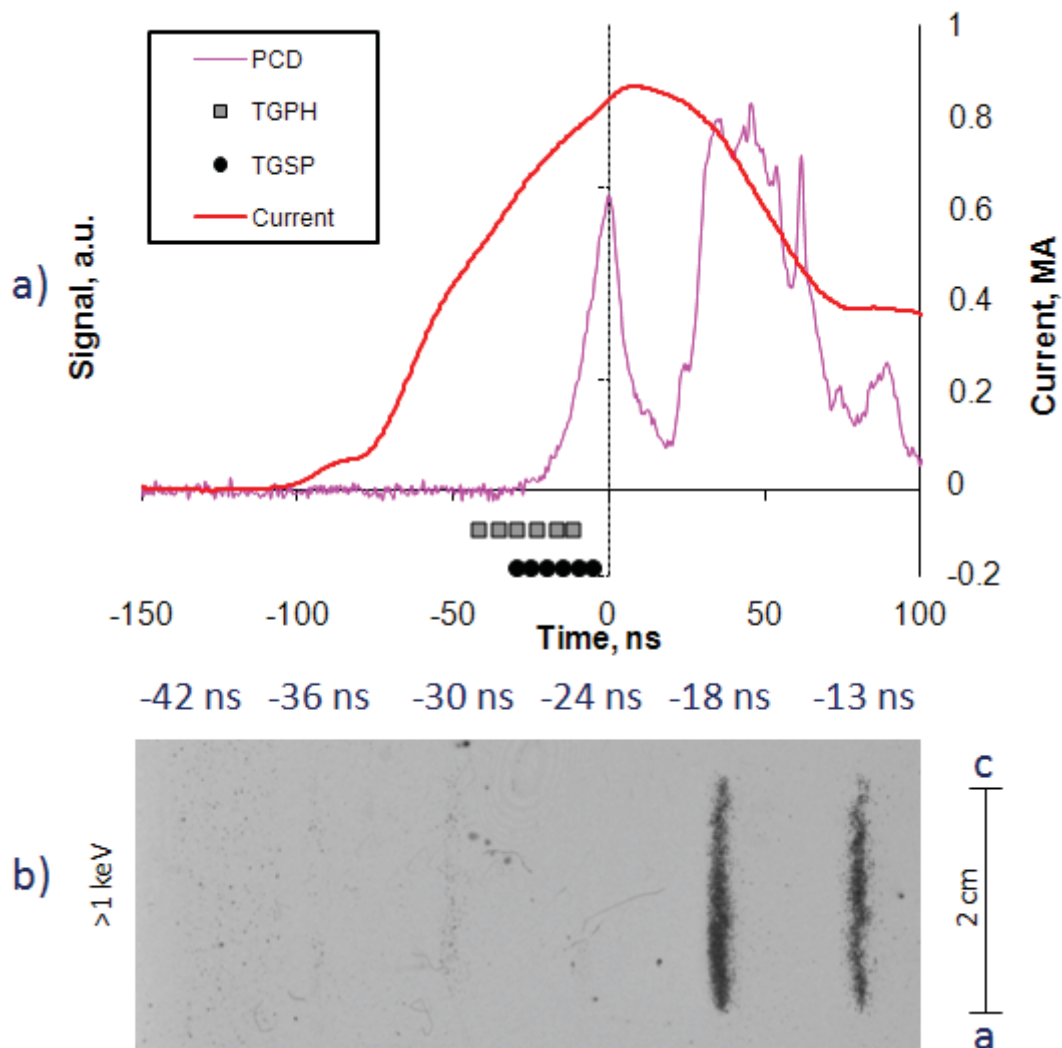


Figure 3.9. a) Signals for 1 MA Alu mel/Al CWA including: current, PCD, x-ray time gated pinhole images (TGPH), and x-ray time gated spectra (TGSP). b) X-ray time gated pinhole images for energies $>1\text{keV}$. Times are relative to the precursor PCD peak. Anode to cathode gap is 1 cm.

and fall that peaked at about 75% of the intensity of the maximum signal at the origin. The signal bottomed out at 17 ns before sharply rising due to the beginning of the main implosion that first peaked at 35 ns. The time gated pinhole images and spectra were able to record the beginning of the rise in the PCD signal. The pinhole images record until the middle of the PCD rise while the spectra last until near the peak of the precursor radiation peak. Figure 3.9b shows the x-ray pinhole images recorded with the timings relative to the first peak of the main x-ray burst. The

frame at -18 ns captured was the first with a strong column of radiation with a diameter between 1.5 and 1.7 mm. The column appeared mostly smooth with the thicker part of the column on the anode side. The following frame at -13 ns showed a column with decreased intensity compared to the previous frame.

Figure 3.10 displays the film that recorded the x-ray time gated spectra with four lineouts from the frames with the most radiation. Three different models were used to analyze the spectra: K-shell Al, K-shell Mg, and L-shell Ni. The K-shell Al lines began optically thin at -20 ns, but then shifted to optically thick in the following frames and therefore K-shell Mg was primarily used to understand the influence of the Al wires. Neither the K-shell Al nor Mg produced the Ly α line and therefore the T_e of the plasma was only able to be determined to be less than 300 eV. A possible reason the Al and Mg radiation was colder than in the Al CWA was likely due to the initial plasma arriving on the axis without the additional pressure from the other four wires which reduces the plasma confinement and therefore the buildup of the hotter temperatures. The N_e was much more reliably determined due to the strong He α and intercombination (I.C.) lines. The N_e

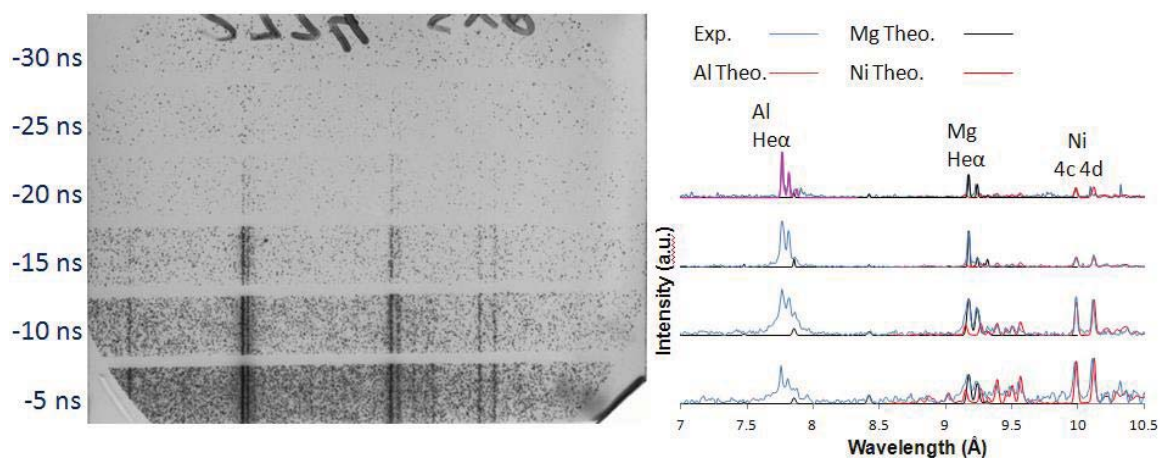


Figure 3.10. X-ray time gated spectra for Al/Mg/Al CWA. Times for spectra are relative to the precursor PCD peak. Spectra from precursor radiation are shown compared to modeling from K-shell Al and Mg and L-shell Ni non-LTE kinetic models.

estimated using the K-shell Mg started at $3 \times 10^{19} \text{ cm}^{-3}$, rose to $2 \times 10^{20} \text{ cm}^{-3}$ in the following frame, then dramatically dropped to $1 \times 10^{18} \text{ cm}^{-3}$, and finally reached $1 \times 10^{17} \text{ cm}^{-3}$. The first rise in the N_e was likely due to the arrival of the Ni plasma which provided a more uniform pressure of the precursor column. The following N_e drop was likely an underestimation due to the increased presence of L-shell Ni radiation in a similar location to the Mg He α and I.C. lines. The modeling of the K-shell Mg matched the peaks associated with the He α and I.C. lines assuming no L-shell Ni influence. The L-shell Ni lines near the Mg He α and I.C. lines had a similar magnitude which would evenly raise the Mg lines and lead to a lower density estimation.

The L-shell Ni radiation was barely present in the -20 ns frame and it grew stronger throughout the remaining frames. At -5 ns the 4C and 4D Ni lines were comparable in intensity to the Mg and Al He α lines. Due to the limited spectral range viewable in the x-ray time gated spectra, the best N_e diagnostic lines were not available. This significantly reduced the accuracy of N_e estimations for the L-shell Ni radiation. A constant N_e of $5 \times 10^{19} \text{ cm}^{-3}$ was used for all the L-shell Ni modeling as it was similar to the densities estimated for the K-shell Mg before the L-shell Ni became prominent and it was also similar to the N_e measured in the previous AluMel CWA experiment. The T_e estimations for the L-shell Ni were fairly consistent starting at 350 eV (20 ns prior to the precursor peak). It was the same at -15 ns, but dropped to 340 eV at -10 ns and lastly rose to 370 eV at -5 ns. These were similar to the T_e measured during the AluMel CWA experiment.

Another method was used to examine the processes occurring in the formation of the precursor column. The spectral range detected by the x-ray time gated spectrometer was divided into four regions shown in Figure 3.11. The region between 6.5 and 8 Å, labeled 1a, was dominated by K-shell Al and the region between 8 and 9.28 Å, labeled 1b, was dominated by K-shell Mg. These two regions combined were labeled 1t and consist of most of the K-shell

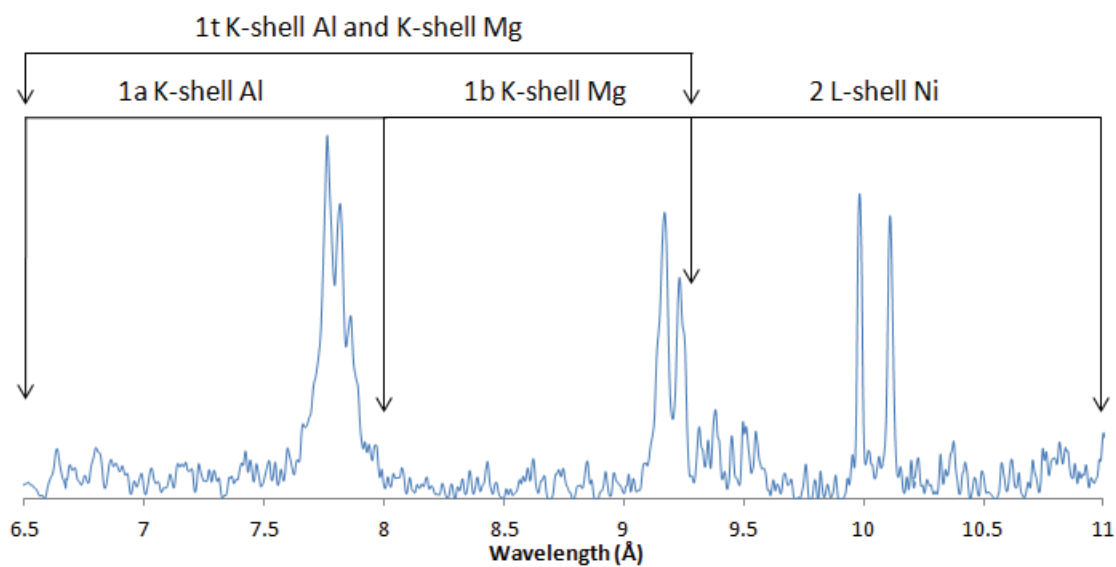


Figure 3.11. The spectral region viewable by the x-ray time gated spectrometer divided into four regions: 1t) K-shell Al and Mg from 6.5 to 9.28 Å, 1a) K-shell Al from 6.5 to 8 Å, 1b) K-shell Mg from 8 to 9.28 Å, and 2) L-shell Ni from 9.28 to 11 Å.

radiation, while the last region was between 9.28 and 11 Å, labeled 2, and was mostly dominated by L-shell Ni radiation. Each of these regions was analyzed by integrating the intensity in the region. The integrals of regions 1t, 1a, and 1b were divided by the integral of region 2 to create a ratio that when plotted versus the timing of the frame create a picture of how the radiation changes through the precursor column formation.

Figure 3.12 displays how the calculated ratios evolved. Each of the ratios followed the same trend of a large increase between the first and second frames followed by two frames of steady decline. The initial increase was due to the faster ablation of the Al 5056 wires creating radiation before the Ni reached the axis to begin radiating. The following frames show the L-shell Ni was reaching the axis and beginning its radiation. The timing of the last frame occurred shortly before the peak in the PCD signal so it is expected that the L-shell Ni was growing during this period. The L-shell Ni was expected to be a bigger contributor to the total radiation as it had roughly double the total mass of the array and L-shell radiation had more transitions to provide

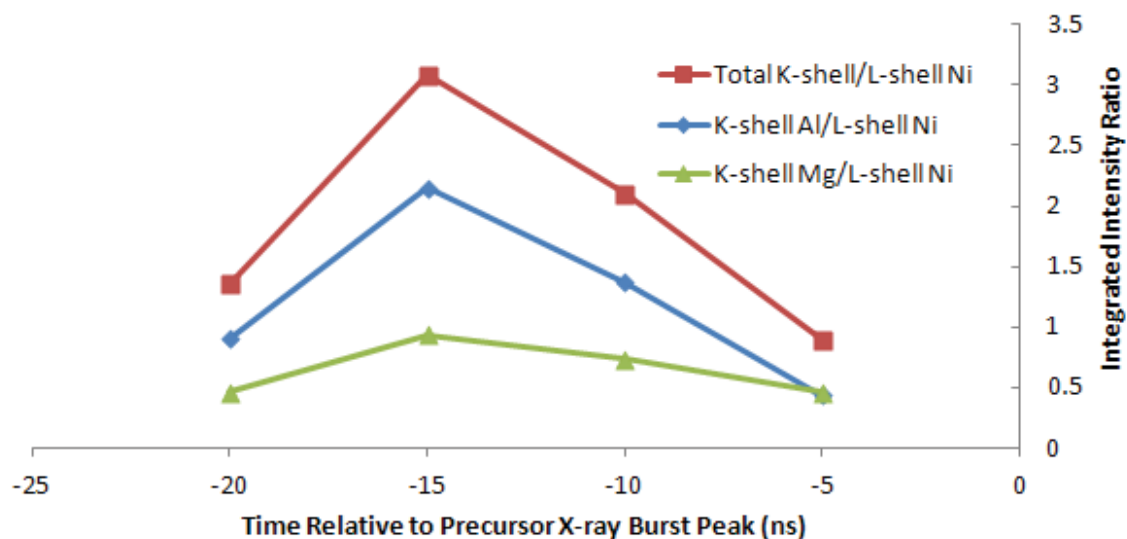


Figure 3.12. The ratios of the integrations of the regions from Figure 3.11 plotted versus the time relative to the first PCD peak which is attributed to the precursor plasma.

more radiation through numbers even with the most intense L-shell Ni transitions existing outside the viewable spectra region.

3.6 Conclusions

The motivation for studying the precursor columns from CWAs was to prove that the high electron temperatures for Ni-60 CWAs measured in Coverdale *et al* 2009 were not unique for mid-Z loads in particular. The expanded research with the Cu and Alumel CWAs found similar >300 eV electron temperatures which suggests such values are common for mid-Z loads. Upon finishing the initial goals of precursor column research, another opportunity was available with the addition of the Load Current Multiplier (LCM). Current scaling effects on precursor columns are difficult to measure as Z-pinch machines are uncommon and are largely divided into university scale (~ 1 MA) and national lab scale (>20 MA). With the LCM, an additional current region can be used to further understand the differences. The experiments done using Ni-60 wires with 1.5 MA currents created thicker precursor columns on average (1.5 mm) than the 1 MA

current experiments (1-1.5 mm). The radiated energy from the precursor column in the PCD range (>750 eV) was approximately 200% more for the enhanced current experiments (40 J/cm to 14 J/cm). Modeling of the x-ray time gated spectra suggests similar electron temperatures for the different currents. However, the electron densities varied from 1×10^{19} to 9×10^{19} cm^{-3} for the enhanced current experiments while the standard current experiments were consistently $\sim 1 \times 10^{19}$ cm^{-3} . Comparing the plasma conditions from each set of experiments suggest the increased current created a typically larger precursor column with nearly similar electron temperatures and higher electron densities leading to more radiation from the precursor plasma.

After obtaining the current scaling results, interest shifted to studying mixed material CWAs. Alumel was chosen due to it being the best precursor phase radiator of the mid-Z materials and aluminum was chosen due to its significantly different ablation rate. Al CWA experiments were performed to determine a baseline for comparison. While analyzing the Al CWA precursor column results it was found that the precursor radiated fairly uniformly from its beginning until the beginning of the main implosion unlike the mid-Z materials that exhibited a rise and fall prior to the main implosion. It was also found that the K-shell radiation from the precursor column was much hotter (270 – 310 eV) than the 50 – 60 eV estimations from the EUV spectra collected by Bott *et al* 2006, but somewhat cooler than from mid-Z loads. The mixed material CWA experiments were performed with two Al wires along a diagonal. The PCD signal detected a precursor phase rise and fall similar to the Alumel CWA. X-ray time gated pinhole images showed the precursor column was similar in size to the Alumel precursor column. The x-ray time gated spectra provided the most interesting results. The spectra captured the evolution of the K-shell Al and Mg and L-shell Ni radiation during the precursor column formation. K-shell Al and Mg radiated first before the L-shell Ni grew stronger leading into the peak of the precursor column radiation. Comparing the integrated spectra from each of the elements highlighted the evolution of the radiation. Modeling of the x-ray time gated spectra determined the K-shell Al

and Mg were colder than seen in the uniform Al CWA. Modeling of the L-shell Ni suggested similar plasma conditions seen in the uniform Al₂O₃ CWA.

The next steps in the CWA precursor column studies would be furthering the understanding of the mixed CWA precursor columns. The first step would be additional experiments with the same configuration, but with different timings for the time gated diagnostics. The current timing captured the early formation very well. However, the precursor radiation phase was much longer than currently recorded. Shifting the timings to capture the peak of the radiation and the fall of the radiation would fill in more information on the precursor column evolution. After fully investigating the precursor column phase, the second step would be changing the ratio of Al and Al₂O₃ wires. Replacing two Al₂O₃ wires with Al wires would help in understanding the influence of the dominant material in the precursor column formation.

Chapter 4

Spectroscopic Analysis of Ti Alloy X-pinch Experiments at 1.5-1.7 MA

4.1 Introduction to X-pinches

An X-pinch is typically formed by crossing 2 or four thin wires that are crossed in an X pattern as seen in Figure 4.1. The wires are then subjected to a large current which causes the wires to ionize into plasma in a process called ablation. The difference between an X-pinch explosion/implosion and a CWA implosion is the current is funneled to the center of an X-pinch. The cross point rapidly ionizes due to the focused current which creates a bright spot in the middle. While the CWA experiments are driven by an implosion process the X-pinch is driven by a series of explosions and implosions as the mass starts in the cross point. The current causes an

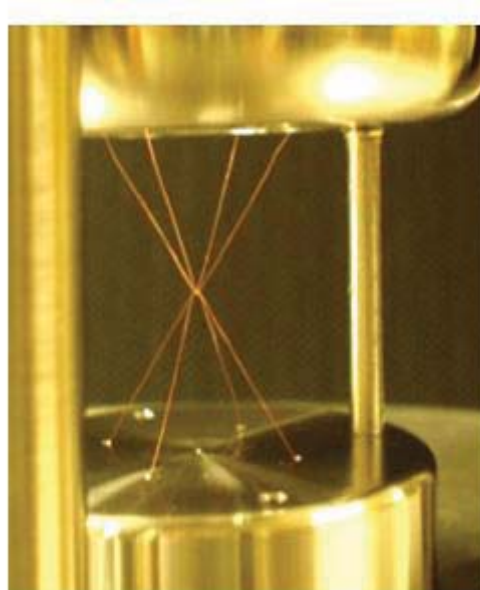


Figure 4.1. Picture of an X-pinch.

explosion of the central mass that will be pulled back into the center due to the $J \times B$ Lorentz force. This will repeat multiple times before it eventually dissipates. The X-pinch primarily radiates x-rays from the well-localized bright spot in the center unlike the CWAs. A common feature of X-pinches is that they create plasma jets that eject from the center (Beg 2006). These jets are created from the pressure created from the gradient in the magnetic fields along the central axis of the wires. This gradient is created by the crossed wires which remove the central axis uniformity that is seen in the CWAs. In addition, jets can be found perpendicular to the X-pinch wires.

X-pinches have been of interest in many fields due to their high intensity, short x-ray bursts and their mostly point like source nature. X-pinches have been used as an x-ray backlighting source (Pikuz 1997 and Shelkovenko 2001), for understanding jet formation which is useful in astrophysics (A.S. Safronova 2009a), and as a high energy density plasma source (A.S. Safronova 2006 and Shelkovenko 2002).

4.2 Ti-Alloy X-pinches at Enhanced Current

There have been significant studies involved in understanding K-shell radiation. An important part of understanding K-shell radiation is knowing what is necessary to achieve K-shell radiation for a given element. There have been many Z-pinch experiments performed by the Naval Research Laboratory investigating the necessary electron temperatures to produce significant K-shell radiation for a given material (Whitney 1990 and Thornhill 2006). A relationship was found as described in Equation 4.1:

$$T_e = 0.3 * Z^{2.9} eV \quad 4.1$$

Z is the atomic number of the material and T_e is the electron temperature in electron volts. This scaling law was confirmed to be accurate with high currents for a variety of materials up to Cu by

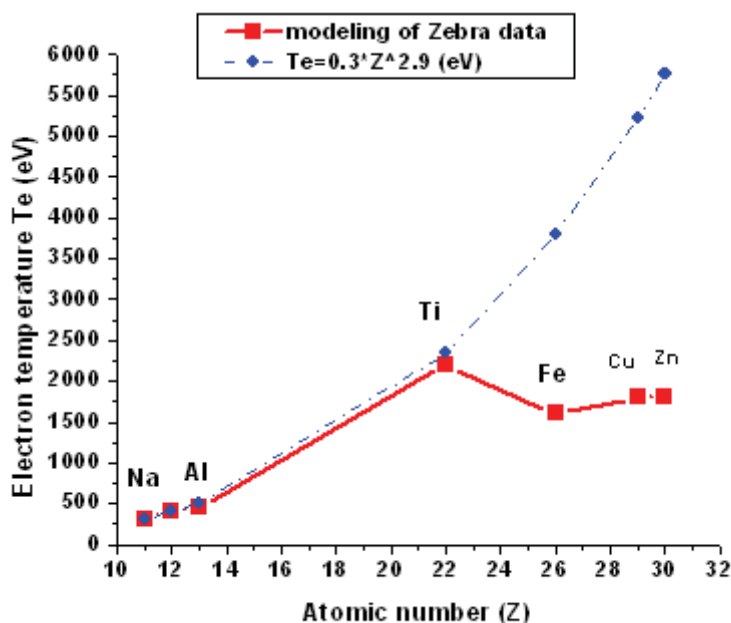


Figure 4.2. Plot of electron temperatures estimated from K-shell radiation of plasmas created with the 1 MA Zebra generator and the theoretical curve that determines the necessary temperature to produce significant K-shell radiation for a given atomic number. Figure borrowed from proceedings of Dense Z-pinches 2011 unpublished.

use of the Z generator at Sandia National Laboratories (Coverdale 2010). Experiments were also performed using the 1 MA Zebra generator at the University of Nevada, Reno showing a good agreement as seen in Figure 4.2. (A.S. Safronova 2012a). The limits of the Zebra generator can be seen however as the experiments begin to substantially deviate from the theoretical curve around $Z=26$. Ti was found to produce the highest electron temperatures with the standard current and was chosen as the starting point to begin testing the limits of the Zebra machine equipped with the LCM.

X-pinch experiments using four Ti or Ti-alloy (90% Ti, 6% Al, and 4% V) wires were performed using the LCM. Table 4.1 lists the Ti X-pinch experiments performed on the Zebra Generator using the LCM with the wire material, load mass, and total energy measured by the bolometer. Much thicker (compared to CWAs) wires with 50-127 μm diameters were used creating a 133-2300 $\mu\text{g}/\text{cm}$ linear mass. Shot 3115 used 50 μm wires and was found to be far too

Table 4.1. Table of X-pinch experiments using Ti based wires. Load mass and total energy measured for the experiments are included.

Shot Number	Wire Material	Load Mass $\mu\text{g}/\text{cm}$	Energy kJ
3115	Ti	133	10.4
3116	90% Ti, 6% Al, 4% V	1455	19.0
3118	90% Ti, 6% Al, 4% V	1455	13.5
3585	Ti	2300	15.3
3586	Ti	2300	12.2

light for optimal use with the LCM. Subsequent loads were made with much thicker wires, 100 or 127 μm . The total radiation yield measured by the bolometer was $15 \text{ kJ} \pm 20\%$. Typical energies for the 1 MA X-pinch were 10 kJ/cm when normalized to the anode to cathode gap.

Figure 4.3a is the current, diode signals, and timings for the time gated diagnostics for the experiment with the highest radiation yield, Shot 3116. The XRD signal represents energies $>0.2 \text{ keV}$, the PCD signal represents energies $>0.75 \text{ keV}$, and the SiD signal represents much higher energies $>9 \text{ keV}$. Each of these signals measured a series of peaks that begin roughly 53 ns after the start of the current rise that continue for the next 50 ns when the signals begin to fade away. Timings for the x-ray time gated spatially integrated (TGSI) spectrometer are shown by the black dots and the grey squares represent the timings for the time gated pinhole cameras.

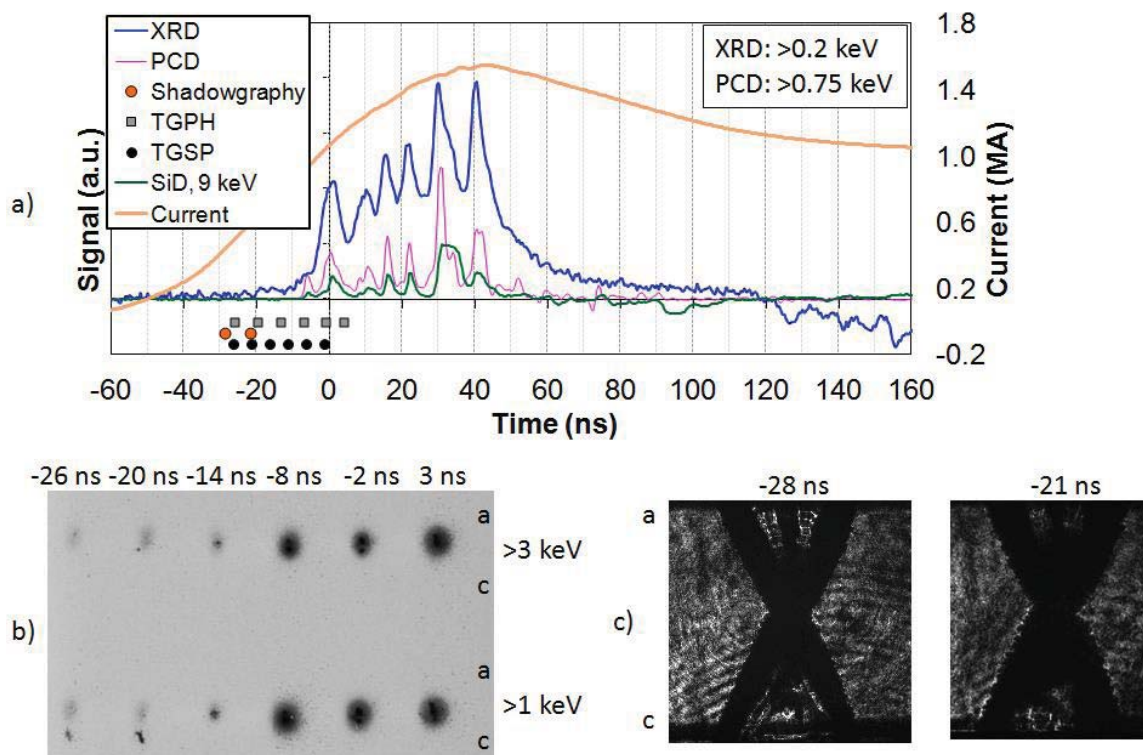


Figure 4.3. a) Current and diode signals, and timings for time gated diagnostics measured from a Ti alloy X-pinch experiment. b) X-ray time gated pinhole images with cutoff energies >3 and >1 keV labeled with timings. c) Shadowgraphy images recorded with timings. All timings are relative to the first peak in the XRD signal.

4.2.1 Time Gated Spectral and Imagery Data Analysis

The timings for the time gated spatially resolved (TGSR) pinhole images are displayed with the gray boxes in Figure 4.3a. These images are shown in Figure 4.3b with their timings relative to the first peak in the XRD signal. The images are filtered into >3 keV on top and >1 keV on the bottom. The >3 keV image represents the K-shell Ti radiation and the difference between the >3 keV and >1 keV images represents the K-shell Al radiation. The first frame shows faint spots in the center of the X-pinch for both the >3 keV and >1 keV images. The >1 keV image has an additional intense spot closer to the cathode. As this does not appear in the >3 keV images, the expected composition of the radiating mass on the cathode side of the cross point is Al. In the following frame the center spot remains faint for both images while the cathode spot

grows larger in the >1 keV image. The third frame shows the cathode spot disappears in the >1 keV image while the center spots for both images get more intense with a slightly larger bright center in the >1 keV image. The fourth frame begins a significant change in the pinhole images. This is at -8 ns which matches up with the first peak in the PCD and SiD signal. The pinhole images grow much larger and more intense with the >1 keV image being a little larger than the >3 keV image. The next frame indicates a small decrease in size of the radiation spots for both images, but multiple bright spots can be observed in the center of the radiation. The fifth frame coincides with the second peak in the PCD and SiD signals and the first peak XRD signal. In the last frame the spots grow a little larger and the bright spots have combined into a larger spot. The signals at this time are at the low points between peaks.

The timings for the shadowgraphy images are represented by the two orange dots at -28 and -21 ns in Figure 4.3a and correlate in time with the first frame of the X-ray pinhole image. These images are displayed in Figure 4.3c. The shadowgraphy image at -28 ns shows the ablating wires that make up the x pattern with a plasma jet from the center up to the anode while between the center and cathode there is some less uniform structure occurring. When compared with the first time gated x-ray pinhole image the structure between the center and the cathode matches the more intense region seen in the pinhole image. The shadowgraphy image at -21 ns shows a similar structure as the image at -28 ns. The wires have expanded further and though there is more blockage of the laser, the structure between the center and the cathode is still there. Again this matches with the intense radiation spot seen in the second pinhole image.

Figure 4.4 displays time gated pinhole images for Shot 3585, a pure Ti wire X-pinch, for comparison with the Ti alloy X-pinch. The timings for the pinhole images are labeled with respect to the main peak in the XRD signal. The images for the >3 keV filtering remain mostly constant for the recorded time of -44 to -14 ns. The >1 keV images start with a very similar

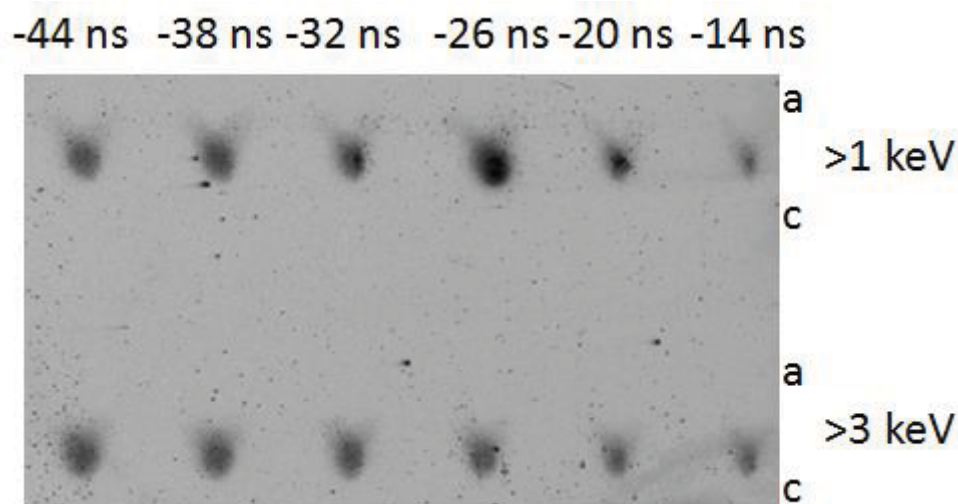


Figure 4.4. Time gated pinhole images from shot 3585. Timings are with respect to the main peak in the XRD signal.

appearance to the >3 keV images. However, at -32 ns the >1 keV image sees the start of a bright spot that grows more intense at -26 ns, before dropping at -20 ns. Finally, at -14 ns both images appear to be the same again. When compared to the Ti alloy X-pinch pinhole images, both show radiation from the cross point, however, the bright spot between the cathode and the cross point in the Ti alloy X-pinch images is not in the pure Ti X-pinch images. This might suggest the Al in the Ti alloy experiment is undergoing a unique process, though it is just as reasonable to assume the materials available in the pure Ti experiments are unable to be energized to the point of radiating in the >1 keV regime under the same conditions. This is because K-shell Ti is much more difficult to achieve than K-shell Al and L-shell Ti does not radiate at >1 keV energies.

The TGSX X-ray spectra with their timings relative to the current start are displayed in Figure 4.5. The last two frames are repeated on the bottom with adjustments to make the lines more visible. The time gated spectra begin with very little background and three lines on the longer wavelength side. These lines fade over the next two frames before completely disappearing in the fourth frame. The last two frames show a complete transition into intense background radiation and three lines on the shorter wavelength side. The timing of the fifth frame

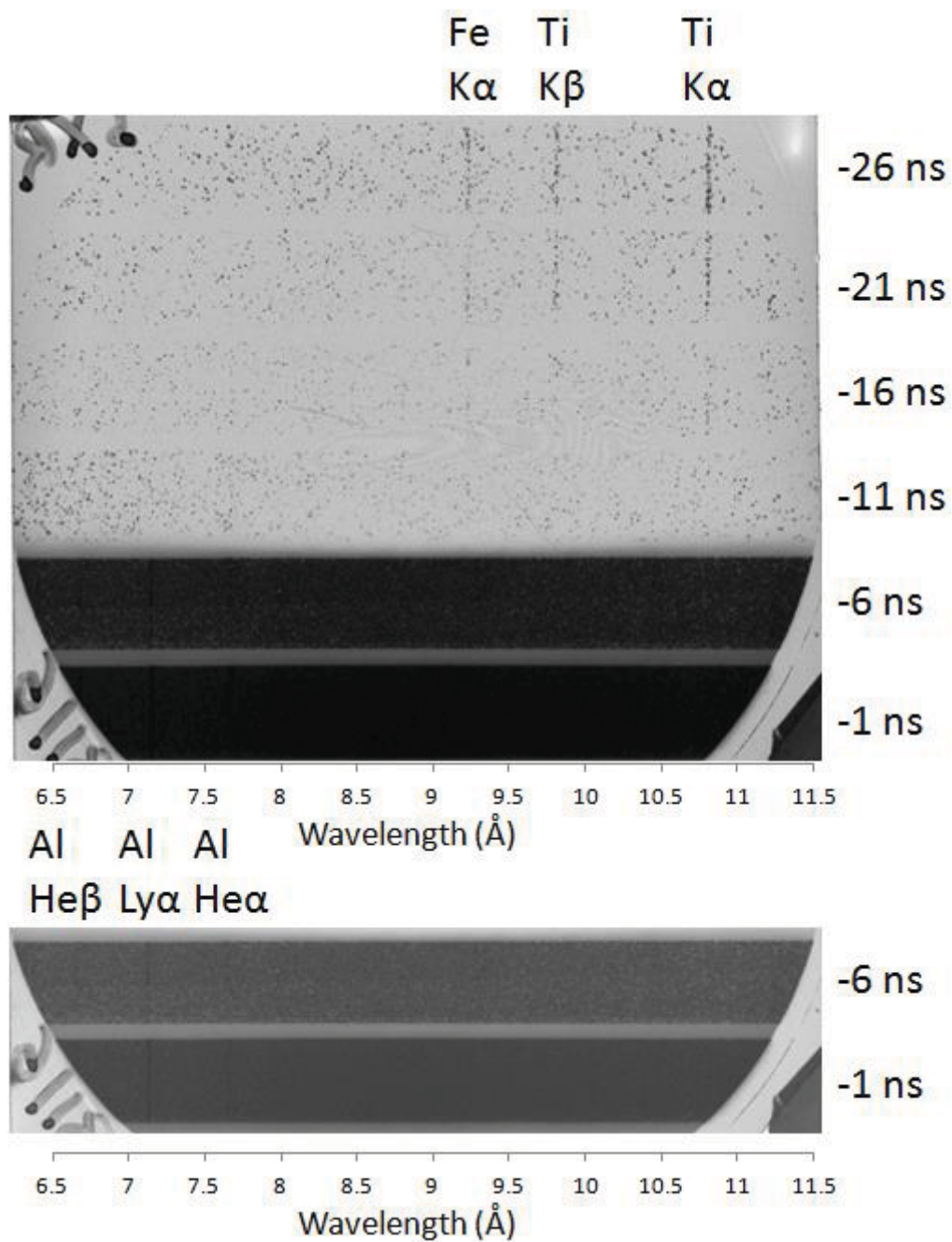


Figure 4.5. Time gated spectra recorded during Ti alloy X-pinch experiment with timings relative to the first peak in the XRD signal. The fifth and sixth frames are repeated with contrast adjustments for better viewing of K-shell Al lines. An approximate wavelength scale is included.

is at -6 ns which is approximately when the first PCD and SiD signal peaks occur. The three lines from the first frames occur before the signals from the various diodes begin rising coupled with the small amount of background radiation suggests the lines are cold characteristic lines.

The singular nature of the lines suggests K-shell emission and the elements available from the wires include Ti, and of much smaller concentration Al. The dominant element is Ti so that is the first expectation to identify the lines. Ti $K\alpha$ emission from neutral Ti has a wavelength of 2.7486 Å. The spectral range of the spectrometer is approximately 6.5 – 11.5 Å. The characteristic lines would have to be from a higher order reflection. The third order Ti $K\alpha$ emission would be ~ 8.2 Å and the fourth order would be ~ 11 Å. 8.2 Å appears to be an unlikely match for any of the lines when compared with the approximate wavelength scale, but 11 Å is a good match for the longest wavelength line. The wavelength for Ti $K\beta$ is 2.514 Å which is ~ 10.05 Å in fourth order. This is a good candidate for the second longest wavelength line. The line with the shortest wavelength of the three was more challenging to identify. Remembering the bright spot near the cathode from the pinhole images could suggest interaction with the hardware of the cathode which is composed of stainless steel. Interaction with the hardware would create cold Fe plasma. The wavelength of neutral Fe $K\alpha$ is 1.936 Å. The fourth order reflection would have a wavelength of ~ 7.74 Å. This is too low for where the line is as shown by the approximate wavelength scale. The fifth order reflection is ~ 9.68 Å which would fit with the location of the line. Additional transitions were tested for matches including hot ionic transitions and other elements; however, the best match came from fourth order cold $K\alpha$ and $K\beta$ Ti and fifth order $K\alpha$ Fe. While these transitions match the lines, the biggest question is why the third order reflections for the Ti transitions and fourth order reflection of the Fe transition was not visible. This is a question that is still under investigation.

The three lines for the last 2 frames are on the shorter wavelength side of the observe spectrum. These three lines are also singular so K-shell radiation is again the expectation. The expectation would have been third order K-shell Ti, however since the previous early frames recorded fourth order reflections without third order reflections it is less certain. The well known K-shell Al He α , Ly α , and He β would also be in this location on the film. In the absence of lines on the longer wavelength side of the film it was determined that the three lines in the last two frames are from Al transitions. The Ly α line is the most intense line suggesting relatively hot temperatures compared to typical Al Z-pinches. Due to the saturation of the film modeling is not reasonable for these spectra.

Unfortunately, due to complications in fielding the spectrometer, the pure Ti X-pinch experiments do not have time gated spectra for comparison. This will be an area of focus for future experiments.

4.2.2 Time Integrated Spectral Data Analysis

A time integrated spatially resolved (TISR) x-ray spectrometer was fielded to record a spectral region of approximately 1-15 Å. The TISR spectra record throughout the entire experiment and with the large spectral range it tends to record most lines that are recorded by the time gated spectrometer. Therefore, they are useful for comparing with time gated spectra to verify the identification of lines. It was expected that third order reflections of K-shell Ti would be the primary feature of the TIRS spectra. Figure 4.6 is a cropped image of the TISR film from one of the Ti alloy X-pinch experiments. The various lines seen on the film are labeled with the final identifications after extensive analysis. The primary features are the very intense K-shell Al and the fourth order K-shell Ti. The Al concentration in the wires was 6% and was therefore not expected to be nearly this noticeable. As previously stated the expectation was that third order

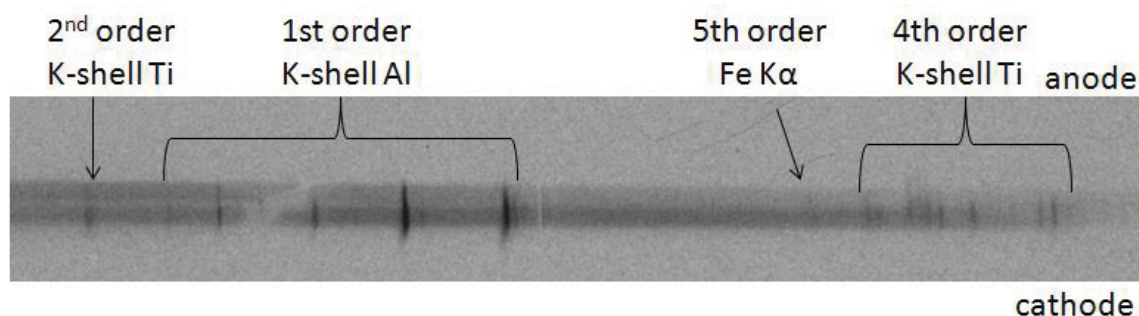


Figure 4.6. A cropped image of the x-ray time integrated and spatially resolved spectra collected from a Ti alloy X-pinch experiment. The different lines are grouped by element and order of reflection.

reflections of K-shell Ti would be dominant in this region and that was the original assumption when attempting to identify the most intense region. One of the early reasons for the confusion was that third order K-shell Ti has very similar wavelengths to first order K-shell Al. Attempting to calibrate the lineout from the TISR spectrum using the third order reflections of K-shell Ti did not produce a smooth correlation that would be expected. Consideration of the time gated spectra suggested K-shell Al could be the solution and calibration under that assumption proved to be a smoother fit. An additional element of confusion was the bright line labeled as second order K-shell Ti in Figure 4.6. This line was too intense to fit as a high Rydberg state K-shell Al transition. It was found that second order Ti He α fit the line location very well.

Figure 4.7 are lineouts from a Ti alloy experiment (red) and a pure Ti experiment (blue). The pure Ti experiment provided additional insight into identification of the lines from the Ti alloy experiment and provided further evidence that the third order reflections for Ti were not appearing with the KAP crystal spectrometers. Looking at the pure Ti lineout shows a clear correlation with many regions from the Ti alloy lineout. The pure Ti lineout has more intense lines at similar points to the Ti alloy lineout which improved the confidence level of the line identification. Additionally, there are no obvious lines between 6 – 9 Å where third order reflections of K-shell Ti would be seen. The lack of third order reflections greatly improves the

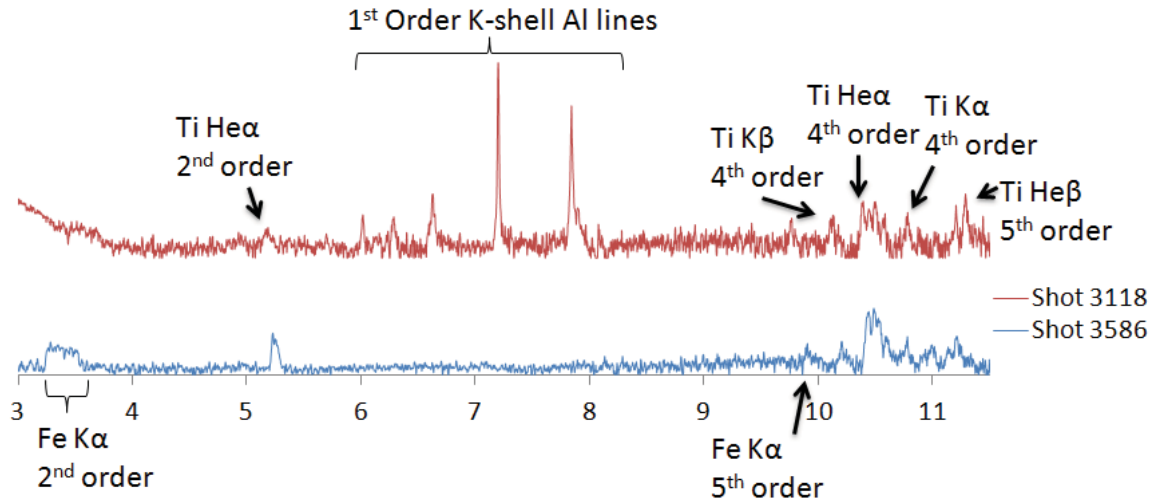


Figure 4.7. Lineouts from TISR spectra from Ti alloy (red) and pure Ti (blue) X-pinch experiments. Important lines are labeled.

confidence in the identification of the lines in the time gated spectra and further verifies the intense K-shell Al is correct.

Figure 4.8 is a lineout focused on the K-shell Al region from the Ti alloy experiment and includes modeling. The model used a $550 \text{ eV } T_e$ and a $5 \times 10^{20} \text{ cm}^{-3} N_e$ that were chosen by matching the model to the lines from high rydberg states. The model was run assuming optically thin plasma. The significant overestimation for the four most intense lines proves that it is a very optically thick plasma. This is a surprising result considering the relatively small concentration of Al in the wire material. The $\text{Ly}\alpha$ line being the most intense highlights the hot electron temperatures for the Al plasma.

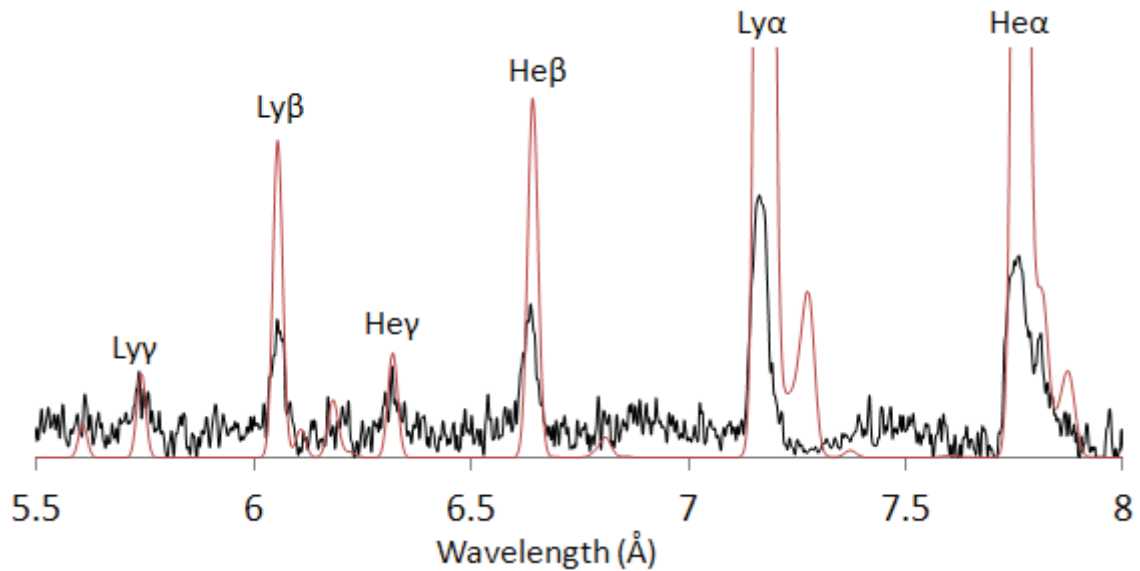


Figure 4.8. A lineout taken from the central hotspot of the x-ray time integrated spatially resolved spectra focused on the K-shell Al radiation (black). Theoretical modeling of the experimental spectra estimated with $T_e = 550$ eV and $N_e = 5 \times 10^{20} \text{ cm}^{-3}$ (red).

After identifying the most intense region, the next step was identifying the diagnostically important lines in the longer wavelength region of the film. It is noticeable that as the background radiation becomes less intense due to the increasing effect from the filters, the lines remain largely consistently intense. Including this with the results from the time gated spectra it was determined the lines were fourth order K-shell Ti reflections with one fifth order Fe $K\alpha$ reflection. The K-shell Ti is most defined by the strong $He\alpha$ line, and the $K\beta$ and $K\alpha$ lines. The $He\alpha$ line suggests temperatures >1000 eV (A.S. Safronova 2008). There are the two peaks on the long wavelength side of the fourth order region that are fifth order $He\beta$ lines and there is another prominent fourth order $K\alpha$ line in between the two lines and the cluster with the $He\alpha$ transition. The $He\alpha$ cluster would like come from the hottest region that would be the center of the X-pinch while the $K\alpha$ lines would come from cooler plasma that surrounds the center or is closer to the anode or cathode.

4.3 Conclusions

Pure Ti and Ti alloy X-pinch experiments were performed using the LCM to test the X-pinch at the enhanced current. This was motivated by Ti X-pinch providing the hottest electron temperatures on the Zebra Generator under standard current conditions (A.S. Safronova 2012a). Ti X-pinch, pure and alloyed, as heavy as $2300 \mu\text{g}/\text{cm}$ were exploded with a very high radiation yield up to 19 kJ cm . The time gated spectra recorded the transition from early cold $K\alpha$ emission from Ti and Fe to the hot ionic emission from K-shell Al that begins with the start of the x-ray bursts in the Ti alloy experiments. The Fe $K\alpha$ would have to come from interactions with the anode or cathode hardware. The time gated pinhole images and the shadowgraphy images showed unique structure between the center of the X-pinch and the cathode which is likely where the Fe $K\alpha$ is originating.

The TISR spectra from the Ti alloy experiments recorded very intense and optically thick K-shell Al radiation as well as fourth order K-shell Ti and fifth order Fe $K\alpha$ reflections. The K-shell Al was estimated with a T_e of 550 eV and a N_e of $5 \times 10^{20} \text{ cm}^{-3}$. The fourth order K-shell Ti included an intense Ti $\text{He}\alpha$ line that suggests a minimum T_e of 1000 eV . The K-shell Ti also include multiple $K\alpha$ lines that were not all clustered suggesting three or more plasma regions with different conditions were radiating.

Continuing with this research would require more experiments with pure Ti wires with a focus on recording first order K-shell Ti and time gated spectra. An additional time integrated spectrometer with a spectral range focusing on first order K-shell would improve estimations of the plasma conditions achievable with the LCM. Further research into the evolution of the X-pinch experiments by varying the times of the time gated diagnostics would improve the understanding of the differences of the implosions and explosions in comparison to the X-pinch

at standard current. The last step is to perform experiments with slightly higher atomic number elements to determine if using the LCM can achieve significant K-shell radiation from heavier materials.

Chapter 5

Application of Dielectronic Recombination to Understand Satellite Structures from Laser Irradiated Mg Targets

5.1 Introduction to Dielectronic Recombination

Dielectronic recombination is an important process in atomic physics. The process includes the capturing of a free electron by an ionized atom to create a doubly excited atom of a lower ionization level. This process leads to radiative emission of satellite lines. This is seen in many plasma related fields including astrophysics, laser plasma physics, and Z-pinch physics.

Atomic energy states of unusual states ($2nl'$ and $1s2nl'$) were introduced for the first time by Edlen *et al* in 1939. They interpreted them as due to the parent transition, in the presence of an additional outer electron. Thus designating the additional electron as nl' satellites to the principle resonance lines would arise from $1snl' - 2pnl'$ and $1s2nl' - 1s2pnl'$. Long wave satellites to the He-like ion resonance lines in the laboratory and in the Sun were classified by Gabriel *et al* 1969 by comparing computed spectra with observation, over the range C IV to Al XI. They also proposed that the dominant mechanism for production of the autoionizing $1s2pnl'$ states was by dielectronic recombination.

Theoretical studies on satellite structures of K-shell transitions have become extremely detailed since they were first introduced. Many satellites to the Ly α transition were calculated for He-like transitions (Vainshtein *et al* 1980, Kato *et al* 2001, and Yamamoto *et al* 2005). The wavelengths, radiative transition probabilities, autoionization rates, and relative intensity factor have been calculated for $1snl' - 2nl'$ transitions with $n = 2, 3$ and 4 providing the necessary tools

to analyze experimental spectra. Mg He-like transitions were calculated using the quasi-relativistic many-body perturbation theory (MZ) code by Vainshtein *et al* 1980. The MZ code coordinates the calculation of energy levels and radiative and autoionization rates. Many-body perturbation theory (MBPT) was used to represent each of those properties as a function of $1/Z$ (Z is the nuclear charge). Kato *et al* 2001 used a Collision Radiative Model (CRM) to calculate He like Mg transitions. Li-like transitions have also been heavily studied as satellites to the He β transition (Peacock *et al* 1973, Steenman-Clark *et al* 1980, Chen 1986, U.I. Safronova *et al* 1995, U.I. Safronova *et al* 2004, and Deng *et al* 2012). These satellites take the form of $1s3lnl'-1s^2nl$ for $n = 2, 3$ and 4 and have been described to high accuracy. Li-like Mg transitions have been calculated with various methods and codes including the multi-configuration Dirac-Fock method (MCDF) (Chen 1986 and Deng *et al* 2012) and the SUPERSTRUCTURE program (Steenman-Clark *et al* 1980).

Laser produced plasmas have been shown to be excellent sources for satellite structure studies for more than four decades (Boiko *et al* 1978, Rosmej *et al* 1998, Faenov *et al* 1999, Rosmej *et al* 2000, Rosmej *et al* 2001, Skobelev *et al* 2002, and Colgan *et al* 2008). The high electron densities provide conditions for typically insignificant satellite lines to be prominent enough for detailed examination. These lines are not very affected by opacity and therefore provide opportunities to diagnose plasma conditions that typically require complicated opacity calculations. Many experiments have been performed to look into satellite structures in K-shell radiation. He-like Mg satellites to the Ly α resonance line have been experimentally studied (Boiko *et al* 1977, Aglizki *et al* 1978, and Yamamoto *et al* 2005). Yamamoto *et al* 2005 used a 15 ns pulse duration laser with a pulse energy of 17 J to study He-like satellites. Spectral analysis of experiments from this laser showed satellites from transitions of the form $1snl - 2lnl'$ ($n=2,3,4,5$).

Li-like dielectronic satellites $1s2l3l'-1s^23l$ and $1s3lnl'-1s^2nl$ ($n=3,4$) were matched to spectra from laser produced plasmas (Boiko *et al* 1978, Rosmej *et al* 1998, Rosmej *et al* 2000, Rosmej *et al* 2001, and Skobelev *et al* 2002). These Li-like transitions are satellites to the He β resonance line. Li-like Mg has been studied using many laser conditions. Skobelev *et al* 2002 used two different lasers with 12 ns pulse durations on Mg targets. The first had a pulse energy of 1 J and spectra recorded from these experiments showed Li-like transitions of the forms $1s2l3l'-1s^23l$ and $1s3l3l'-1s^23l$. The second laser had a pulse energy of 20 J and spectra recorded from these experiments had the transitions seen with the previous laser experiments and additionally the $1s3l4l'-1s^24l$ transitions were noticeable. Laser experiments with fs pulses were performed by Rosmej *et al* 2000. The 400 fs pulse duration had an energy of 1 J and was used on Mg targets. Spectra recorded from these experiments showed Li-like transitions of the form $1s2l3l'-1s^23l$ and $1s3l3l'-1s^23l$.

5.2 Description of Mg Target Experiments and Spectrometers

The experiments were performed at the Leopard laser facility at NTF/UNR. The Leopard laser is a hybrid 1.057 μm Ti:Sapphire/Nd:glass laser system suitable to generate 15 J sub-picosecond pulses, with high spatial and temporal beam quality. A detailed description can be found in Wiewior *et al* 2010. Experiments were performed on a wide selection of materials (A.S. Safronova *et al* 2012b). Table 5.1 summarizes the laser parameters for the Mg experiments performed. The laser parameters include pulse length duration (350 fs or 0.8 ns), prepulse to main pulse contrast ratio (10^{-7} , high contrast or 10^{-5} , low contrast), and energy of the laser pulse. The contrast ratio is a comparison of the intensities of prepulses to the intensity of the main pulse from the laser. Prepulses can create plasma prior to the arrival of the main pulse and thus minimizing the prepulse intensity is typically desired. The laser pulse was focused to a 10 μm spot. The Mg targets were flat with a thickness of 50 μm .

Table 5.1. Shot details for Leopard Laser Experiments. All shots had a target thickness of 50 μm .

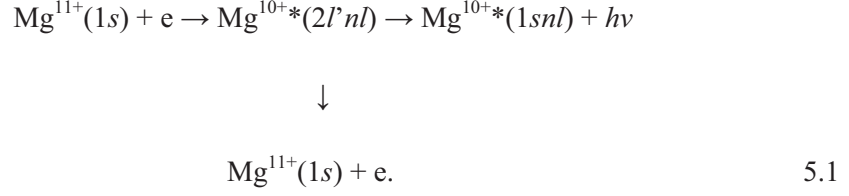
Leopard Shot	Laser Pulse Duration	Contrast	Energy (J)
527	350 fs	10^{-7}	14.4
533	350 fs	10^{-7}	13
534	350 fs	10^{-7}	15
548	350 fs	10^{-5}	13.8
550	0.8 ns	10^{-5}	15.8

Two different spectrometers were fielded to record x-ray spectra. The first spectrometer was a convex spectrometer with a potassium hydrogen phthalate (KAP) crystal. This spectrometer has a spectral resolution of about 300 and has been employed before in Z-pinch experiments (Kantsyrev *et al* 2006 and A.S. Safronova *et al* 2009b). This survey spectrometer covered a broad spectral range from 7 to 17.5 \AA . The second spectrometer was a focusing spectrometer with spatial resolution (FSSR) (Faenov *et al* 1994 and Skobelev *et al* 1995) based on the spherically bent mica crystal ($2d = 19.91 \text{\AA}$). The FSSR spectrometer provides much better resolution of ~ 3000 . The high resolution of the FSSR spectrometer resolves additional spectral features that cannot be resolved by the first survey spectrometer. The high resolution is limited to a narrow spectral range between 14.5 and 17.5 \AA in the first order of mica crystal reflection. In order to use the mica crystal for K-shell Mg, the 2nd reflection order was measured giving a spectral range 7.25-8.75 \AA . This includes the $\text{He}\gamma$, $\text{He}\beta$, and $\text{Ly}\alpha$ resonance lines.

5.3 Dielectronic Satellite Spectra for He-Like Mg

The dielectronic recombination (DR) process entails the capturing of a free electron by an ionized atom which lowers the ionization level of the atom and puts it into an autoionizing state. In studying He-like Mg radiation, this involves a H-like Mg ion capturing a free electron to

become a He-like ion. From the autoionizing level, the He-like Mg ion can either emit a photon through radiative decay or release the electron to return to the initial H-like state as shown:



The ground level of Mg^{11+} , $1s$, is the initial level. The $2l'nl$ levels are the He-like autoionizing levels that will emit a photon or electron to complete the cycle. During the DR process, a dielectronic satellite photon, $h\nu$, is emitted when the electron transitions from a doubly excited autoionizing state, $2l'nl$, to a singly excited bound state, $1snl$. These radiative transitions give rise to satellite lines to the $2p - 1s$ ($\text{Ly}\alpha$) transitions in H-like Mg.

The most important intensity relevant characteristics of satellites are branching ratios $K(i, i_0)$ and relative intensity factors Q_d of the dielectronic satellite (DS) lines. (Vainshtein *et al* 1978)

$$K(j, i) = \frac{A_r(j, i)}{\sum_{i'_0} A_a(i, i'_0) + \sum_j A_r(i, j)} \quad 5.2$$

$$Q_d(j, i) = \frac{g(i)A_a(i, i_0)A_r(j, i)}{\sum_{i'_0} A_a(i, i'_0) + \sum_k A_r(k, i)} \quad 5.3$$

Here, j denotes the bound state, i is the autoionizing state, i_0 is the initial state (that is, the ground state $1s$ of H-like Mg), and i'_0 is the possible final state for autoionization, which in our case is same as i_0 . The statistical weight of the doubly excited state is $g(i)$, $A_a(i, i_0)$ is the rate of autoionization from i to i_0 , $A_r(j, i)$ is the radiative rate from i to j .

When a Maxwellian distribution is used, the effective emission rate coefficient, C_S^{eff} , of the dielectronic satellite line is obtained as follows (Dubau *et al* 1980)

$$C_S^{eff}(j, i) = 3.3 \times 10^{-24} \left(\frac{I_H}{kT_e}\right)^{3/2} \frac{Q_d(j, i)}{g_o} \times \exp\left(-\frac{E_s(i)}{kT_e}\right) \text{ photons cm}^3 \text{ s}^{-1} \quad 5.4$$

Table 5.2. Wavelengths (λ in Å), radiative rates (A_r in s^{-1}), autoionization rates (A_a in s^{-1}), Auger energies (E_s in keV), branching ratio (K), intensity factors (Q_d in s^{-1}) and effective emission rate coefficients (C_{eff} in cm^3/s) ($T_e = 600$ eV) for the $2lnl'-1snl''$ transitions $n = 2, 3, 4, 5$ in He-like Mg calculated using the MZ Code. Designations: $E = 2s2s$, $C = 2s2p$, $F = 2p2p$, $C' = 2snp$, $B' = 2pns$, $A' = 2pnd$, $J' = 2pnf$, $E' = 2sns$, $G' = 2snd$, $F' = 2pnp$, $I' = 2snf$, $S = 1s2s$, $P = 1s2p$, $S' = 1sns$, $P' = 1snp$, $D' = 1snd$, $H' = 1snf$. Digits after a letter (i.e. $F155$) stand for $(2S + 1)(2L + 1)(2J + 1)$. A[B] means $A \cdot 10^B$

Labels	λ	A_r	A_a	E_s	K	Q_d	C_{eff}
<i>2l2l'-1s2l'' transitions</i>							
<i>F155-P133</i>	8.5512	2.44[13]	3.71[14]	1.040	6.17[-2]	1.15[14]	2.29[-13]
<i>F111-P133</i>	8.4457	1.90[13]	1.78[13]	1.058	5.17[-1]	9.19[12]	1.77[-14]
<i>E111-P133</i>	8.6693	5.04[12]	3.44[14]	1.021	1.45[-2]	4.97[12]	1.02[-14]
<i>F335-P335</i>	8.5327	1.82[13]	2.19[12]	1.035	6.84[-1]	7.50[12]	1.51[-14]
<i>C133-S111</i>	8.4897	1.26[13]	2.03[14]	1.042	5.87[-2]	3.56[13]	7.06[-14]
<i>C335-S313</i>	8.5180	1.22[13]	1.36[13]	1.025	4.73[-1]	3.22[13]	6.57[-14]
<i>C333-S313</i>	8.5215	1.22[13]	1.37[13]	1.024	4.70[-1]	1.94[13]	3.96[-14]
<i>C331-S313</i>	8.5231	1.22[13]	1.36[13]	1.024	4.72[-1]	6.44[12]	1.32[-14]
<i>2l3l'-1s3l'' transitions</i>							
<i>G'155-P'133</i>	8.4175	5.71[12]	8.05[13]	1.290	6.54[-2]	2.63[13]	3.45[-14]
<i>F'335-P'133</i>	8.4471	2.62[12]	2.69[13]	1.285	6.47[-2]	8.72[12]	1.15[-14]
<i>F'155-P'133</i>	8.4499	5.23[12]	6.13[13]	1.285	7.20[-2]	2.21[13]	2.92[-14]
<i>G'357-P'335</i>	8.4310	3.01[12]	2.59[12]	1.286	4.63[-1]	8.41[12]	1.11[-14]
<i>F'335-P'335</i>	8.4335	6.80[12]	2.69[13]	1.285	1.68[-1]	2.26[13]	2.99[-14]
<i>F'155-P'335</i>	8.4362	3.36[12]	6.13[13]	1.285	4.63[-2]	1.42[13]	1.88[-14]
<i>A'133-D'155</i>	8.3967	1.09[13]	4.59[12]	1.294	6.55[-1]	9.01[12]	1.17[-14]
<i>A'177-D'155</i>	8.4072	1.15[13]	2.59[13]	1.292	2.95[-1]	5.35[13]	7.00[-14]
<i>A'375-D'353</i>	8.4527	8.50[12]	4.44[12]	1.284	4.95[-1]	1.10[13]	1.46[-14]
<i>A'377-D'355</i>	8.4502	9.09[12]	5.34[12]	1.284	5.02[-1]	1.88[13]	2.49[-14]
<i>A'379-D'357</i>	8.4476	1.28[13]	5.33[12]	1.285	7.05[-1]	3.39[13]	4.49[-14]
<i>B'133-S'111</i>	8.4183	6.74[12]	9.28[13]	1.288	6.61[-2]	1.84[13]	2.42[-14]
<i>2l4l'-1s4l'' transitions</i>							
<i>A'177-D'155</i>	8.4146	1.02[13]	1.09[13]	1.371	4.42[-1]	3.37[13]	3.87[-14]
<i>A'375-D'353</i>	8.4368	8.12[12]	6.00[12]	1.367	4.40[-1]	1.32[13]	1.52[-14]
<i>A'377-D'355</i>	8.4347	7.43[12]	7.62[12]	1.367	3.73[-1]	1.99[13]	2.30[-14]
<i>A'379-D'357</i>	8.4320	1.20[13]	9.34[12]	1.367	5.63[-1]	4.73[13]	5.45[-14]
<i>B'133-S'111</i>	8.4203	6.69[12]	3.69[13]	1.369	1.46[-1]	1.62[13]	1.86[-14]
<i>2l5l'-1s5l'' transitions</i>							
<i>A'177-D'155</i>	8.4171	7.56[12]	5.04[12]	1.407	5.07[-1]	1.79[13]	1.93[-14]
<i>I'377-D'155</i>	8.4183	1.45[12]	1.70[13]	1.407	7.80[-2]	9.27[12]	1.00[-14]
<i>A'379-D'357</i>	8.4257	1.22[13]	4.41[12]	1.406	7.35[-1]	2.91[13]	3.15[-14]
<i>B'133-S'111</i>	8.4209	7.25[12]	1.84[13]	1.406	2.63[-1]	1.45[13]	1.57[-14]

where I_H is the ionization potential of hydrogen, $E_s(i)$ is the energy of the autoionizing state i relative to $1s$, and T_e is the electron temperature. The statistical weight of the initial state, i_0 , is $g_0 = 1$.

Wavelengths, radiative rates (A_r), autoionization rates (A_a), Auger energies (E_s), branching ratio (K), intensity factors (Q_d in s^{-1}) and effective emission rate coefficients (C_s^{eff} for $T_e = 600$ eV) in He-like magnesium are listed in Table 5.2. The MZ code was used to calculate radiative transitions and decays from the $2l'n l$ states in Mg^{10+} . Only transitions with the largest values for the effective emission rate coefficient, C_s^{eff} are represented. In Table 5.2, we present results for transitions without changing of principal quantum number n , the $2lnl'-1snl''$ transitions with $n = 2, 3, 4$, and 5 , that cover a spectral range of 8.3-8.6 Å.

5.4 Dielectronic Satellite Spectra for Li-Like Mg

In Table 5.3, we list wavelengths, weighted radiative rates, weighted autoionization rates, Auger energies, intensity factors, and effective emission rate coefficients for the $1s3l3l'-1s^23l$ transitions. Results are given for the $1s^2$ decay channel and the sum of the $1s^2$, $1s2s$, and $1s2p$ decay channels. Those results are given in columns labeled as '+ $1s2l$ ', while results only including the $1s^2$ channel are in columns with ' $1s^2$ ' label. In Table 5.3, we present values for transitions with the largest values for the effective emission rate coefficient, C_s^{eff} . The complete set of $[1s3s^2 + 1s3p^2 + 1s3s3d + 1s3d^2]-[1s^23p]$ and the $[1s3s3p + 1s3p3d]-[1s^23s + 1s^23d]$ transitions includes 107 transitions. We used the Hartree-Fock-Relativistic method (COWAN code) to evaluate atomic data for these transitions. The values of weighted autoionizing rates gA_a , intensity factors

Q_d , and effective emission rate coefficients C_s^{eff} are increased by 1-5 orders of magnitude. The ratios of gA_a and Q_d values evaluated by the $1s^2$ decay channel and by the sum of [$1s^2 + 1s2s +$

Table 5.3. Wavelengths (λ in Å), radiative rates (gA_r in s^{-1}), autoionization rates (gA_a in s^{-1}), Auger energies (E_s in eV), intensity factors (Q_d in s^{-1}) and effective emission rate coefficients (C_{eff} in $10^{-15} \text{ cm}^3/\text{s}$) ($T_e = 600 \text{ eV}$) for the $1s3l'1s^23l$ Li-like Mg transitions calculated using the COWAN code. Results are given for the $1s^2$ decay channel (a) and the sum of $1s^2$, $1s2s$, and $1s2p$ decay channels (b). Those results are given in columns labeled as $1s2l$. A[B] means $A \cdot 10^B$.

(a)							
Lower	Upper	λ	gA_r	gA_a	E_s	Q_d	C_{eff}
Level	Level	Å	s^{-1}	s^{-1}	eV	s^{-1}	$10^{-15} \text{ cm}^3/\text{s}$
$1s^23s^2S_{1/2}$	$1s3s3p^2P^a_{1/2}$	7.9152	8.19[12]	8.32[11]	1407.537	1.23[11]	1.33[-01]
$1s^23s^2S_{1/2}$	$1s3s3p^2P^a_{3/2}$	7.9148	1.69[13]	1.16[12]	1407.610	1.65[11]	1.78[-01]
$1s^23p^2P_{1/2}$	$1s3s3d^2D^b_{3/2}$	7.9367	3.95[12]	1.20[13]	1408.626	2.87[11]	3.13[-01]
$1s^23p^2P_{1/2}$	$1s3p^2P_{1/2}$	7.9166	9.19[12]	3.74[08]	1412.598	5.24[07]	5.72[-05]
$1s^23p^2P_{1/2}$	$1s3p^2P_{3/2}$	7.9160	4.23[12]	2.96[08]	1412.718	9.62[06]	1.05[-05]
$1s^23p^2P_{1/2}$	$1s3p^2D_{3/2}$	7.9023	1.91[12]	6.83[12]	1415.434	4.77[10]	5.21[-02]
$1s^23p^2P_{1/2}$	$1s3d^2D_{3/2}$	7.8645	1.97[12]	6.63[12]	1422.976	1.63[11]	1.78[-01]
$1s^23p^2P_{3/2}$	$1s3s3d^2D^b_{5/2}$	7.9375	6.88[12]	1.79[13]	1408.778	5.00[11]	5.46[-01]
$1s^23p^2P_{3/2}$	$1s3s3d^2D^a_{5/2}$	7.9182	1.28[12]	2.02[11]	1412.590	4.01[09]	4.38[-03]
$1s^23p^2P_{3/2}$	$1s3p^2P_{1/2}$	7.9173	4.31[12]	3.74[08]	1412.761	2.45[07]	2.68[-05]
$1s^23p^2P_{3/2}$	$1s3p^2P_{3/2}$	7.9167	2.26[13]	2.96[08]	1412.881	5.13[07]	5.60[-05]
$1s^23p^2P_{3/2}$	$1s3p^2S_{1/2}$	7.9057	2.07[12]	9.25[11]	1415.060	1.01[10]	1.10[-02]
$1s^23p^2P_{3/2}$	$1s3d^2D_{5/2}$	7.9029	3.58[12]	1.02[13]	1415.607	8.94[10]	9.76[-02]
$1s^23p^2P_{3/2}$	$1s3p^2D_{5/2}$	7.8652	3.65[12]	9.97[12]	1423.140	3.03[11]	3.31[-01]
$1s^23d^2D_{3/2}$	$1s3p3d^2D^b_{3/2}$	7.9249	1.59[12]	6.58[07]	1413.149	1.90[07]	2.03[-05]
$1s^23d^2D_{3/2}$	$1s3p3d^2F^a_{3/2}$	7.9199	1.73[13]	2.92[12]	1414.147	8.02[11]	8.55[-01]
$1s^23d^2D_{3/2}$	$1s3p3d^2D^a_{3/2}$	7.9056	1.62[13]	2.17[09]	1416.978	4.18[08]	4.44[-04]
$1s^23d^2D_{3/2}$	$1s3p3d^2D^a_{5/2}$	7.9052	2.14[12]	3.90[09]	1417.047	6.59[07]	7.00[-05]
$1s^23d^2D_{3/2}$	$1s3p3d^2P^a_{1/2}$	7.9021	6.49[12]	6.74[10]	1417.672	4.41[10]	4.68[-02]
$1s^23d^2D_{3/2}$	$1s3p3d^2F^b_{5/2}$	7.8875	1.07[13]	8.66[12]	1420.569	1.54[11]	1.63[-01]
$1s^23d^2D_{3/2}$	$1s3p3d^2P^b_{1/2}$	7.8696	2.77[12]	1.31[12]	1424.151	5.91[10]	6.20[-02]
$1s^23d^2D_{5/2}$	$1s3s3p^2P^a_{3/2}$	7.9429	1.28[12]	1.21[13]	1409.654	3.59[10]	3.86[-02]
$1s^23d^2D_{5/2}$	$1s3p3d^2D^b_{5/2}$	7.9252	2.28[12]	9.70[09]	1413.148	2.72[09]	2.91[-03]
$1s^23d^2D_{5/2}$	$1s3p3d^2F^a_{5/2}$	7.9201	1.66[12]	2.92[12]	1414.151	7.70[10]	8.21[-02]
$1s^23d^2D_{5/2}$	$1s3p3d^2F^a_{7/2}$	7.9194	2.56[13]	3.98[12]	1414.295	1.22[12]	1.30[00]
$1s^23d^2D_{5/2}$	$1s3p3d^2D^a_{3/2}$	7.9058	2.41[12]	2.17[09]	1416.982	6.22[07]	6.60[-05]
$1s^23d^2D_{5/2}$	$1s3p3d^2D^a_{5/2}$	7.9055	2.57[13]	3.90[09]	1417.050	7.94[08]	8.43[-04]
$1s^23d^2D_{5/2}$	$1s3p3d^2P^a_{3/2}$	7.9025	1.09[13]	1.50[11]	1417.644	8.09[10]	8.58[-02]
$1s^23d^2D_{5/2}$	$1s3p3d^2F^b_{7/2}$	7.8878	1.52[13]	1.15[13]	1420.561	2.18[11]	2.30[-01]
$1s^23d^2D_{5/2}$	$1s3p3d^2P^b_{3/2}$	7.8697	5.21[12]	2.63[12]	1424.174	1.11[11]	1.16[-01]

(b)							
Lower	Upper	λ	gA_r	gA_a	E_s	Q_d	C_{eff}
Level	Level	Å	s^{-1}	s^{-1}	eV	s^{-1}	$10^{-15} \text{ cm}^3/s$
$1s^2 3s \ ^2S_{1/2}$	$1s3s3p \ ^2P^a_{1/2}$	7.9152	8.19[12]	4.69[13]	68.507	6.93[12]	6.86[01]
$1s^2 3s \ ^2S_{1/2}$	$1s3s3p \ ^2P^a_{3/2}$	7.9148	1.69[13]	1.02[14]	68.580	1.44[13]	1.44[02]
$1s^2 3p \ ^2P_{1/2}$	$1s3s3d \ ^2D^b_{3/2}$	7.9367	3.95[12]	1.60[14]	69.596	3.84[12]	3.58[01]
$1s^2 3p \ ^2P_{1/2}$	$1s3p^2 \ ^2P_{1/2}$	7.9166	9.19[12]	5.21[13]	73.568	7.30[12]	7.32[01]
$1s^2 3p \ ^2P_{1/2}$	$1s3p^2 \ ^2P_{3/2}$	7.9160	4.23[12]	1.04[14]	73.688	3.36[12]	3.39[01]
$1s^2 3p \ ^2P_{1/2}$	$1s3p^2 \ ^2D_{3/2}$	7.9023	1.91[12]	2.71[14]	76.405	1.90[12]	1.85[01]
$1s^2 3p \ ^2P_{1/2}$	$1s3d^2 \ ^2D_{3/2}$	7.8645	1.97[12]	7.77[13]	83.946	1.91[12]	1.77[01]
$1s^2 3p \ ^2P_{3/2}$	$1s3s3d \ ^2D^b_{5/2}$	7.9375	6.88[12]	2.40[14]	69.748	6.69[12]	6.27[01]
$1s^2 3p \ ^2P_{3/2}$	$1s3s3d \ ^2D^a_{5/2}$	7.9182	1.28[12]	6.31[13]	73.560	1.25[12]	1.25[01]
$1s^2 3p \ ^2P_{3/2}$	$1s3p^2 \ ^2P_{1/2}$	7.9173	4.31[12]	5.21[13]	73.731	3.42[12]	3.42[01]
$1s^2 3p \ ^2P_{3/2}$	$1s3p^2 \ ^2P_{3/2}$	7.9167	2.26[13]	1.04[14]	73.851	1.79[13]	1.81[02]
$1s^2 3p \ ^2P_{3/2}$	$1s3p^2 \ ^2S_{1/2}$	7.9057	2.07[12]	1.86[14]	76.030	2.04[12]	2.03[01]
$1s^2 3p \ ^2P_{3/2}$	$1s3d^2 \ ^2D_{5/2}$	7.9029	3.58[12]	4.05[14]	76.577	3.55[12]	3.48[01]
$1s^2 3p \ ^2P_{3/2}$	$1s3p^2 \ ^2D_{5/2}$	7.8652	3.65[12]	1.17[14]	84.110	3.54[12]	3.29[01]
$1s^2 3d \ ^2D_{3/2}$	$1s3p3d \ ^2D^b_{3/2}$	7.9249	1.59[12]	3.77[12]	74.119	1.09[12]	1.08[01]
$1s^2 3d \ ^2D_{3/2}$	$1s3p3d \ ^2F^a_{3/2}$	7.9199	1.73[13]	4.40[13]	75.117	1.21[13]	1.13[02]
$1s^2 3d \ ^2D_{3/2}$	$1s3p3d \ ^2D^a_{3/2}$	7.9056	1.62[13]	6.54[13]	77.948	1.26[13]	1.25[02]
$1s^2 3d \ ^2D_{3/2}$	$1s3p3d \ ^2D^a_{5/2}$	7.9052	2.14[12]	9.86[13]	78.017	1.67[12]	1.65[01]
$1s^2 3d \ ^2D_{3/2}$	$1s3p3d \ ^2P^a_{1/2}$	7.9021	6.49[12]	2.71[12]	78.642	1.77[12]	1.71[01]
$1s^2 3d \ ^2D_{3/2}$	$1s3p3d \ ^2F^b_{5/2}$	7.8875	1.07[13]	5.89[14]	81.539	1.05[13]	1.02[02]
$1s^2 3d \ ^2D_{3/2}$	$1s3p3d \ ^2P^b_{1/2}$	7.8696	2.77[12]	5.82[13]	85.122	2.62[12]	2.51[01]
$1s^2 3d \ ^2D_{5/2}$	$1s3s3p \ ^2P^a_{3/2}$	7.9429	1.28[12]	4.27[14]	70.624	1.27[12]	1.24[01]
$1s^2 3d \ ^2D_{5/2}$	$1s3p3d \ ^2D^b_{5/2}$	7.9252	2.28[12]	5.42[12]	74.119	1.52[12]	1.51[01]
$1s^2 3d \ ^2D_{5/2}$	$1s3p3d \ ^2F^a_{5/2}$	7.9201	1.66[12]	4.40[13]	75.121	1.16[12]	1.08[01]
$1s^2 3d \ ^2D_{5/2}$	$1s3p3d \ ^2F^a_{7/2}$	7.9194	2.56[13]	5.80[13]	75.265	1.77[13]	1.66[02]
$1s^2 3d \ ^2D_{5/2}$	$1s3p3d \ ^2D^a_{3/2}$	7.9058	2.41[12]	6.54[13]	77.952	1.88[12]	1.85[01]
$1s^2 3d \ ^2D_{5/2}$	$1s3p3d \ ^2D^a_{5/2}$	7.9055	2.57[13]	9.86[13]	78.020	2.01[13]	1.98[02]
$1s^2 3d \ ^2D_{5/2}$	$1s3p3d \ ^2P^a_{3/2}$	7.9025	1.09[13]	5.95[12]	78.615	3.22[12]	3.10[01]
$1s^2 3d \ ^2D_{5/2}$	$1s3p3d \ ^2F^b_{7/2}$	7.8878	1.52[13]	7.86[14]	81.531	1.49[13]	1.45[02]
$1s^2 3d \ ^2D_{5/2}$	$1s3p3d \ ^2P^b_{3/2}$	7.8697	5.21[12]	1.16[14]	85.144	4.92[12]	4.69[01]

$1s2p$] channels are equal (see Equation 5.3). Additional increase of the ratios C_S^{eff} evaluated by the $1s^2$ decay channel and by the sum of $[1s^2 + 1s2s + 1s2p]$ channels comes from the exponential factor $\exp\left(-\frac{E_s(i)}{kT_e}\right)$ in Equation 5.4. The ratio of Auger energies for the $1s^2$ decay and for the $1s2l$ decays are equal to 17-20. The spectral range covered by Table 5.3 is 7.8-8 Å.

Table 5.4. Wavelengths (λ in Å), radiative rates (gA_r in s^{-1}), autoionization rates (gA_a in s^{-1}), Auger energies (E_s in eV), intensity factors (Q_d in s^{-1}) and effective emission rate coefficients (C_{eff} in $10^{-15} \text{ cm}^3/\text{s}$) ($T_e = 600 \text{ eV}$) for the $1s3l4l'-1s^24l$ Li-like Mg transitions calculated using the Cowan Code. Results are given for the $1s^2$ decay channel (a) and the sum of $1s^2$, $1s2s$, and $1s2p$ decay channels (b). Those results are given in columns labeled as $1s2l$. A[B] means $A \cdot 10^B$.

(a)							
Lower	Upper	λ	gA_r	gA_a	E_s	Q_d	C_{eff}
Level	Level	Å	s^{-1}	s^{-1}	eV	s^{-1}	$10^{-15} \text{ cm}^3/\text{s}$
$1s^24s^2S_{1/2}$	$1s3p4s^2P^b_{3/2}$	7.8778	7.01[12]	4.18[12]	1485.7	3.29[11]	3.11[-1]
$1s^24p^2P_{3/2}$	$1s3p4p^2P^a_{3/2}$	7.8759	1.25[13]	8.88[07]	1482.9	1.02[07]	9.70[-6]
$1s^24d^2D_{3/2}$	$1s3d4p^2D^a_{3/2}$	7.8679	7.96[12]	1.81[09]	1490.7	1.98[08]	1.86[-4]
$1s^24d^2D_{5/2}$	$1s3d4p^2D^a_{5/2}$	7.8678	1.23[13]	3.62[09]	1490.8	4.04[08]	3.79[-4]
$1s^24d^2D_{5/2}$	$1s3d4p^2F^b_{7/2}$	7.8580	8.20[12]	7.80[12]	1492.7	1.22[11]	1.14[-1]
$1s^24f^2F_{5/2}$	$1s3p4f^2G^a_{7/2}$	7.8657	2.40[13]	4.43[08]	1485.8	4.45[07]	4.21[-5]
$1s^24f^2F_{7/2}$	$1s3p4f^2G^a_{9/2}$	7.8656	3.13[13]	5.57[08]	1485.9	6.74[07]	6.38[-5]
$1s^24f^2F_{7/2}$	$1s3d4d^2F^a_{7/2}$	7.8629	1.70[13]	3.66[08]	1486.4	9.64[07]	9.12[-5]
$1s^24f^2F_{7/2}$	$1s3p4f^2G^b_{9/2}$	7.8497	1.29[13]	1.37[12]	1489.0	2.89[10]	2.72[-2]
$1s^24f^2F_{7/2}$	$1s3p4f^2F^a_{7/2}$	7.8708	2.04[13]	1.93[10]	1484.8	8.72[09]	8.27[-3]
$1s^24f^2F_{5/2}$	$1s3d4d^2F^a_{5/2}$	7.8631	1.16[13]	4.16[10]	1486.4	3.99[10]	3.77[-2]
$1s^24f^2F_{7/2}$	$1s3p4f^2D^a_{5/2}$	7.8571	1.62[13]	2.74[12]	1487.6	7.55[11]	7.12[-1]
$1s^24f^2F_{5/2}$	$1s3p4f^2G^b_{7/2}$	7.8496	1.02[13]	1.10[12]	1489.1	2.33[10]	2.19[-2]
$1s^24f^2F_{5/2}$	$1s3p4f^2D^a_{3/2}$	7.8485	5.48[12]	1.20[12]	1489.3	4.25[11]	4.00[-1]
$1s^24f^2F_{7/2}$	$1s3p4f^2D^a_{5/2}$	7.8485	8.20[12]	2.74[12]	1489.3	6.32[11]	5.95[-1]
(b)							
Lower	Upper	λ	gA_r	gA_a	E_s	Q_d	C_{eff}
Level	Level	Å	s^{-1}	s^{-1}	eV	s^{-1}	$10^{-15} \text{ cm}^3/\text{s}$
$1s^24s^2S_{1/2}$	$1s3p4s^2P^b_{3/2}$	7.8778	7.01[12]	8.10[13]	146.7	6.37[12]	5.36[1]
$1s^24p^2P_{3/2}$	$1s3p4p^2P^a_{3/2}$	7.8759	1.25[13]	8.96[13]	143.9	1.03[13]	9.12[1]
$1s^24d^2D_{3/2}$	$1s3d4p^2D^a_{3/2}$	7.8679	7.96[12]	6.04[13]	151.7	6.61[12]	5.78[1]
$1s^24d^2D_{5/2}$	$1s3d4p^2D^a_{5/2}$	7.8678	1.23[13]	9.12[13]	151.8	1.02[13]	8.90[1]
$1s^24d^2D_{5/2}$	$1s3d4p^2F^b_{7/2}$	7.8580	8.20[12]	5.16[14]	153.7	8.05[12]	6.94[1]
$1s^24f^2F_{5/2}$	$1s3p4f^2G^a_{7/2}$	7.8657	2.40[13]	2.13[14]	146.8	2.14[13]	1.89[2]
$1s^24f^2F_{7/2}$	$1s3p4f^2G^a_{9/2}$	7.8656	3.13[13]	2.28[14]	146.8	2.75[13]	2.43[2]
$1s^24f^2F_{7/2}$	$1s3d4d^2F^a_{7/2}$	7.8629	1.70[13]	4.66[13]	147.4	1.23[13]	1.08[2]
$1s^24f^2F_{7/2}$	$1s3p4f^2G^b_{9/2}$	7.8497	1.29[13]	5.96[14]	150.0	1.26[13]	1.10[2]
$1s^24f^2F_{7/2}$	$1s3p4f^2F^a_{7/2}$	7.8708	2.04[13]	2.35[13]	145.8	1.06[13]	9.37[1]
$1s^24f^2F_{5/2}$	$1s3d4d^2F^a_{5/2}$	7.8631	1.16[13]	9.67[12]	147.3	4.47[12]	8.14[1]
$1s^24f^2F_{7/2}$	$1s3p4f^2D^a_{5/2}$	7.8571	1.62[13]	4.07[13]	148.5	1.12[13]	9.27[1]
$1s^24f^2F_{5/2}$	$1s3p4f^2G^b_{7/2}$	7.8496	1.02[13]	4.72[14]	150.0	1.00[13]	8.75[1]
$1s^24f^2F_{5/2}$	$1s3p4f^2D^a_{3/2}$	7.8485	5.48[12]	1.83[13]	150.3	3.57[12]	5.35[1]
$1s^24f^2F_{7/2}$	$1s3p4f^2D^a_{5/2}$	7.8485	8.20[12]	4.07[13]	150.3	5.67[12]	7.73[1]

In Table 5.4, we list wavelengths, weighted radiative rates, weighted autoionization rates, Auger energies, intensity factors, and effective emission rate coefficients for the $1s3l4l'$ - $1s^24l$ transitions. We present values for transitions with largest values of the effective emission rate coefficients C_S^{eff} . Complete set of the $[1s3s4s + 1s3s4d + 1s3p4p + 1s3p4f + 1s3d4s + 1s3d4d]$ - $[1s^23p + 1s^24p + 1s^24f]$ transitions includes 420 transitions. We used the the Hartree-Fock-Relativistic method (COWAN code) to evaluate atomic data for these transitions. Comparison values given in columns with $1s^2$ and $1s2l$ labels of Table 5.4 show large differences between evaluated data. The values of weighted autoionizing rates gA_a , intensity factors Q_d , and effective emission rate coefficients C_S^{eff} are increased by 1-5 orders of magnitude. The ratios of gA_a and Q_d values evaluated by the $1s^2$ decay channel and by the sum of $[1s^2 + 1s2s + 1s2p]$ channels are equal (see Equation 5.4). Additional increase of the ratios C_S^{eff} evaluated by the $1s^2$ decay channel and by the sum of $[1s^2 + 1s2s + 1s2p]$ channels comes from the exponential factor $\exp\left(-\frac{E_S(i)}{kT_e}\right)$ in Equation 5.4. The ratio of Auger energies for the $1s^2$ decay and for the $1s2l$ decays is about a factor of 10. The spectral range covered by Table 5.4 is 7.8-7.9 Å.

5.5 Dielectronic Satellite Spectra for Be-Like Mg

In Table 5.5, we list wavelengths, weighted radiative rates, weighted autoionization rates, Auger energies, intensity factors, and effective emission rate coefficients for the $1s3l3l'3l''$ - $1s^23l3l'$ transitions. Results are given for the $1s^23l$ decay channel and the sum of the $1s2l3l'$ decay channels. These results are given in columns labeled as $1s2l3l'$, while results only including the $1s^23l$ channel are in columns with the $1s^23l$ label. In Table 5.5, we present values for transitions with the largest values for the effective emission rate coefficient, C_S^{eff} . We used the Hartree-Fock-Relativistic method (COWAN code) to evaluate atomic data for these transitions. The spectral range covered by Table 5.5 is 7.8-8 Å.

Table 5.5. Wavelengths (λ in Å), radiative rates (gA_r in s^{-1}), autoionization rates (gA_a in s^{-1}), Auger energies (E_s in eV), intensity factors (Q_d in s^{-1}) and effective emission rate coefficients (C_{eff} in $10^{-15} \text{ cm}^3/\text{s}$) ($T_e = 600 \text{ eV}$) for the $1s^2 3l' - 1s 3l' 3l''$ Li-like Mg transitions calculated using the COWAN Code. In the first two columns, we use shorter labeling: $3l' / 3l'$ instead of $1s^2 3l' / 1s 3l' 3l''$ and $3l' / 3l''$ instead of $1s 3l' 3l''$. Results are given for the $1s^2 3l'$ (a) and $1s 2l' 3l'$ decay channels and the sum of these channels (b). Those results are given in columns labelled as $1s 2l' 3l'$. A[B] means $A \cdot 10^B$.

(a)							
Lower	Upper	λ	gA_r	gA_a	E_s	Q_d	C_{eff}
$1s^2 3l' / 3l'$	$1s 3l' 3l' / 3l''$	Å	s^{-1}	s^{-1}	eV	s^{-1}	$10^{-15} \text{ cm}^3/\text{s}$
$3p^2 1D_2$	$3s 3p 3d 1F_3^b$	7.9842	1.13[13]	9.12[12]	1425.6	3.34[10]	3.50[-02]
$3d^2 1D_2$	$3p 3d^2 1F_3$	7.9790	1.11[13]	3.41[12]	1434.5	2.25[10]	2.32[-02]
$3s 3d 3D_1$	$3s 3p 3d 3F_2^a$	7.9746	1.11[13]	3.34[12]	1421.8	4.39[10]	4.62[-02]
$3s 3d 3D_2$	$3s 3p 3d 3F_3^a$	7.9744	1.65[13]	4.62[12]	1421.8	6.42[10]	6.76[-02]
$3s 3d 3D_3$	$3s 3p 3d 3F_4^a$	7.9741	2.41[13]	5.86[12]	1421.9	9.20[10]	9.69[-02]
$3d^2 3F_2$	$3p 3d^2 3G_3^a$	7.9737	1.55[13]	3.65[12]	1431.5	5.84[10]	6.05[-02]
$3d^2 3F_3$	$3p 3d^2 3G_4^a$	7.9734	2.03[13]	4.71[12]	1431.6	7.69[10]	7.97[-02]
$3d^2 3F_4$	$3p 3d^2 3G_5^a$	7.9730	2.68[13]	5.78[12]	1431.7	1.02[11]	1.06[-01]
$3s 3d 1D_2$	$3p^3 1D_2$	7.9715	2.43[13]	1.17[13]	1421.2	1.42[11]	1.50[-01]
$3p^2 3P_2$	$3p^3 3S_1$	7.9695	1.41[13]	6.22[10]	1424.6	5.74[08]	6.02[-04]
$3d^2 3P_2$	$3p 3d^2 3D_3^a$	7.9680	1.75[13]	4.74[12]	1435.3	1.36[11]	1.40[-01]
$3d^2 1G_4$	$3p 3d^2 1G_4$	7.9678	2.33[13]	5.50[11]	1435.3	2.45[09]	2.52[-03]
$3s^2 1S_0$	$3s^2 3p 1P_1$	7.9625	1.24[13]	1.39[13]	1414.3	1.14[11]	1.22[-01]
$3s 3d 3D_2$	$3s 3p 3d 3D_2^a$	7.9618	1.34[13]	1.80[12]	1424.3	1.80[10]	1.89[-02]
$3s 3d 3D_3$	$3s 3p 3d 3D_3^a$	7.9617	2.41[13]	2.41[12]	1424.3	3.13[10]	3.28[-02]
$3p^2 1D_2$	$3p^3 1D_2$	7.9600	2.09[13]	1.37[13]	1430.3	9.94[10]	1.03[-01]
$3d^2 1G_4$	$3p 3d^2 1H_5$	7.9551	5.23[13]	2.94[13]	1437.8	1.48[11]	1.52[-01]
$3d^2 1D_2$	$3p 3d^2 1F_3$	7.9530	1.54[13]	1.21[13]	1439.6	7.91[10]	8.09[-02]
$3s 3d 1D_2$	$3p^3 1P_1$	7.9500	1.13[13]	7.84[12]	1425.4	4.62[10]	4.84[-02]
$3d^2 1D_2$	$3p 3d^2 1D_2$	7.9415	1.18[13]	6.14[12]	1441.8	6.49[10]	6.61[-02]
$3d^2 1G_4$	$3p 3d^2 1G_4$	7.9362	1.89[13]	7.56[12]	1441.5	2.90[10]	2.96[-02]
$3d^2 1G_4$	$3p 3d^2 1F_3$	7.9244	2.41[13]	2.78[12]	1443.8	1.25[10]	1.27[-02]
$3p 3d 1F_3$	$3p^2 3d 1G_4$	7.9949	1.65[13]	2.65[13]	1428.9	8.43[10]	8.77[-02]
$3p 3d 1D_2$	$3s 3d^2 1F_3$	7.9816	1.17[13]	2.54[13]	1425.0	1.31[11]	1.37[-01]
$3p 3d 1F_3$	$3p^2 3d 1F_3$	7.9700	1.98[13]	9.87[12]	1433.8	5.17[10]	5.34[-02]
$3p 3d 3F_4$	$3p^2 3d 3G_5$	7.9651	1.68[13]	4.72[13]	1428.2	1.10[11]	1.15[-01]
$3p 3d 3F_4$	$3p^2 3d 3G_4$	7.9651	2.07[13]	2.28[13]	1428.2	1.09[11]	1.14[-01]
$3s 3p 1P_1$	$3s 3p^2 1P_1$	7.9634	1.80[13]	7.41[12]	1422.4	5.61[10]	5.90[-02]
$3p 3d 1F_3$	$3p^2 3d 1F_3$	7.9519	1.31[13]	1.21[13]	1437.3	3.50[10]	3.59[-02]
$3p 3d 1F_3$	$3p^2 3d 1D_2$	7.9462	1.30[13]	7.98[12]	1438.4	3.03[10]	3.10[-02]
$3p 3d 1D_2$	$3p^2 3d 1F_3$	7.9366	1.21[13]	9.87[12]	1433.8	3.16[10]	3.26[-02]

(b)

Lower	Upper	λ	gA_r	gA_a in s^{-1}	E_s	Q_d	C_{eff}
$1s^23l3l'$	$1s3l3l''$	\AA	s^{-1}	ΣgA_a	eV	s^{-1}	$10^{-15} \text{ cm}^3/s$
$3p^2^1D_2$	$3s3p3d^1F_3^b$	7.9842	1.13[13]	3.06[15]	102.7	1.12[13]	1.06[02]
$3d^2^1D_2$	$3p3d^2^1F_3$	7.9790	1.11[13]	1.67[15]	111.6	1.10[13]	1.03[02]
$3s3d^3D_1$	$3s3p3d^3F_2^a$	7.9746	1.11[13]	8.33[14]	98.8	1.10[13]	1.05[02]
$3s3d^3D_2$	$3s3p3d^3F_3^a$	7.9744	1.65[13]	1.17[15]	98.9	1.62[13]	1.55[02]
$3s3d^3D_3$	$3s3p3d^3F_4^a$	7.9741	2.41[13]	1.51[15]	99.0	2.37[13]	2.26[02]
$3d^2^3F_2$	$3p3d^2^3G_3^a$	7.9737	1.55[13]	9.51[14]	108.6	1.52[13]	1.43[02]
$3d^2^3F_3$	$3p3d^2^3G_4^a$	7.9734	2.03[13]	1.22[15]	108.7	2.00[13]	1.88[02]
$3d^2^3F_4$	$3p3d^2^3G_5^a$	7.9730	2.68[13]	1.50[15]	108.8	2.63[13]	2.47[02]
$3s3d^1D_2$	$3p^3^1D_2$	7.9715	2.43[13]	1.98[15]	98.2	2.40[13]	2.29[02]
$3p^2^3P_2$	$3p^3^3S_1$	7.9695	1.41[13]	1.51[15]	101.6	1.39[13]	1.32[02]
$3d^2^3P_2$	$3p3d^2^3D_3^a$	7.9680	1.75[13]	5.89[14]	112.4	1.69[13]	1.58[02]
$3d^2^1G_4$	$3p3d^2^1G_4$	7.9678	2.33[13]	5.20[15]	112.4	2.32[13]	2.17[02]
$3s^2^1S_0$	$3s^23p^1P_1$	7.9625	1.24[13]	1.50[15]	91.4	1.23[13]	1.19[02]
$3s3d^3D_2$	$3s3p3d^3D_2^a$	7.9618	1.34[13]	1.32[15]	101.4	1.32[13]	1.26[02]
$3s3d^3D_3$	$3s3p3d^3D_3^a$	7.9617	2.41[13]	1.83[15]	101.4	2.38[13]	2.26[02]
$3p^2^1D_2$	$3p^3^1D_2$	7.9600	2.09[13]	2.85[15]	107.4	2.07[13]	1.95[02]
$3d^2^1G_4$	$3p3d^2^1H_5$	7.9551	5.23[13]	1.04[16]	114.8	5.20[13]	4.84[02]
$3d^2^1D_2$	$3p3d^2^1F_3$	7.9530	1.54[13]	2.32[15]	116.6	1.52[13]	1.41[02]
$3s3d^1D_2$	$3p^3^1P_1$	7.9500	1.13[13]	1.91[15]	102.4	1.13[13]	1.07[02]
$3d^2^1D_2$	$3p3d^2^1D_2$	7.9415	1.18[13]	1.10[15]	118.9	1.16[13]	1.07[02]
$3d^2^1G_4$	$3p3d^2^1G_4$	7.9362	1.89[13]	4.91[15]	118.6	1.88[13]	1.74[02]
$3d^2^1G_4$	$3p3d^2^1F_3$	7.9244	2.41[13]	5.30[15]	120.9	2.40[13]	2.21[02]
$3p3d^1F_3$	$3p^23d^1G_4$	7.9949	1.65[13]	5.16[15]	106.0	1.64[13]	1.55[02]
$3p3d^1D_2$	$3s3d^2^1F_3$	7.9816	1.17[13]	2.25[15]	102.0	1.16[13]	1.10[02]
$3p3d^1F_3$	$3p^23d^1F_3$	7.9700	1.98[13]	3.75[15]	110.8	1.97[13]	1.84[02]
$3p3d^3F_4$	$3p^23d^3G_5$	7.9651	1.68[13]	7.21[15]	105.2	1.68[13]	1.59[02]
$3p3d^3F_4$	$3p^23d^3G_4$	7.9651	2.07[13]	4.31[15]	105.2	2.06[13]	1.95[02]
$3s3p^1P_1$	$3s3p^2^1P_1$	7.9634	1.80[13]	2.36[15]	99.5	1.79[13]	1.71[02]
$3p3d^1F_3$	$3p^23d^1F_3$	7.9519	1.31[13]	4.51[15]	114.4	1.31[13]	1.22[02]
$3p3d^1F_3$	$3p^23d^1D_2$	7.9462	1.30[13]	3.42[15]	115.5	1.30[13]	1.21[02]
$3p3d^1D_2$	$3p^23d^1F_3$	7.9366	1.21[13]	3.75[15]	110.8	1.20[13]	1.12[02]

5.6 Comparison to Experimental Spectra

A comparison can now be made between the experimentally collected K-shell Mg spectra and the theoretically calculated dielectronic satellite lines. Three different laser parameters are

investigated to determine differences between various combinations of contrasts and pulse durations. The parameters discussed include high contrast with fs pulse, low contrast with fs pulse, and low contrast with ns pulse as described in Table 5.1.

Figure 5.1 displays spectra from the two spectrometers fielded in the experiments. Figure 5.1a shows the K-shell Mg spectra measured with the KAP spectrometer compared to the

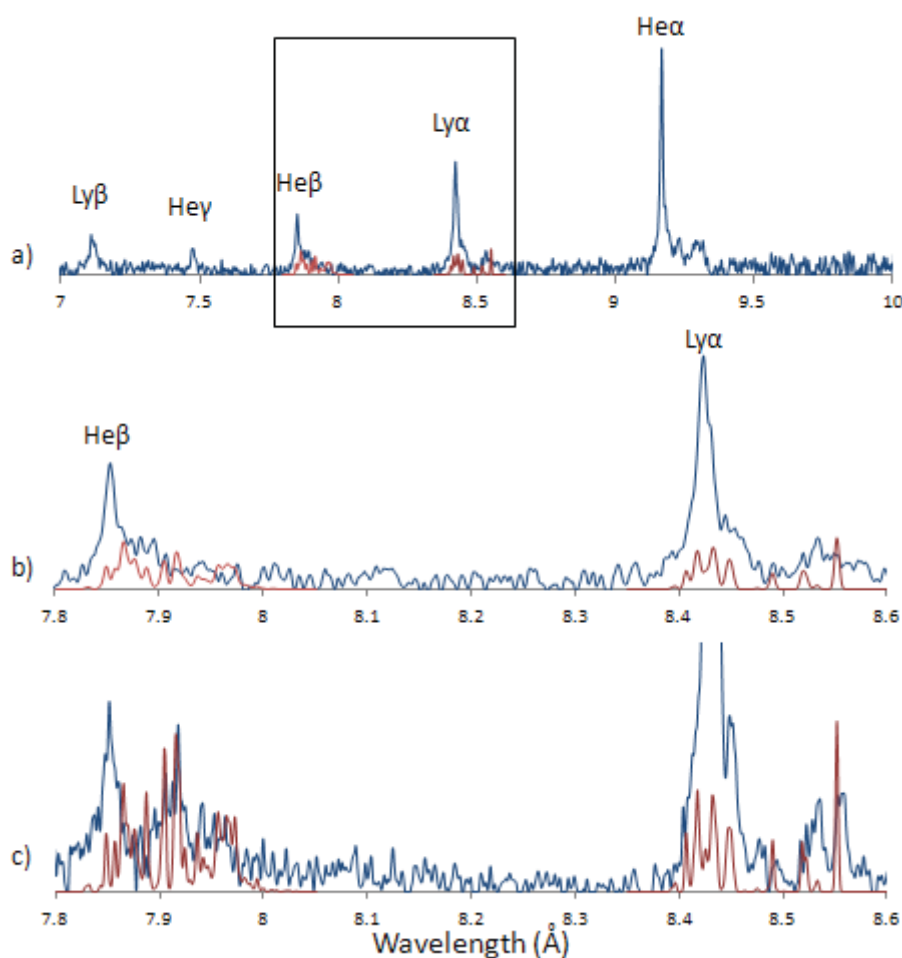


Figure 5.1. K-shell Mg spectra recorded in high contrast (10^{-7}) and 350 fs pulse experiment by the FSSR and KAP spectrometers compared to synthetic spectra: a) Synthetic spectra with experimental KAP spectra. The boxed region highlights the area of focus for spectra comparison. b) KAP spectra with synthetic spectra from boxed region. c) FSSR spectra with synthetic spectra.

synthetic spectra. The region highlighted in the box represents the spectral range that is the main focus of comparison with the theoretical calculations from Tables 5.2-5.4. Figure 5.1b and 5.1c show the experimental and theoretical spectra from the KAP and FSSR spectrometers respectively. Comparing the experimental spectra from the two spectrometers highlights the better resolution for the FSSR spectra as seen in the greater definition of the satellites being described with the theoretical spectra.

Figure 5.2 shows the experimental spectra for three different laser conditions collected by the KAP spectrometer compared to modeling from a nonlocal thermodynamic equilibrium (non-LTE) kinetics model (A.S. Safronova *et al* 2007). The Mg model includes all ionization stages with detailed structure. Notably H-like states up to $n=6$, singly excited He-like states up to $n=5$, and singly excited Li-like states up to $n=4$. The FAC code (Gu 2004) was used to provide radiative and collisional rate data and energy levels. The modeling provides approximate electron temperatures and densities for the plasma. Figure 5.2a is for high contrast with fs laser pulse duration modeled with electron temperature of 320 eV and electron density of $3 \times 10^{20} \text{ cm}^{-3}$. The spectrum recorded at low contrast with fs laser pulse duration is shown in Figure 5.2b and matched to modeling using 320 eV and $3 \times 10^{20} \text{ cm}^{-3}$. Low contrast with ns pulse duration is shown in Figure 5.2c. The modeling parameters were 350 eV and $2 \times 10^{20} \text{ cm}^{-3}$. The boxed region highlights the spectral range of interest for satellites represented in the tables. Figure 5.2c shows more narrow resonance lines than those recorded at other experimental conditions, which is consistent with what was previously noticed for L-shell Cu (A.S. Safronova *et al* 2012b). The more narrow lines were found to be described better with the addition of a small percentage of hot electrons. Hot electrons were not used for the Mg spectra here due to changes in the fraction of hot electron showing the same trends as temperature changes. This is largely due to the small number of ionization stages found in K-shell spectra (only H-like and He-like). Future studies will look deeper into the significance of the hot electrons. Figure 5.2 is used to show how the

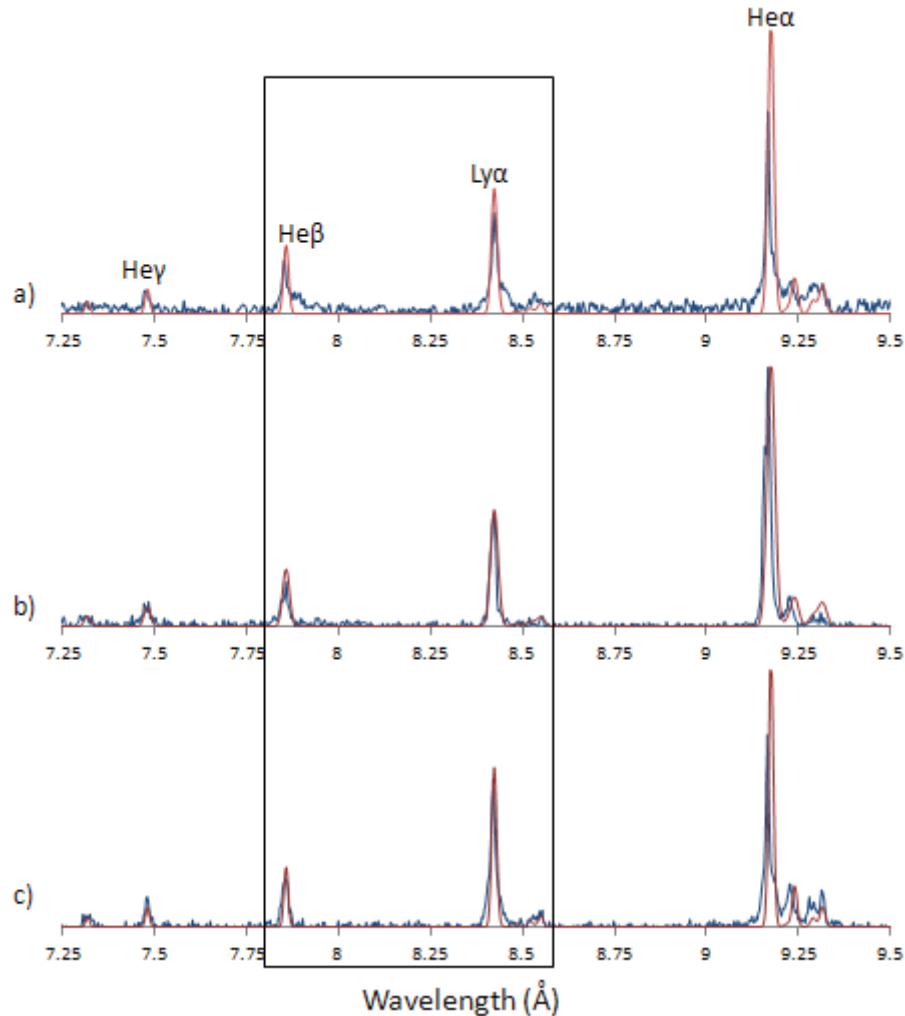


Figure 5.2. Experimental spectra recorded by KAP spectrometer for: a) High contrast (10^{-7}) and 350 fs pulse with non-LTE kinetic modeling at electron temperature of 320 eV and electron density of $3 \times 10^{20} \text{ cm}^{-3}$, b) Low contrast (10^{-5}) and 350 fs pulse with non-LTE kinetic modeling at electron temperature of 320 eV and electron density of $3 \times 10^{20} \text{ cm}^{-3}$, and c) Low contrast (10^{-5}) and 0.8 ns pulse with non-LTE kinetic modeling at electron temperature of 350 eV and electron density of $2 \times 10^{20} \text{ cm}^{-3}$. Boxed region highlights spectral range of focus for satellite studies.

satellites differ between shots. For high contrast and fs pulse, the satellites are very strong throughout the spectra. Figure 5.2b shows how the satellites are significantly less prominent for low contrast with fs pulse. Figure 5.2c shows even fewer satellites for low contrast and ns pulse. The KAP spectrometer provides a quick comparison while the FSSR spectrometer will be used for detailed analysis for each set of parameters.

Figure 5.3 shows the experimental spectra collected with the FSSR spectrometer for experiments with high contrast (5.3a, 5.3c, and 5.3e) and low contrast (5.3b, 5.3d, and 5.3f). Both experiments had a 350 fs laser pulse duration. The experimental spectra are compared to the dielectronic satellite calculations. The satellite lines are universally broadened using a Gaussian profile and are magnitude adjusted on a table by table basis to best match the experimental spectrum.

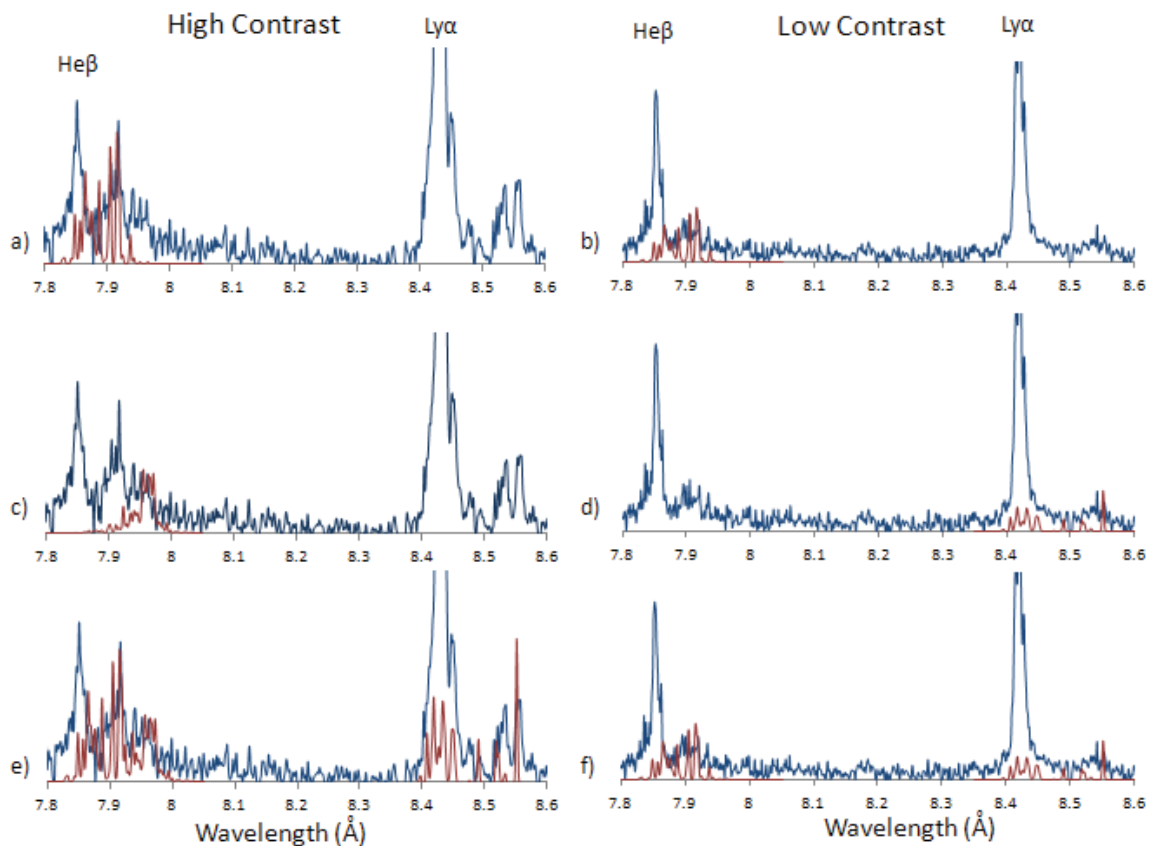


Figure 5.3. K-shell Mg spectra from high contrast (10^{-7}) and 350 fs pulse (a, c, e) and low contrast (10^{-5}) and 350 fs pulse (b, d, f) experiments recorded by FSSR spectrometer. Synthetic spectra (red) compared to experimental data (blue) which include: a), b) Li-like $1s3l3l'-1s^23l$ transitions as described in Table 5.3 combined with Li-like $1s3l4l'-1s^24l$ transitions as described in Table 5.4. c) Be-Like transitions as described by Table 5.5. d) He-like $2lnl'-1snl''$ transitions with $n = 2,3,4,5$ as described in Table 5.2. e) All Tables with the region around 8.4 – 8.6 Å described with He-like $2lnl'-1snl''$ transitions from Table 5.2. f) Combination of Tables 5.2, 5.3, and 5.4.

Figure 5.3a shows Li-like transitions from Table 5.3 and Table 5.4 compared to the high contrast experimental spectrum. Most of these transitions are separated from their resonance line, He β . There is a large cluster of satellite lines in the region of 7.88 – 7.93 Å. Many of the Table 5.3 transitions lie within this range. The highest wavelength lines within this cluster are closely matched by the theoretical calculations. The Table 5.4 transitions cover the region from 7.85 – 7.89 Å. This region contains satellite structures that are not completely resolved from the He β line and the lowest wavelength satellites of the structures described by Table 5.3 transitions. There is a small gap just below 7.9 Å that is not described by the calculations and it exists for all experiments. Figure 5.3b shows the low contrast spectrum with the Table 5.3 and 5.4 transitions. Looking at the experimental spectra it is easy to see that the satellite clusters from Figure 5.3a are much less pronounced. Transitions from Table 5.3 and 5.4 are able to strongly match the low contrast experiment much the same as for the high contrast experiment.

Figure 5.3c shows the Be-like transitions from Table 5.5 compared to the high contrast experimental spectrum. These transitions cover the satellite structure on the higher wavelength side of the Li-like transitions. The Be-like transitions strongly describe the region of 7.95 – 7.98 Å. On the lower wavelength side of that region, less prominent Be-like transitions combine with Li-like transitions to improve the synthetic spectrum's matching of the region of 7.93 – 7.95 Å as shown in Figure 5.3e. Be-like transitions were not as significant in the low contrast experiment and therefore Be-like transitions are not shown for comparison. Figure 5.3d shows Table 5.2 transitions compared to the low contrast experimental spectrum. The Ly α satellites are much weaker than for the high contrast experiment and the Table 5.2 transitions do not provide strong evidence for the existence of the $2lnl'-1snl''$ transitions.

Figure 5.3e compares all theoretical calculations from Tables 5.2-5.5 with the experimental data. The transitions near the Ly α line are from Table 5.2. Most of these transitions

are too close to the resonance line to resolve, however, some do match with minor peaks extending from the resonance line. There is also one cluster of lines at approximately 8.48 Å that nicely matches a small experimental peak. There are strong satellite lines at 8.53 and 8.55 Å that are well known $2l2l' - 1s2l$ transitions. They are not fully described in our synthetic spectra due to maintaining a consistent broadening coefficient between the different tables. Figure 5.3f combines all the He-like and Li-like satellite transitions for comparison with the low contrast experimental spectrum. Figure 5.3f highlights the reduced satellite structure found in the low contrast experiment.

Figure 5.4 compares FSSR spectra from the low contrast and ns pulse experiment, with the theoretical calculations. This experiment has a similar appearance to the low contrast and fs pulse experiment with the less pronounced satellite clusters. Satellites to the Ly α line are not defined between 8.45 and 8.5 Å and satellites to the He β line are very weak. Attempts to match the experimental data do not provide evidence that the desired satellite lines exceed the noise in the spectra.

5.7 Conclusions

Laser produced plasmas have been shown to be excellent sources for satellite structure studies. Satellite transitions provide opportunities to test and improve atomic codes as well as increase our understanding of the processes that create plasma radiation. This paper discussed new K-shell Mg experimental data collected using different parameters of laser irradiation. The satellite structures between the Ly α and He β resonance lines were investigated dependent on experimental conditions. Synthetic spectra of dielectronic satellite lines are evaluated using energy levels, radiative transition probabilities, and autoionization rates for the $2l'nl - 1snl'$ $n = 2,3,4,5$, $1s3l'l' - 1s^23l$, and $1s3l'l' - 1s^24l$ transitions in He-like and Li-like Mg using the quasi-

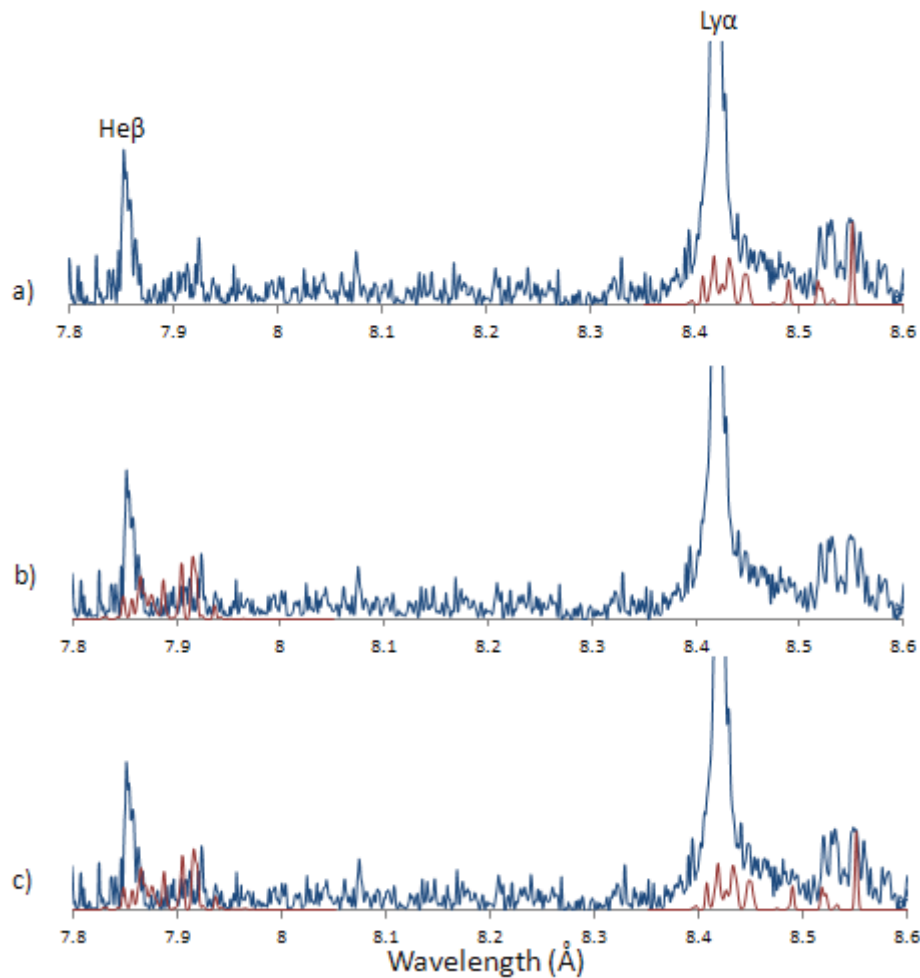


Figure 5.4. K-shell Mg spectra from low contrast (10^{-5}) and 0.8 ns pulse experiment recorded by FSSR spectrometer. Synthetic spectra (red) compared to experimental data (blue) which include: a) He-like $2lnl'-1snl''$ transitions with $n = 2,3,4,5$ as described in Table 5.2. b) Li-like Mg $1s3l/3l'-1s23l$ transitions as described in Table 5.3. c) Combination of Tables 5.2, 5.3, and 5.4.

relativistic many-body perturbation theory (MZ) code. These transitions were compared to spectra collected from experiments with three different conditions related to contrast and pulse duration. It was found that high contrast (10^{-7}) and short pulse (350 fs) produced the best satellite data. Synthetic spectra from our dielectronic satellite calculations did a good job describing the spectral features next to the He β line, while calculations for satellites near the Ly α line matched location. Spectra from shots with low contrast (10^{-5}) reduced the presence of the satellite lines and

the synthetic spectra matching dropped in quality as a result. Finally, lengthening the pulse (0.8 ns) while lowering the contrast (10^{-5}) caused the satellite structures to not be distinguishable from the noise. Synthetic spectra matching were poor for these conditions. Transitions of the form $2l'nl - 1snl'$ $n = 2,3,4,5$ (Table 5.2) were found to be a good match for some satellites near the Ly α line. Transitions of the form $1s3/3l' - 1s^23l$ (Table 5.3) and $1s3/4l' - 1s^24l$ (Table 5.4) matched most of the satellites near the He β line. It was shown that dielectronic recombination can be used to describe most satellite transitions to the He β resonance line with only small gaps where the calculations were not adequate.

A comprehensive study of satellite structure between 7.8 – 8.6 Å from Mg ions is accomplished. Experiments at different conditions were performed that were able to affect the intensity of satellite structures for K-shell Mg. Relativistic calculations of dielectronic recombination satellites matched well the experimental spectra. These calculations proved that the primary contribution in the most intense satellite spectra, at high contrast and fs pulse duration, were from dielectronic recombination satellites.

Chapter 6

Influence of Hot Electrons on the Spectra of Fe Plasma Irradiated by Femtosecond Laser Pulses

6.1 Introduction to K-shell Fe Plasma from Femtosecond Laser Pulses

Observations of astrophysical phenomena have been a continual source of x-ray spectra for many years. Through spectroscopic analysis, these spectra provide clues to understanding the processes that create the various plasmas seen throughout the universe. The spectra point out gaps in our understanding, such as important lines and atomic data details, and targeted laboratory experiments can help fill in those gaps (Beiersdorfer 2003). Iron is an important element in solar (Jain *et al* 2006 and Phillips 2012) and other star systems (Eze 2014 and Ponti *et al* 2015) and for that reason x-ray Fe spectra have been studied in laboratory experiments using many different plasma sources, including: electron beam ion traps (Decaux *et al* 1995, Decaux *et al* 1997, and Drake *et al* 1999), tokamaks (Beiersdorfer *et al* 1993, 2001), and X-pinchs (A.S. Safronova *et al* 2009a).

There have been many improvements in the understanding of Fe x-ray spectra, however, there is more to learn about the different processes involved in x-ray formation with respect to the roles of fast electron beams and x-ray pumping for spectra in laboratory and astrophysics for both low and high density plasmas. One of the important points is to understand the possible role of x-ray photo pumping. In recent investigations with ultra-relativistic laser produced plasma it was found that photo-pumping was affecting the spectra of medium z targets such as Al (Colgan *et al* 2013, Pikuz *et al* 2013, Hansen *et al* 2014, and Faenov *et al* 2015). It was shown in (Faenov *et al* 2015) that femtosecond laser pulses with intensity reaching 10^{21} W/cm² at the surface of some

microns Al foils could generate x-ray source with intensity of 10^{17} W/cm² and such intensity already enough for photo-pumping generation of hollow KK and KL ions. Here spectra of higher z material (Fe) collected from the same experimental conditions as seen in the Al experiments are analyzed to see the roles of fast electron beams and x-ray pumping.

6.2 Description of Experiments

The experiments are performed using the J-KAREN (Kiriya *et al* 2010 and Nishiuchi *et al* 2015) that is described in section 2.3. Spectra were recorded from plasma created by 2 μ m stainless steel Fe foils irradiated by ~ 7 J, 35 fs laser pulses. Spectroscopy measurements were collected with a Focusing Spectrometer with Spatial Resolution (FSSR) (Faenov *et al* 1994 and Blasco *et al* 2001). The spectrometer was equipped with a spherically bent quartz (31-40) crystal with a lattice spacing $2d \sim 2.36$ Å and a radius of curvature of $R = 150$ mm. The crystal was aligned to record K-shell emission spectra of multi-charged (He_{α} line of Fe XXV and Ly_{α} line of Fe XXVI) and neutral (i.e. K_{α} , K_{β} lines) Fe ions in 1.7 – 1.97 Å wavelength range. The FSSR spectral resolving power was approximately 3000. The spectrometer, observed the laser-irradiated front surface of the target at an angle of $\sim 40^{\circ}$ to the target surface normal and the target-to-crystal distance of 2045 mm.

The spectra from the J-KAREN experiments are compared to Stainless Steel (69% Fe, 19% Cr, 9% Ni) X-pinch experiments performed on the Zebra Generator at the Nevada Terawatt Facility at the University of Nevada, Reno described in section 2.1. The Zebra generator was operated with ~ 1 MA current and ~ 100 ns rise time. The X-pinches were composed of 4 wires crossed in an X pattern with a 31.7° angle between the wires on the anode and cathode sides. The wires were 40 μ m thick providing a 415 μ g/cm linear mass through a 20 mm anode to cathode gap. X-ray spectra were recorded using a time integrated spatially resolved spectrometer using a

LiF crystal ($2d=4.028 \text{ \AA}$). The spectrometer was capable of recording over a spectral range of $1.5 - 2.3 \text{ \AA}$ and used an 8 \mu m Kapton Polyimide, 0.3 \mu m Al, and 2 \mu m Polypropylene filter.

6.3 Modeling the K-shell Fe Spectra

The K-shell Fe experimental spectrum from plasmas irradiated by ultra-intense laser beams with femtosecond scale pulse duration is expected to be primarily dominated by three distinct regions. The first is the hottest region. This region is characterized by the prepulse (10^{10} contrast) interacting with the solid material, providing energy to excite the material before the main pulse arrives shortly after. The main pulse would then hit the already excited material, now plasma, which would further excite to the hottest region of the experiment. This would be most strongly composed of H-like, He-like, and Li-like Fe. It would be expected to have an electron temperature (T_e) between $3000 - 4000 \text{ eV}$ with optimal absorption of the main pulse when the electron density (N_e) is around $2 \times 10^{21} \text{ cm}^{-3}$, which for our case corresponded laser critical intensity.

The second region would be characterized by the portions of solid material that remain after the prepulse that are hit by the main pulse. This would create cooler plasma than the first region due to the higher density of the material. For neutral Fe, the solid density is $8.25 \times 10^{22} \text{ atoms/cm}^{-3}$. This region would be expected to be dominated by ionizations between Li-like and Ne-like Fe with an average ion charge of $+22-24$ which would suggest N_e for this region should be around $2 \times 10^{24} \text{ cm}^{-3}$.

The third region would be the material that does not directly interact with either the prepulse or main pulse. This region would be heated by the radiation transfer and hot electrons from the previous two regions. This would create relatively cold temperature plasma ($20-50 \text{ eV}$) that is likely to be dominated by ionizations near neutral Fe. This plasma would be close to solid

density with an average ion charge around +1-3. This suggests N_e should be around $8 \times 10^{22} - 2 \times 10^{23} \text{ cm}^{-3}$.

Theoretical spectra were obtained using two models: one for ionic transitions and one for characteristic transitions. These models are described in section 2.4.1. Figure 6.1 shows the spectrum recorded from the J-KAREN experiment with modeling. Three models are included that correspond with the expected predicted regions. Figure 6.1a covers the first expected region. The plasma parameters used to model this region were $T_e = 3500 \text{ eV}$, $N_e = 3 \times 10^{21} \text{ cm}^{-3}$, and 0.1% hot electrons. T_e was determined by matching the relative ratios of the He α and Ly α (1.78 Å) lines. N_e was determined by matching the relative ratios of the He α line with the intercombination (I.C.) line (1.86 Å). The hot electron concentration was most noticeable in the intensities of the H-like, He-like, and Li-like transitions. Increasing the hot electron concentration further emphasized the He-like transitions while the reducing the H-like and Li-like transitions.

The modeling in Figure 6.1b covers the second expected region. The modeling suggest plasma parameters of $T_e = 700 \text{ eV}$, $N_e = 1.8 \times 10^{24} \text{ cm}^{-3}$, and 0.1% hot electrons. This modeling primarily covers Li-like to C-like transitions. Changes to T_e shift the ionization balance of the plasma. The T_e for this region was determined by adjusting the ionization balance such that Be-like transitions ($\sim 1.87 \text{ Å}$) are the most prominent. Increasing N_e broadens the ionization distribution while decreasing N_e narrows the distribution. N_e was determined by matching the relative intensities of the Be-like, B-like and C-like structures. The presence of hot electrons effected the higher ionizations most significantly. Therefore the hot electron concentration was chosen by looking at the He-like, Li-like, and Be-like contributions to the spectrum.

Figure 6.1c compares the experimental spectrum with a model with plasma parameters of: $T_e = 10 \text{ eV}$, $N_e = 8 \times 10^{22} \text{ cm}^{-3}$, and 0.1% hot electrons with 10 keV temperature with 50 eV half width at half max (HWHM). These plasma parameters describe the K α and K β transitions near

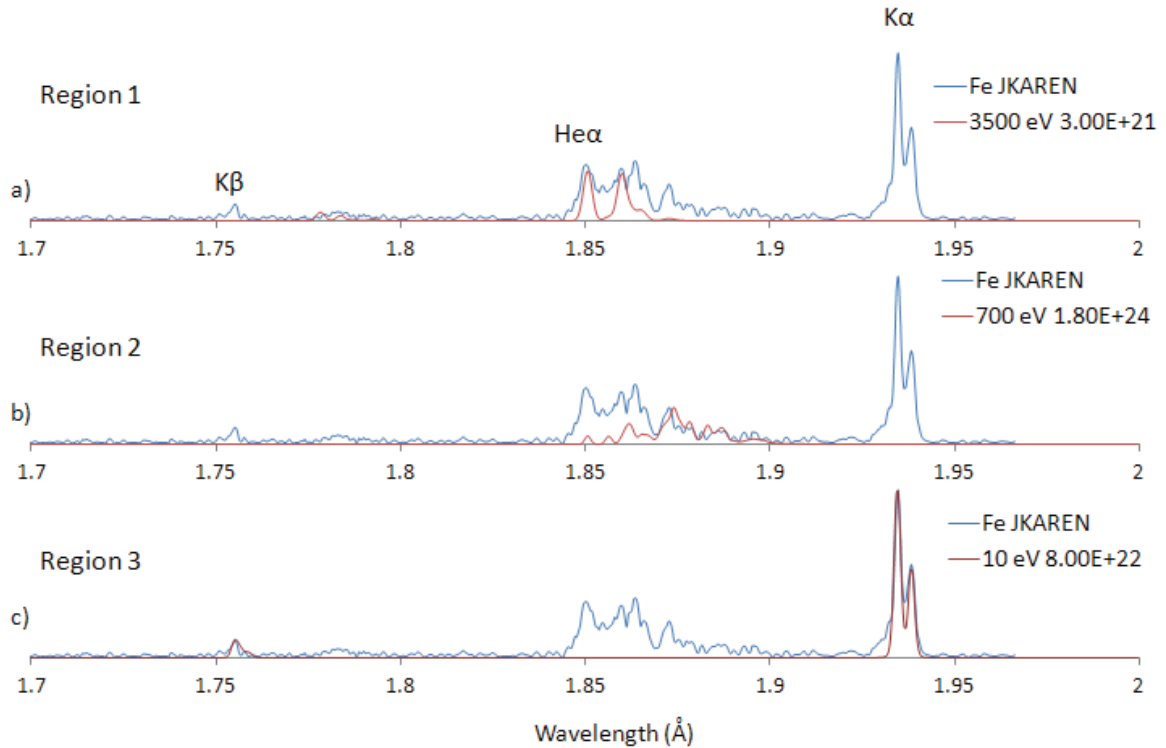


Figure 6.1. Theoretical modeling matched to experimental data from laser experiments performed at J-KAREN facility. All models include 0.1% hot electrons described with a Gaussian distribution at 10 keV with a 50 eV half width at half max (HWHM). a) 3500 eV and $8 \times 10^{22} \text{ cm}^{-3}$ modeling matches He α and Ly α transitions. b) 700 eV and $1.8 \times 10^{24} \text{ cm}^{-3}$ modeling matches B-like and C-like structures between 1.88 and 1.9 Å. c) Modeling for cold K α and K β transitions suggest 10 eV electron temperatures with a $8 \times 10^{22} \text{ cm}^{-3}$ electron density.

1.93 and 1.75 Å, respectively. The T_e was determined by aligning the location of the K β lines in the experimental and theoretical spectra. The K β transitions shift toward lower wavelengths with increasing T_e quicker than the K α transitions. The N_e is determined by matching the relative intensities of the two peaks in the K α region. The K α peaks are also influenced by the concentration of hot electrons. The presence of hot electrons increases the relative intensity of the higher wavelength peak. While the presence of hot electrons was a significant change to the modeling, varying the concentration of the hot electrons created very small changes to the modeling. This prevented a precise determination of the hot electron concentration in this region. A 0.1% concentration was used for the modeling as it was found to be a good match for the other regions in which the hot electron concentration is more noticeable.

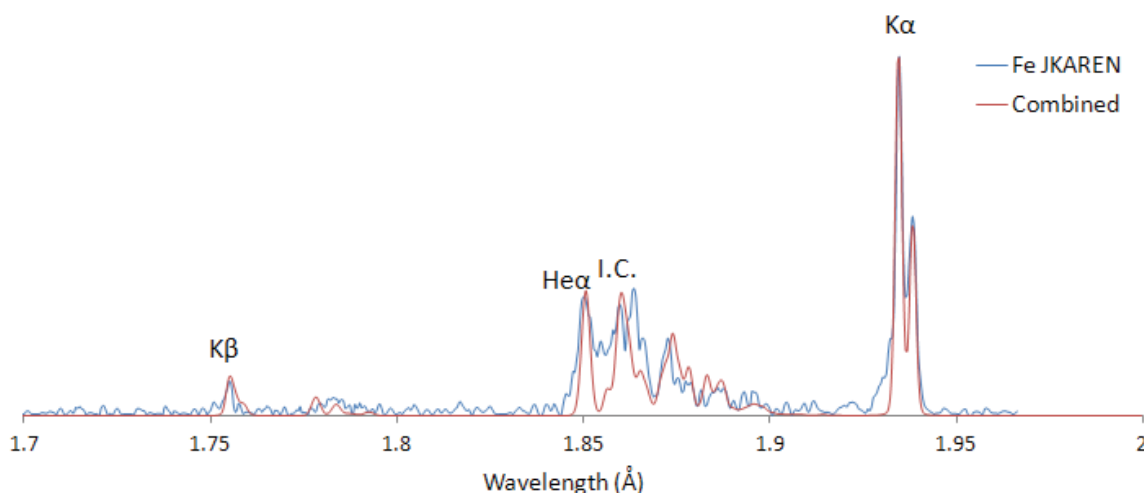


Figure 6.2. Combination of theoretical models shown in Figure 6.1 matched to the experimental spectrum. The modeling matches most structure between 1.85 and 1.95 Å.

Figure 6.2 compares the combined theoretical spectra from Figure 6.1 with the experimental spectra. The combined spectrum shows good comparison with the cold $K\alpha$ and $K\beta$ regions and with the Be-like, B-like, and C-like transitions. The most noticeable differences are surrounding the I.C. line. This is possibly due to some differences in wavelengths between the theoretical calculations and the experimental spectrum. The theoretical line for the Li-like peak just to the right of the I.C. line is closer to the I.C. line leading to more of a build up instead of a split peak. Also the theoretical line for the peak between the $He\alpha$ and I.C. line is shifted close to the I.C. line. This leads to the peak getting absorbed into the I.C. line when trying to broaden the He-like transitions rather than rising to fill the region.

Figure 6.3 is a comparison of the experimental spectrum with three models that include a very high concentration of hot electrons in a mild T_e (300 eV) bulk plasma with the intent to describe the hotter plasma using one plasma region. The three concentrations are a) 10%, b) 25%, and c) 40% which were chosen to display the effects of hot electrons on the theoretical spectrum. Figure 6.3a displays the 10% hot electron concentration and it covers the lower ionization states without any significant presence of the He- and Li-like ions. Figure 6.3b is the 25% hot electron

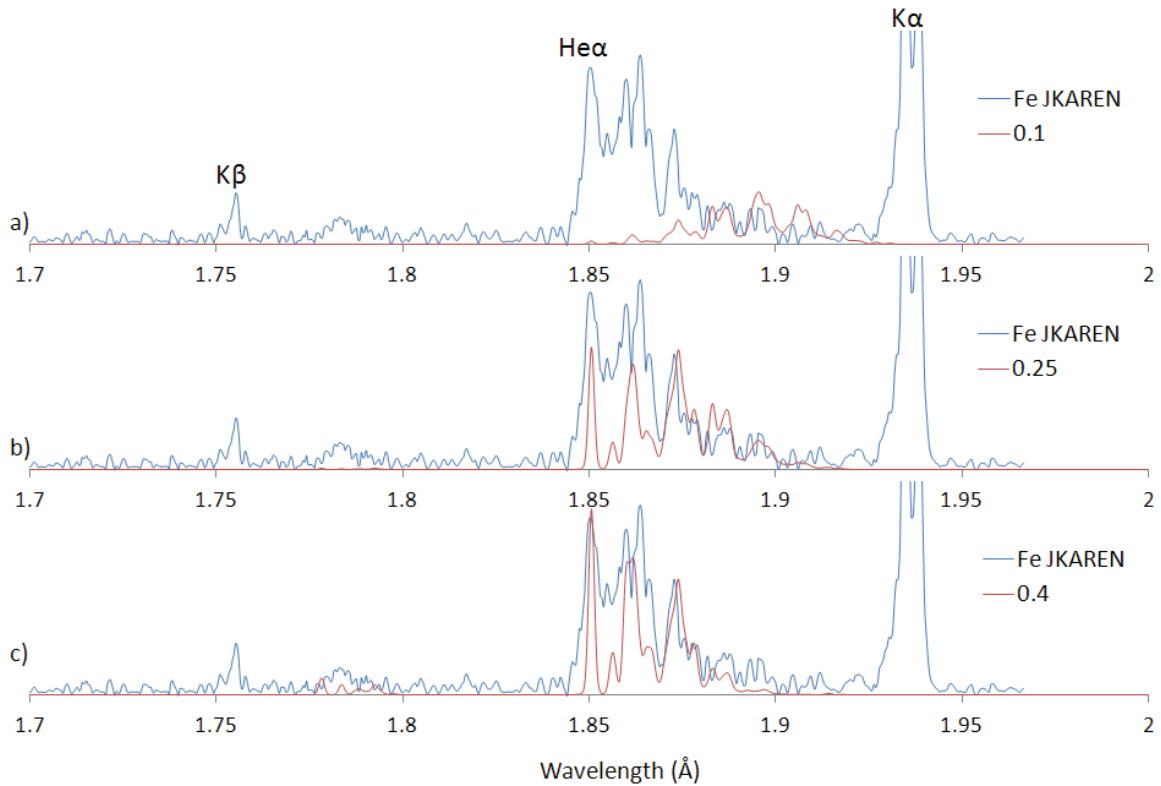


Figure 6.3. Theoretical modeling of three different hot electron concentrations, a) 10%, b) 25%, and c) 40%, with a bulk $T_e=300$ eV and $N_e=1.8 \times 10^{24}$ cm $^{-3}$. The modeling shows the ionization balance does not fit the experimental spectrum which confirms the need for multiple regions shown in Figure 6.1.

concentration and it has a balance between the higher (He- and Li-like) and the lower (B- and C-like) ionization levels. This balance does not fit with the experimental spectrum as the higher ionizations are underrepresented and the lower ionizations are slightly overestimated. Figure 6.3c is the 40% concentration and it matches the higher ionizations closer while the lower ionizations are underestimated. This figure confirms that the hotter plasma cannot be a single region of mild T_e with a high hot electron concentration.

Figure 6.4 displays a K-shell Fe experimental spectrum recorded during a stainless steel X-pinch experiment performed on the Zebra generator at 1 MA. Three theoretical spectra are compared with the experimental spectrum to point out the differences of the X-pinch spectrum and the Laser-produced spectrum. The theoretical spectra were modeled at $T_e=170$ eV and

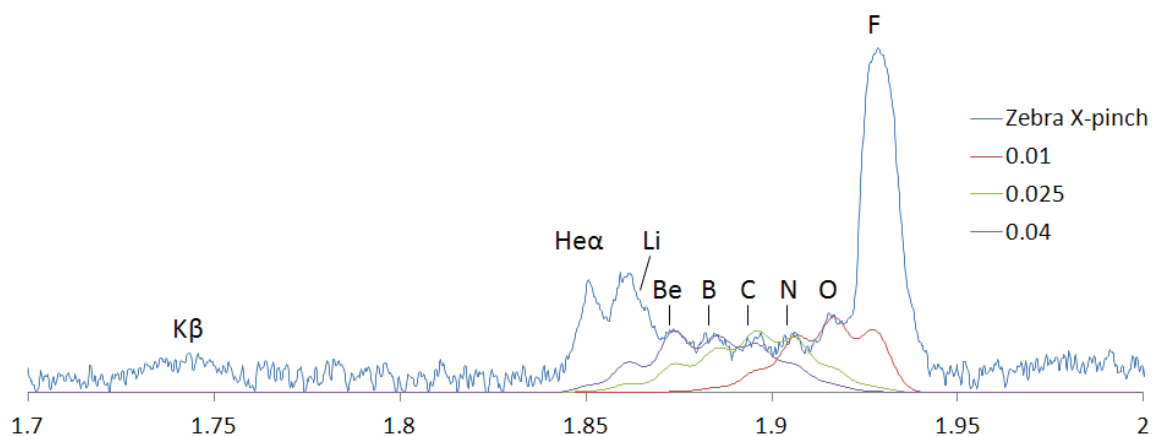


Figure 6.4. Theoretical modeling showing the influence of different ionizations on the K-shell Fe experimental spectrum from a stainless steel X-pinch experiment performed on the Zebra generator at 1 MA. Modeling was done with $T_e=170$ eV and $N_e=1 \times 10^{20}$ cm^{-3} and three different hot electron concentrations (1%, 2.5%, and 4%). The experimental spectrum shows evidence of He-like to F-like ions.

$N_e=1 \times 10^{20}$ cm^{-3} with varying hot electron concentrations (1%, 2.5%, and 4%). The Laser-produced spectrum was dominated by fewer regions that were relatively easy to distinguish, while the X-pinch spectrum is composed of significant contributions from all the ionizations between He-like and Ne-like Fe which occurs as the plasma ionizes throughout the experiment.

Figure 6.5 is the experimental spectrum for the X-pinch compared to two theoretical

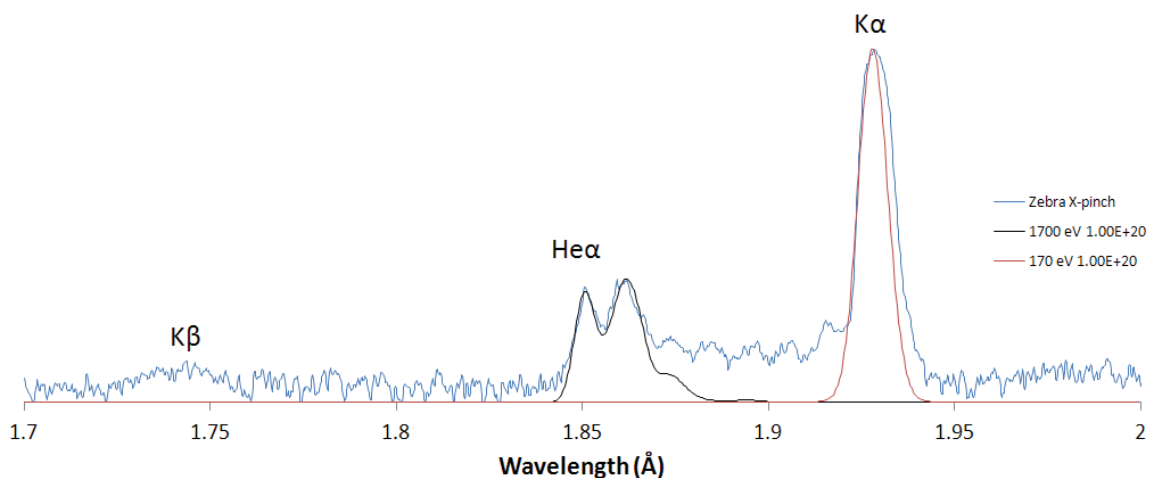


Figure 6.5. Theoretical modeling for Stainless Steel X-pinch spectra estimating the plasma parameters of the highest T_e (1700 eV, 1×10^{20} cm^{-3}) and lowest T_e (170 eV, 1×10^{20} cm^{-3}) regions.

spectra that describe the maximum and minimum temperature regions represented in the experimental spectrum. The cold region is estimated with $T_e = 170$ eV and $N_e = 1 \times 10^{20}$ cm⁻³. This is primarily Ne-like transitions that fill in the largest peak in the spectrum. T_e is estimated by matching the location of the $K\alpha$ peak with the theoretical spectrum. N_e is chosen by using the value from the hot region as the density can't be properly estimated using one line. The hottest region is estimated with $T_e = 1700$ eV and $N_e = 1 \times 10^{20}$ cm⁻³. N_e is estimated by matching the relative intensities of the $He\alpha$ line with the I.C. line. T_e is estimated with less accuracy as there is not a $Ly\alpha$ line presence with which to compare the $He\alpha$ line.

6.4 Conclusions

The laser-produced spectrum was describable with the three predicted plasma regions: 1) the preplasma region irradiated by both the prepulse and the main pulse, 2) the solid density plasma from the center of the focusing spot region irradiated by only the main pulse, and 3) the solid density periphery region excited by the radiation and hot electrons emitted from the previous two regions. This creation of separate regions can occur due to the fast and ultra-intense interaction of the laser with the target. The fs pulse duration occurs so fast and its intensity is so high, that due to optical field ionization (Ammosov *et al* 1986), the atoms are ionized faster than they can radiate which prevents radiation from intermittent ions. The spectrum from the stainless steel X-pinch experiment was different because the intermediate ions were present. This is due to the much longer time scale of the experiment where the current typically rises for 30-60 ns prior to the first explosion of the X-pinch. The X-pinch spectrum had a strong $K\alpha$ presence suggesting colder plasma surrounding the hotter core. This is similar to the $K\alpha$ presence in the laser experiment; however, the T_e for each experiment is significantly different (~ 10 eV laser and ~ 170 eV X-pinch). The colder laser-produced plasma is heated by X-ray radiation and fast electrons from the hotter regions while the colder plasma in the X-pinch experiment is also energized by

the kinetic energy acquired while being accelerated by the explosions and implosions. This is seen in the different ionization levels of the transitions that dominate the $K\alpha$ peaks. The hottest regions for each experiment are also quite different. The value of the electron densities differ by an order of magnitude ($3 \times 10^{21} \text{ cm}^{-3}$ laser, $1 \times 10^{20} \text{ cm}^{-3}$ X-pinch) and the maximum values of the electron temperatures are quite different (3500 eV laser, 1700 eV X-pinch). The T_e difference is quickly noticeable by the presence of the $\text{Ly}\alpha$ in the laser-produced spectrum and not in the X-pinch spectrum.

Along with estimating the conditions of the laser-produced plasma, there was the hope to observe effects of X-ray pumping and hot electrons by analyzing KK and KL hollow ion emissions. The spectral regions where the KK and KL hollow ion transitions would be seen are within approximately 1.8-1.85 Å and 1.86-1.92 Å, respectively. Unfortunately, the KK hollow ions spectral region provided no evidence of spectral lines. The KL hollow ion spectral region included multiple peaks of greater intensity that are also influenced by singly excited state transitions. The modeling of the laser-produced spectrum was improved with the inclusion of a small percentage of hot electrons for each of the three regions. The hot electrons were generated in the two hotter regions and dispersed to the coldest region to excite the near neutral atoms which then produced the $K\alpha$ emissions. The hot electrons also broadened the ionization distribution for the two hotter regions. Though the X-ray source intensity $\sim 10^{17} \text{ W/cm}^2$ was enough to create KK hollow ions in aluminum (Faenov *et al* 2015), it was insufficient to create KK hollow ions of iron. The KL spectral region does have a reasonable presence though it is difficult to distinguish between the KL transitions and the singly excited state transitions. By considering the KK and KL emission regions it was determined that there were no sufficient effects from X-ray pumping on the spectra of hollow ions of iron in laser-produced plasma experimental conditions. At the same time it was shown that influence of hot electrons for formation of K-shell spectra of iron is rather large.

Chapter 7

Conclusion

This dissertation focuses on using spectroscopic analysis to expand the knowledge related to the processes involved in plasma formation and evolution. Z-pinch, X-pinch, and laser experiments were performed to produce X-ray radiation from plasmas that can be recorded with an advanced set of diagnostics. The Z-pinch and X-pinch experiments were performed using the Zebra Generator and the laser experiments were performed using the Leopard Laser and the J-KAREN Laser. The experimental facilities were described in Chapter 2 along with the theoretical models used to estimate plasma conditions for both K-shell and L-shell radiating plasmas. The non-LTE kinetic models used include K-shell Al, Mg, and Fe, and L-shell Cu and Ni.

Chapter 3 discussed the results from the CWA precursor plasma research. It began by investigating CWAs with mid-atomic number materials (Cu and Ni) to further research whether the high electron temperatures (>300 eV) found for the first time previously for Ni-60 (94% Cu and 6% Ni) CWA precursor plasmas (Coverdale *et al* 2009) are consistent for other wire materials with similar atomic numbers. Experiments at 1 MA using Alume1 (95% Ni, 2% Al, 2% Mn, and 1% Si) and pure Cu were analyzed with results confirming that high electron temperatures can be found with other mid-atomic-number materials. This research continued with experiments using Ni-60 CWAs to study the effects of increasing the current from 1 MA to 1.7 MA. The results included determining that the electron density and plasma column size increased with the increase in current, while the electron temperature remained fairly consistent. These results were published in *IEEE Transactions on Plasma Science* (Stafford *et al* 2015). The CWA precursor plasma research continued with mixed material CWAs using both Alume1 and Al wires. The results from the time gated spectra detailed the early evolution of K-shell Al and L-shell Ni

radiation. The plasma conditions estimated from the K-shell Al spectra suggested lower electron temperatures than from the uniform Al CWA while the L-shell Ni remained very similar to the uniform Alumel CWA. The results from the mixed material CWAs were presented at the Division of Plasma Physics Conference in 2012.

Chapter 4 detailed the first X-pinch experiments at 1.7 MA on the Zebra Generator. In general, X-pinches create the hottest and densest plasmas out of the different pinch configurations. Ti alloy X-pinches were used to begin the enhanced current experiments with X-pinches because Ti was found to produce the hottest K-shell radiation for the standard current of 1 MA on the Zebra Generator. The goal of these experiments was to optimize the experimental parameters, most notably the array mass, to best take advantage of the increased current and determine what the limits are for the Zebra Generator with the enhanced current. The optimization of the array mass was improved, however, not perfectly realized. As for testing the limits of the enhanced current, the small Al concentration (6%) in the Ti alloy radiated much stronger than predicted. Optically thick K-shell Al spectra were recorded with the time integrated spectrometer with estimated electron temperatures of ~ 550 eV. The intense K-shell Al radiation completely dominated the spectra region where third order K-shell Ti was expected. However, fourth order K-shell Ti was recorded with both hot ionic lines ($\text{He}\alpha$, I.C.) and cold characteristic $\text{K}\alpha$ lines. Fifth order Fe $\text{K}\alpha$ was also recorded but this was from the excitation of the anode of the machine and not from the wires. The time gated spectrometer recorded the early stages of the X-pinch radiation. It began with characteristic $\text{K}\alpha$ radiation from both Ti and Fe which faded away and was replaced by intense background radiation and K-shell Al lines. Pure Ti X-pinch experiments were performed to gain a better understanding of the unexpected results from the Ti alloy experiments. The pure Ti experiments supported the lack of third order K-shell Ti and provided a clearer look at the fourth order reflections of K-shell Ti that improved the confidence in the identification of the lines recorded in the Ti alloy experiments. These results were

presented at the International Conference on Plasma Science in 2014 and as an invited talk at the Radiation from High Energy Density Physics Conference in 2015.

In Chapter 5, the results from Leopard Laser experiments were explained. Flat Mg targets were irradiated by the Leopard laser to produce Mg plasma that emitted K-shell radiation with pronounced satellite line structures near the Ly α and He β lines. The laser was operated in three different conditions: 350 fs pulse duration and 10^{-7} prepulse to main pulse contrast, 350 fs duration and 10^{-5} contrast, and 0.8 ns duration and 10^{-5} contrast. The goal of these experiments was to identify the transitions responsible for the satellite structures and to determine the importance of dielectronic recombination in producing the satellite structures. The satellite structures near the He β line were able to be identified as Li-like $1s3/3l'-1s^23l$ and $1s3/4l'-1s^24l$ transitions and Be-like $1s3/3l'3l''-1s^23/3l'$ transitions. These satellites were mostly matched with the theoretical spectra with a couple areas that need further investigation. The Ly α satellite structures were not as fully described with the He-like $2nl'-1snl''$ transitions with $n = 2,3,4,5$. This suggests dielectronic recombination is not as significant for these satellite lines as it is for the He β satellite lines. The results from this research were published in the *Journal of Physics B* (Stafford *et al* 2014).

Chapter 6 explored the significance of hot electrons and X-ray pumping in K-shell Fe spectra recorded from the J-KAREN Laser. The plasma produced by the irradiation from the laser was found to emit from three distinct plasma regions: 1) the preplasma region irradiated by both the prepulse and the main pulse, 2) the solid density plasma from center of focusing spot region irradiated by only the main pulse, and 3) the solid density periphery region excited by the radiation and hot electrons emitted from the previous two regions. This occurred due to the quick interaction with the short duration (35 fs) and ultra-intense laser pulse. For contrast, K-shell Fe spectra from an X-pinch experiment was compared showing a more diverse spread of Ka

radiation from all the ionizations between He-like and F-like which comes with the much slower experimental timeframe of 30 - 60 ns to first X-ray burst. It was found that hot electrons played a significant role in the K-shell radiation from the laser produced spectra as each region was best modeled using a 0.1% hot electron concentration. On the other hand, the hollow ion transitions that would manifest effects from X-ray pumping were not significantly noticeable. These results have been submitted for review to *High Energy Density Physics*.

The last six years of research has been a complete experience. I participated in 15 experimental campaigns using either the Zebra Generator or the Leopard Laser. I was in charge of signal processing for both types of experimental campaigns from the spring of 2013 to the spring of 2016. I presented my research at 15 conferences with 11 posters and 4 oral talks, two of which were invited. Two first authored peer reviewed articles were published with a third currently under review. Additional twelve papers and four conference proceedings included me as a coauthor. I was a mentor for three undergraduate students and contributed to multiple proposals for grants. Overall I became proficient with using theoretical codes, spectroscopic analysis, diode signals, and plasma imaging tools, to evaluate processes in high energy density plasma. I learned how to manage data collection from experiments and how to work in a team to achieve our research goals. I was a part of the local organizing committee for the Radiation from High Energy Density Plasmas Conference in 2015. Finally, I gained experience leading others by overseeing the process of preparing for my experiments and mentoring undergraduate students with their own research projects.

References

- E.V. Aglizki, V.A. Boiko, A.Ya. Faenov, V.V. Korneev, V.V.Krutov, S.L. Mandelstam, S.A. Pikuz, U.I. Safronova, J.A. Sylwester, A.M. Urnov, L.A. Vainshtein, and I.A. Zhitnik, *New Satellite Structure of the Solar and Laser Plasma Spectra in Vicinity of the La (Mg XII) Line*, *Solar Physics* **56**, 375 (1978)
- M.V. Ammosov, N.B. Delone, and V.P. Krainov, *Tunnel ionization of complex atoms and of atomic ions in an alternating electromagnetic field*, *Journal of Experimental and Theoretical Physics* **64**, 1191 (1986)
- J.P. Apruzese, P.E. Pulsifer, J. Davis, R.W. Clark, K.G. Whitney, J.W. Thornhill, T.W.L. Sanford, G.A. Chandler, C. Deeney, D.L. Fehl, T.J. Nash, R.B. Spielman, W.A. Stygar, K.W. Struve, R.C. Mock, T.L. Gilliland, D.O. Jobe, J.S. McGurn, J.F. Seamen, J.A. Torres, and M. Vargas., *K-shell radiation physics in the ultrahigh optical depth pinches of the Z generator*, *Physics of Plasmas* **5**, 4476 (1998)
- B.S. Bauer, V.L. Kantsyrev, F. Winterberg, A.S. Shlyaptseva, R.C. Mancini, H. Li, A. Oxner, *The dense Z-pinch program at the University of Nevada, Reno*, *AIP Conference Proceedings* **409**, 153-156 (1997)
- F.N. Beg, A. Ciardi, I. Ross, Y. Zhu, A.E. Dangor, and K. Krushelnick, *Jet Formation and Current Transfer in X-Pinches*, *IEEE Transactions on Plasma Science*, **34**, 2325 (2006)
- P. Beiersdorfer, T. Phillips, V.L. Jacobs, K.W. Hill, M. Bitter, S. von Goeler, and S.M. Kahn, *High-Resolution Measurements, Line Identification, and Spectral Modeling of $K\alpha$ Transitions in Fe XVIII-Fe XXV*, *The Astrophysical Journal* **409**, 846 (1993)
- P. Beiersdorfer, S. von Goeler, M. Bitter, and D.B. Thorn, *Measurement of the 3d-2p resonance to intercombination line-intensity ratio in neonlike Fe XVII, Ge XXIII, and Se XXV*, *Physical Review A* **64**, 032705 (2001)
- P. Beiersdorfer, *Laboratory X-ray Astrophysics*, *Annual Review of Astronomy and Astrophysics* **41**, 343 (2003)

F. Blasco, C. Stenz, F. Salin, A.Ya. Faenov, A.I. Magunov, T.A. Pikuz, and I.Yu. Skobelev, *Portable, tunable, high-luminosity spherical crystal spectrometer with an x-ray charge coupled device, for high-resolution x-ray spectromicroscopy of clusters heated by femtosecond laser pulses*, Review of Scientific Instruments **72**, 1956 (2001)

V.A. Boiko, A.Ya. Faenov, S.A. Pikuz, and U.I. Safronova, *The analysis of satellites to the H-like ion resonance lines observed in the X-ray region*, Monthly Notices of the Royal Astronomical Society **181**, 107 (1977)

V.A. Boiko, A.Ya. Faenov, and S.A. Pikuz, *X-ray spectroscopy of multiply-charged ions from laser plasmas*, Journal of Quantitative Spectroscopy and Radiative Transfer **19**, 11 (1978)

S.C. Bott, S.V. Lebedev, D.J. Ampleford, S.N. Bland, J.P. Chittenden, A. Ciardi, M.G. Haines, C. Jennings, M. Sherlock, G. Hall, J. Rapley, F.N. Beg, and J. Palmer, *Dynamics of cylindrically converging precursor plasma flow in wire-array Z-pinch experiments*, Physical Review E **74**, 046403 (2006)

M.H. Chen, *Dielectronic Satellite Spectra for He-like Ions*, Atomic Data and Nuclear Data Tables **34**, 301 (1986)

J.P. Chittenden, S.V. Lebedev, A.R. Bell, R. Aliaga-Rossel, S.N. Bland, and M.G. Haines, *Plasma Formation and Implosion Structure in Wire Array Z Pinches*, Physical Review Letters **83**, 100 (1999)

A.S. Chuvatin, V.L. Kantsyrev, L.I. Rudakov, M.E. Cuneo, A.L. Astanovitskiy, R. Presura, A.S. Safronova, W. Cline, K.M. Williamson, I. Shrestha, G.C. Osborne, B. LeGalloudec, V. Nalajala, T.D. Pointon, and K.A. Mikkelsen, *Operation of a load current multiplier on a nanosecond mega-ampere pulse forming line generator*, Physical Review Special Topics - Accelerators and Beams **13**, 010401 (2010)

J. Colgan, J. Abdallah Jr, A. Faenov, T.A. Pikuz, and I.Yu. Skobelev, *MUTA calculations of a laser-produced Mg hollow atom spectrum*, Physica Scripta **78**, 015302 (2008)

J. Colgan, J. Abdallah, Jr., A.Ya. Faenov, S.A. Pikuz, E. Wagenaars, N. Booth, O. Culfa, R.J. Dance, R.G. Evans, R.J. Gray, T. Kaempfer, K.L. Lancaster, P. McKenna, A.L. Rossall, I.Yu. Skobelev, K.S. Schulze, I. Uschmann, A.G. Zhidkov, and N.C. Woolsey, *Exotic Dense-Matter*

States Pumped by a Relativistic Laser Plasma in the Radiation-Dominated Regime, Physical Review Letters **110**, 125001 (2013)

C.A. Coverdale, C. Deeney, M.R. Douglas, J.P. Apruzese, K.G. Whitney, J.W. Thornhill, and J. Davis, *Optimal Wire-Number Range for High X-Ray Power in Long-Implosion-Time Aluminum Z Pinches*, Physical Review Letters **88**, 065001 (2002)

C.A. Coverdale, A.S. Safronova, V.L. Kantsyrev, N.D. Quart, A.A. Esaulov, C. Deeney, K.M. Williamson, G.C. Osborne, I. Shrestha, D.J. Ampleford, and B. Jones, *Observation of >400 -eV Precursor Plasmas from Low-Wire-Number Copper Arrays at the 1-MA Zebra Facility*, Physical Review Letters **102**, 155006 (2009)

C.A. Coverdale, B. Jones, D.J. Ampleford, J. Chittenden, C. Jennings, J.W. Thornhill, J.P. Apruzese, R.W. Clark, K.G. Whitney, A. Dasgupta, J. Davis, J. Guiliani, P.D. LePell, C. Deeney, D.B. Sinars, and M.E. Cuneo, *K-shell X-ray sources at the Z Accelerator*, High Energy Density Physics **6**, 143 (2010)

M.E. Cuneo, D.B. Sinars, E.M. Waisman, D.E. Bliss, W.A. Stygar, R.A. Vesey, R.W. Lemke, I.C. Smith, P.K. Rambo, J.L. Porter, G.A. Chandler, T.J. Nash, M.G. Mazarakis, R.G. Adams, E.P. Yu, K.W. Struve, T.A. Mehlhorn, S.V. Lebedev, J.P. Chittenden, and C.A. Jennings, *Compact single and nested tungsten-wire-array dynamics at 14–19 MA and applications to inertial confinement fusion*, Physics of Plasmas **13**, 056318 (2006)

V. Decaux, P. Beiersdorfer, A. Osterheld, M. Chen, and S.M. Kahn, *High-Resolution Measurements of the Ka Spectra of Low-Ionization Species of Iron: a New Spectral Signature of Nonequilibrium Ionization Conditions in Young Supernova Remnants*, The Astrophysical Journal **443**, 464 (1995)

V. Decaux, P. Beiersdorfer, S.M. Kahn, and V.L. Jacobs, *High Resolution Measurement of the Ka Spectrum of Fe XXV–XXVIII: New Spectral Diagnostics of Nonequilibrium Astrophysical Plasmas*, The Astrophysical Journal **482**, 1076 (1997)

C. Deeney, P.D. LePell, B.H. Failor, S.L. Wong, J.P. Apruzese, K.G. Whitney, J.W. Thornhill, J. Davis, E. Yadlowsky, R.C. Hazelton, J.J. Moschella, T. Nash, and N. Loter, *Increased kilo-electron-volt x-ray yields from Z-pinch plasmas by mixing elements of similar atomic numbers*, Physical Review E **51**, 4823 (1995)

B.L. Deng, G. Jiang, L. Zhang, X. Wang, and X.Z. Hua, *Relativistic configuration interaction calculations on $K\alpha$ X-ray satellites of magnesium ions*, European Physical Journal D **66**, 146 (2012)

J.J. Drake, D.A. Swartz, P. Beiersdorfer, G.V. Brown, and S.M. Kahn, *On Photospheric Fluorescence and the Nature of the 17.62 Å Feature in Solar X-ray Spectra*, The Astrophysical Journal **521**, 839 (1999)

J. Dubau and S. Volonte, *Dielectronic recombination and its applications in astronomy*, Reports on Progress in Physics **43**, 199 (1980)

B. Edlen and F. Tyren, *Atomic Energy States of an Unusual Type*, Nature **143**, 940 (1939)

R.N.C. Eze, *Fe $K\alpha$ line in hard X-ray emitting symbiotic stars*, Monthly Notices of the Royal Astronomical Society **437**, 857 (2014)

A.Ya. Faenov, S.A. Pikuz, A.I. Erko, B.A. Bryunetkin, V. M. Dyakin, G.V. Ivanenkov, A.R. Mingaleev, T.A. Pikuz, V.M. Romanova, and T.A. Shelkovenko, *High-Performance X-ray Spectroscopic Devices for Plasma Microsources Investigations*, Physics Scripta **50**, 333 (1994)

A.Ya. Faenov, A.I. Magunov, T.A. Pikuz, I.Yu. Skobelev, S.A. Pikuz, A.M. Urnov, J. Abdallah, R.E.H. Clark, J. Cohen, R.P. Jonson, G.A. Kyrala, M.D. Wilke, A. Maksimchuk, D. Umstadter, N. Nantel, R. Doron, E. Behar, P. Mandelbaum, J.J. Schwob, J. Dubau, F.B. Rosmej, and A. Osterheld, *High-resolved X-ray spectra of hollow atoms in a femtosecond laser-produced solid plasma*, Physica Scripta **T80**, 536 (1999)

A.Ya. Faenov, J. Colgan, S.B. Hansen, A. Zhidkov, T.A. Pikuz, M. Nishiuchi, S.A. Pikuz, I.Yu. Skobelev, J. Abdallah, H. Sakaki, A. Sagisaka, A.S. Pirozhkov, K. Ogura, Y. Fukuda, M. Kanasaki, N. Hasegawa, M. Nishikino, M. Kando, Y. Watanabe, T. Kawachi, S. Masuda, T. Hosokai, R. Kodama, and K. Kondo, *Nonlinear increase of X-ray intensities from thin foils irradiated with a 200 TW femtosecond laser*, Scientific Reports **5**, 13436 (2015)

A.H. Gabriel and C. Jordan, *Long Wavelength Satellites to the He-like Ion Resonance Lines in the Laboratory and in the Sun*, Nature **221**, 947 (1969)

A.H. Gabriel, *Dielectronic Satellite Spectra for Highly-charged Helium-like Ion lines*, Monthly Notices of the Royal Astronomical Society **160**, 99 (1972)

- M.F. Gu, *The Flexible Atomic Code*, American Institute of Physics Conference Proceedings **730**, 127 (2004)
- M.F. Gu, *The flexible atomic code*, Canadian Journal of Physics **86**, 675-689 (2008)
- S.B. Hansen, *Development and Application of L-shell Spectroscopic Modeling for Plasma Diagnostics*, Ph.D. Dissertation, University of Nevada, (2003)
- S.B. Hansen, J. Colgan, A.Ya. Faenov, J. Abdallah Jr., S.A. Pikuz Jr., I.Yu. Skobelev, E. Wagenaars, N. Booth, O. Culfa, R.J. Dance, G.J. Tallents, R.G. Evans, R.J. Gray, T. Kaempfer, K.L. Lancaster, P. McKenna, A.K. Rossall, K.S. Schulze, I. Uschmann, A.G. Zhidkov, and N.C. Woolsey, *Detailed analysis of hollow ions spectra from dense matter pumped by X-ray emission of relativistic laser plasma*, Physics of Plasmas **21**, 031213 (2014)
- R. Jain, A.K. Pradhan, V. Joshi, K.J. Shah, J.J. Travedi, S.L. Kayasth, V.M. Shah, and M.R. Deshpande, *The Fe-line Feature in the X-ray Spectrum of Solar Flares: First Results from the SOXS Mission*, Solar Physics **239**, 217 (2006)
- V.L. Kantsyrev, L.I. Rudakov, A.S. Safronova, D.A. Fedin, V.V. Ivanov, A.L. Velikovich, A.A. Esaulov, A.S. Chuvatin, K. Williamson, N.D. Quart, V. Nalajala, G. Osborne, I. Shrestha, M.F. Yilmaz, S. Pokala, P.J. Laca, and T.E. Cowan, *Planar Wire Array as Powerful Radiation Source*, IEEE Transactions on Plasma Science **34**, 2295 (2006)
- T. Kato, N. Yamamoto, R. More, and T. Fujimoto, *Collisional radiative model including dielectronic states*, Journal of Quantitative Spectroscopy & Radiative Transfer **71**, 431 (2001)
- H. Kiriya, M. Mori, Y. Nakai, T. Shimomura, H. Sasao, M. Tanoue, S. Kanazawa, D. Wakai, F. Sasao, H. Okada, I. Daito, M. Suzuki, S. Kondo, K. Kondo, A. Sugiyama, P.R. Bolton, A. Yokoyama, H. Daido, S. Kawanishi, T. Kimura, and T. Tajima, *High temporal and spatial quality petawatt-class Ti:sapphire chirped-pulse amplification laser system*, Optics Letters **35**, 1497 (2010)
- S.V. Lebedev, I.H. Mitchell, R. Aliaga-Rossel, S.N. Bland, J.P. Chittenden, A.E. Dangor, and M.G. Haines, *Azimuthal Structure and Global Instability in the Implosion Phase of Wire Array Z-Pinch Experiments*, Physical Review Letters **81**, 4152 (1998)

S.V. Lebedev, F.N. Beg, S.N. Bland, J.P. Chittenden, A.E. Dangor, M.G. Haines, S.A. Pikuz and T.A. Shelkovenko, *Plasma formation and the implosion phase of wire array z-pinch experiments*, Laser and Particle Beams **19**, 355-376 (2001)

M.K. Matzen, M.A. Sweeney, R.G. Adams, J.R. Asay, J.E. Bailey, G.R. Bennett, D.E. Bliss, D.D. Bloomquist, T.A. Brunner, R.B. Campbell, G.A. Chandler, C.A. Coverdale, M.E. Cuneo, J.P. Davis, C. Deeney, M.P. Desjarlais, G.L. Donovan, C.J. Garasi, T.A. Hail, C.A. Hall, D.L. Hanson, M.J. Hurst, B. Jones, M.D. Knudson, R.J. Leeper, R.W. Lemke, M.G. Mazarakis, D.H. McDaniel, T.A. Mehlhorn, T.J. Nash, C.L. Olson, J.L. Porter, P.K. Rambo, S.E. Rosenthal, G.A. Rochau, L.E. Ruggles, C.L. Ruiz, T.W.L. Sanford, J.F. Seamen, D.B. Sinars, S.A. Slutz, I.C. Smith, K.W. Struve, W.A. Stygar, R.A. Vesey, E.A. Weinbrecht, D.F. Wenger, and E.P. Yu, *Pulsed-power-driven high energy density physics and inertial confinement fusion research*, Physics of Plasmas **12**, 55503 (2005)

M. Nishiuchi, H. Sakaki, T.Zh. Esirkepov, K. Nishio, T.A. Pikuz, A.Ya. Faenov, I.Yu. Skobelev, R. Orlandi, H. Sako, A.S. Pirozhkov, K. Matsukawa, A. Sagisaka, K. Ogura, M. Kanasaki, H. Kiriya, Y. Fukuda, H. Koura, M. Kando, T. Yamauchi, Y. Watanabe, S.V. Bulanov, K. Kondo, K. Imai, and S. Nagamiya, *Acceleration of highly charged GeV Fe ions from a low-Z substrate by intense femtosecond laser*, Physics of Plasmas **22**, 033107 (2015)

G. Osborne, *An Investigation of Tungsten-Based Z-Pinch Planar Wire Array and Benchmarking Experiments*, Ph.D. Dissertation, University of Nevada, (2012)

N.D. Quart, *Radiative properties of Z-pinch and laser produced plasmas from mid-atomic-number materials*, Ph.D. Dissertation, University of Nevada, (2010)

N.J. Peacock, M.G. Hobby, and M. Galanti, *Satellite spectra for helium-like ions in laser-produced plasmas*, Journal of Physics B: Atomic, Molecular, and Optical Physics **6**, L298 (1973)

O. Peyrusse, P. Combis, M. Lousi-Jacquet, D. Naccache, C.J. Keane, B.J. MacGowan, and D.L. Matthews, *Spectroscopic diagnostics of an x-ray laser plasma by use of L-shell spectra*, Journal of Applied Physics **65**, 3802 (1989)

K.J.H. Phillips, *The solar photospheric-to-coronal Fe abundance ratio from X-ray fluorescence lines*, Monthly Notices of the Royal Astronomical Society **421**, 1757 (2012)

S.A. Pikuz, T.A. Shelkovenko, V.M. Romanova, D.A. Hammer, A.Ya. Faenov, V.A. Dyakin, and T.A. Pikuz, *High-luminosity monochromatic x-ray backlighting using an incoherent plasma source to study extremely dense plasmas*, Review of Scientific Instruments **68**, (1997)

S.A. Pikuz, A.Ya. Faenov, J. Colgan, R.J. Dance, J. Abdallah, E. Wagenaars, N. Booth, O. Culfa, R.G. Evans, R.J. Gray, T. Kaempfer, K.L. Lancaster, P. McKenna, A.L. Rossall, I.Yu. Skobelev, K.S. Schulze, I. Uschmann, A.G. Zhidkov, and N.C. Woolsey, *Measurement and simulations of hollow atom X-ray spectra of solid-density relativistic plasma created by high-contrast PW optical laser pulses*, High Energy Density **9**, 560 (2013)

G. Ponti, S. Bianchi, T. Munoz-Darias, B. De Marco, T. Dwelly, R.P. Fender, K. Nandra, N. Rea, K. Mori, D. Haggard, C.O. Heinke, N. Degenaar, T. Aramaki, M. Clavel, A. Goldwurm, C.J. Hailey, G.L. Israel, M.R. Morris, A. Rushton, and R. Terrier, *On the Fe K absorption – accretion state connection in the Galactic Centre neutron star X-ray binary AX J1745.6-2901*, Monthly Notices of the Royal Astronomical Society **446**, 1536 (2015)

F.B. Rosmej, A.Ya. Faenov, T.A. Pikuz, F. Flora, P.Di. Lazzaro, T. Letardi, A. Grilli, A. Reale, L. Palladino, G. Tomassetti, A. Scafati, and L. Reale, *Line formation of high-intensity He β -Rydberg dielectronic satellites 1s3lnl' in dense laser-produced plasmas*, Journal of Physics B: Atomic, Molecular, and Optical Physics **31**, L921 (1998)

F.B. Rosmej, U.N. Funk, M. Geibel, D.H.H. Hoffmann, A. Tauschwitz, A.Ya. Faenov, T.A. Pikuz, I.Yu. Skobelev, F. Flora, S. Bollanti, P.Di. Lazzaro, T. Letardi, A. Grilli, L. Palladino, A. Reale, G. Tomassetti, A. Scafati, L. Reale, T. Auguste, P. D'Oliveira, S. Hulin, P. Monot, A. Maksimchuk, S.A. Pikuz, D. Umstadter, M. Nantel, R. Bock, M. Dornik, M. Stetter, S. Stowe, V. Yakushev, M. Kulisch, and N. Shilkin, *X-ray radiation from ions with K-shell vacancies*, Journal of Quantitative Spectroscopy & Radiative Transfer **65**, 477 (2000)

F.B. Rosmej, A. Calisti, B. Talin, R. Stamm, W. Sub, M. Geibel, D.H.H. Hoffmann, A.Ya. Faenov, and T.A. Pikuz, *Observation of two-electron transitions in dense non-Maxwellian laser-produced plasmas and their use as diagnostic reference lines*, Journal of Quantitative Spectroscopy & Radiative Transfer **71**, 639 (2001)

A.S. Safronova, V.L. Kantsyrev, N. Ouart, F. Yilmaz, D. Fedin, A. Astanovitsky, B. LeGalloudec, S. Batie, D. Brown, V. Nalajala, S. Pokala, I. Shrestha, T.E. Cowan, B. Jones, C.A. Coverdale, C. Deeney, S.B. Hansen, P.D. LePell, D. Jobe, and D. Nielson, *Spectroscopic*

modeling of radiation from Cu and Mo X-pinch produced on the UNR 1MA Zebra generator, Journal of Quantitative Spectroscopy & Radiative Transfer **99**, 560 (2006)

A.S. Safronova, V.L. Kantsyrev, M.F. Yilmaz, G. Osborne, N.D. Ouart, K. Williamson, I. Shrestha, V. Shlyaptseva, S. Batie, B. LeGalloudec, A. Astanovitsky, V. Nalajala, and W. McDaniel, *Radiative properties of implosions of combined X-pinch and planar wire arrays composed from different wire materials on the UNR 1 MA Z-pinch generator*, High Energy Density Physics **3**, 237 (2007)

A.S. Safronova, V.L. Kantsyrev, P. Neill, U.I. Safronova, D.A. Fedin, N.D. Ouart, M.F. Yilmaz, G. Osborne, I. Shrestha, K. Williamson, T. Hoppe, C. Harris, P. Beiersdorfer, and S. Hansen, *The importance of EBIT data for Z-pinch plasma diagnostics*, Canadian Journal of Physics **87**, 267 (2008)

A.S. Safronova, V.L. Kantsyrev, A.A. Esaulov, N.D. Ouart, U.I. Safronova, I. Shrestha, and K.M. Williamson, *X-ray spectroscopy and imaging of stainless steel X-pinch with application to astrophysics*, The European Physical Journal Special Topics **169**, 155 (2009a)

A.S. Safronova, V.L. Kantsyrev, U.I. Safronova, A.A. Esaulov, M.F. Yilmaz, N.D. Ouart, I. Shrestha, K.W. Williamson, G.C. Osborne, P.G. Wilcox, M.E. Weller, V. Shlyaptseva, C.A. Coverdale, B. Jones, D.J. Ampleford, P.D. LePell, and C. Deeney, *Studying Radiation from Z-pinch Wire Array and X-Pinch Plasmas: K-shell Mg to M-shell Mo*, American Institute of Physics Conference Proceedings **1161**, 217 (2009b)

A.S. Safronova, V.L. Kantsyrev, A.A. Esaulov, I. Shrestha, V.V. Shlyaptseva, M.E. Weller, N.D. Ouart, G.C. Osborne, A. Stafford, S.F. Keim, A.L. Velikovich, J.L. Giuliani, and A.S. Chuvatin, *Producing kiloelectronvolt L-shell plasmas on Zebra at UNR*, IEEE Transactions on Plasma Science **40**, 3347 (2012a)

A.S. Safronova, V.L. Kantsyrev, A.Y. Faenov, U.I. Safronova, P. Wiewior, N. Renard-Le Galloudec, A.A. Esaulov, M.E. Weller, A. Stafford, P. Wilcox, I. Shrestha, N.D. Ouart, V. Shlyaptseva, G.C. Osborne, O. Chalyy, and Y. Paudel, *Atomic physics of relativistic high contrast laser-produced plasmas in experiments on Leopard laser facility at UNR*, High Energy Density Physics **8**, 190 (2012b)

U.I. Safronova, M.S. Safronova, R. Bruch, and L.A. Vainshtein, *Dielectronic Satellite Spectra of the $1s3p-1s^2$ Lines for Highly-Charged Ions with $Z = 6-54$ ($1s2l3l'-1s^22l$ Transitions)*, *Physica Scripta* **51**, 471 (1995)

U.I. Safronova and M.S. Safronova, *Relativistic many-body calculations of energies for doubly-excited $1s2l2l'$ and $1s3l3l'$ states in Li-like ions*, *Canadian Journal of Physics* **82**, 743 (2004)

T.A. Shelkovenko, D.B. Sinars, S.A. Pikuz, K.M. Chandler, and D.A. Hammer, *Point-projection x-ray radiography using an X pinch as the radiation source*, *Review of Scientific Instruments* **72**, 667 (2001)

T.A. Shelkovenko, S.A. Pikuz, D.B. Sinars, K.M. Chandler, and D.A. Hammer, *Time-resolved spectroscopic measurements of ~ 1 keV, dense, subnanosecond X-pinch plasma bright spots*, *Physics of Plasmas* **9**, 2165 (2002)

I.Yu. Skobelev, A.Ya. Faenov, B.A. Bryunetkin, V. M. Dyakin, T.A. Pikuz, S.A. Pikuz, T.A. Shelkovenko, V.M. Romanova, and A.R. Mingaleev, *Investigating the emission properties of plasma structures with x-ray imaging spectroscopy*, *Journal of Experimental and Theoretical Physics* **81**, 692 (1995)

I.Yu. Skobelev, A.Ya. Faenova, T.A. Pikuz, A.I. Magunov, F. Flora, S. Bollanti, P. DiLazzaro, D. Murra, A. Reale, L. Reale, G. Tomassetti, A. Ritucci, G. Petrocelli, S. Martellucci, N. Lisi, and F.B. Rosmej, *Spectral Transitions from the Rydberg Autoionization States of a Li-Like Mg X Ion*, *Journal of Experimental and Theoretical Physics* **95**, 421 (2002)

L. Spitzer Jr., *Physics of Fully Ionized Gases*, John Wiley and Sons (1962)

A. Stafford, A.S. Safronova, U.I. Safronova, V.L. Kantsyrev, A.Y. Faenov, P. Wiewior, M.E. Weller, I. Shrestha, V.V. Shlyaptseva, and Y. Paudel, *Analysis of Mg spectral features produced by irradiations of laser pulses with different contrast and pulse durations*, *Journal of Physics B: Atomic, Molecular, and Optical Physics* **47**, 065001 (2014)

A. Stafford, A.S. Safronova, V.L. Kantsyrev, M.E. Weller, I. Shrestha, V.V. Shlyaptseva, C.A. Coverdale, and A.S. Chuvatin, *Mid-Atomic-Number Cylindrical Wire Array Precursor Plasma Studies on Zebra*, *IEEE Transactions on Plasma Science* **43**, 2497 (2015)

- L. Steenman-Clark, F. Bely-Dubau, and P. Faucher, *Calculations of the atomic parameters for the dielectronic satellite lines of the Mg XI resonance line*, Monthly Notices of the Royal Astronomical Society **191**, 951 (1980)
- J.W. Thornhill, A.L. Velikovich, R.W. Clark, J.P. Apruzese, J. Davis, K.G. Whitney, P.L. Coleman, C.A. Coverdale, C. Deeney, B.M. Jones, and P.D. Lepell, *Assessing the ZR Machine's Potential for Producing Multi-keV X-Ray Yields in K-Shell Line and Free-Bound Continuum Radiation*, IEEE Transactions on Plasma Science **34**, 2377 (2006)
- L.A. Vainshtein and U.I. Safronova, *Wavelengths and Transition Probabilities of Satellites to Resonance Lines of H- and He-like Ions*, Atomic Data and Nuclear Data Tables **21**, 49 (1978)
- L.A. Vainshtein and U.I. Safronova, *Dielectronic Satellite Spectra for Highly Charged H-like Ions ($2l'3l''-1s2l$, $2l3l''-1s3l$) and He-like Ions ($1s2l'3l''-1s^22l$, $1s2l'3l''-1s^23l$) with $Z=6-33$* , Atomic Data and Nuclear Data Tables **25**, 311 (1980)
- M.E. Weller, *Theoretical and Experimental Studies of Radiation from Z-Pinch Complex Wire Arrays and Applications*, Ph.D. Dissertation, University of Nevada, (2014)
- K.G. Whitney, J.W. Thornhill, J.P. Apruzese, and J. Davis, *Basic Considerations for Scaling Z-pinch X-ray Emission with Atomic Number*, Journal of Applied Physics **67**, 1725 (1990)
- P.P. Wiewior, V.V. Ivanov, and O. Chalyy, *Development of the 50 TW laser for joint experiments with 1 MA Z-pinches*, Journal of Physics: Conference Series **244**, 032013 (2010)
- K.M. Williamson, *Implosion and Radiation Dynamics of Cylindrical and Planar Wire Array Z-pinch Plasma*, Ph.D. Dissertation, University of Nevada, (2011)
- E.J. Yadlowsky, J.J. Moschella, R.C. Hazelton, T.B. Settersten, G.G. Spanjers, C. Deeney, B.H. Failor, P.D. LePell, J. Davis, J.P. Apruzese, K.G. Whitney, and J.W. Thornhill, *Evidence for precursor plasma formation resulting from heterogeneous current channels in wire array loads*, Physics of Plasmas **3**, 1745 (1996)
- N. Yamamoto, T. Kato, and F.B. Rosmej, *Opacity free and space resolved X-ray diagnostics based on satellite lines near H-like $Ly\alpha$ of highly charged ions*, Journal of Quantitative Spectroscopy & Radiative Transfer **96**, 343 (2005)

M.F. Yilmaz, *Radiative properties of L-shell Mo and K-shell Al plasmas from planar and cylindrical wire arrays imploded at 1 MA Z-pinch generator*, Ph.D. Dissertation, University of Nevada, (2009)

B.K.F. Young, A.L. Osterheld, R.S. Walling, W.H. Golstein, T.W. Phillips, R.E. Stewart, G. Charatis, and Gar. E. Busch, *Measurement of density-sensitive electric quadrupole transition in neonlike laser-produced plasmas*, *Physical Review Letters* **62**, 1266 (1989)